

**Studies of the  $K^+ \rightarrow \pi^+ \pi^0$  background  
for the measurement of  $K^+ \rightarrow \pi^+ \nu \bar{\nu}$   
and  $\pi^0 \rightarrow \nu \bar{\nu}$  decays**

by

Jie Fu

B.Sc., Shandong University, 2010

A THESIS SUBMITTED IN PARTIAL FULFILLMENT OF  
THE REQUIREMENTS FOR THE DEGREE OF

MASTER OF SCIENCE

in

The Faculty of Graduate and Postdoctoral Studies

(Physics)

THE UNIVERSITY OF BRITISH COLUMBIA

(Vancouver)

August 2016

© Jie Fu 2016

# Abstract

The NA62 experiment aims at measuring the branching ratio of the ultra-rare decay  $K^+ \rightarrow \pi^+ \nu \bar{\nu}$  with 10% precision. To achieve the desired precision, high levels of background rejection must be accomplished using techniques such as high-resolution timing, kinematic rejection, particle identification, and hermetic vetoing of photons.  $K^+ \rightarrow \pi^+ \pi^0$  ( $K_{\pi 2}$ ) decays, one of the largest background sources, are mainly rejected by kinematics reconstruction and photon vetoing in NA62. To evaluate  $K_{\pi 2}$  background rejection capabilities of the NA62 system, we studied the inefficiency of these two techniques.  $K_{\pi 2}$  and  $K^+ \rightarrow \mu^+ \nu$  ( $K_{\mu 2}$ ) events were selected from 2015 minimum bias data runs using  $K_{\pi 2}/K_{\mu 2}$  separation cuts whose efficiency was also studied in details. The inefficiency of kinematics suppression was found to be  $(2.16 \pm 0.21) \times 10^{-3}$ , and the upper limit of the photon veto inefficiency was  $7 \times 10^{-7}$  at 90% confidence level. Combined with correction factors from Monte Carlo simulations, a preliminary result,  $S/B > 0.2$ , was estimated for  $K_{\pi 2}$  background in the measurement of  $K^+ \rightarrow \pi^+ \nu \bar{\nu}$ . Also, an upper limit on the branching ratio of the invisible decay  $\pi^0 \rightarrow \nu \bar{\nu}$ ,  $4.3 \times 10^{-7}$ , was obtained at 90% confidence level.

# Preface

This thesis is based on the experimental apparatus and data of the NA62 experiment.

The NA62 collaboration has 337 members from 30 different institutions. I joined the experiment in January 2015 when the 2014 pilot run finished. Since then I mainly focused on the data analysis and tried to evaluate  $K_{\pi 2}$  background rejection capabilities of the NA62 system. I also worked with the STRAW working group during my stay at CERN. Under the supervision of Hans Danielson, I conducted several tests using the STRAW prototype: gas leak measurements, experimenting with methods of decreasing the ambient noise signal, examining the signal threshold using the scanning data and also gain measurement presented in Appendix A. In addition, I participated in a few data taking shifts in 2015 and 2016.

The apparatus description in Chapter 3 is mainly based on the NA62 technical design [1] and papers on related detectors. The corrections (section 4.1), one track selection cuts (section 4.2) and additional LKr reconstruction algorithm (section 5.1.2) are developed by Giuseppe Ruggiero. With the help of Douglas Bryman and Giuseppe Ruggiero, I set photon veto cuts in Chapter 5. I completed all the data analysis of 2015 minimum bias data and Monte Carlo data presented in this thesis except reconstruction of data runs which was conducted by Antonino Sergi.

# Table of Contents

<b>Abstract</b>	ii
<b>Preface</b>	iii
<b>Table of Contents</b>	iv
<b>List of Tables</b>	vii
<b>List of Figures</b>	viii
<b>Glossary</b>	xi
<b>Acknowledgements</b>	xiii
<b>Dedication</b>	xiv
<b>1 Introduction</b>	1
1.1 Overview of the NA62 experiment	1
1.1.1 Motivation for the NA62 experiment	1
1.1.2 Decay-in-flight technique	2
1.1.3 Main background sources and rejection techniques	4
1.2 $K_{\pi 2}$ background study	8
1.3 $\pi^0 \rightarrow \nu\bar{\nu}$ study	8
1.4 Outline of the thesis	10
<b>2 NA62 Experimental Apparatus</b>	11
2.1 Beam line	13
2.2 Tracking devices	14
2.2.1 GTK	15
2.2.2 STRAW spectrometer	16
2.3 Particle identification and timing	18
2.3.1 CEDAR	18
2.3.2 RICH	19

*Table of Contents*

---

2.3.3	CHOD . . . . .	22
2.4	Veto system . . . . .	23
2.4.1	CHANTI . . . . .	23
2.4.2	Photon veto . . . . .	25
2.4.3	Muon veto . . . . .	29
<b>3</b>	<b>Analysis strategies . . . . .</b>	<b>33</b>
3.1	$K_{\pi 2}$ background evaluation . . . . .	33
3.1.1	Kinematics suppression . . . . .	33
3.1.2	$\pi^0$ suppression . . . . .	34
3.2	Upper limit on the branching ratio of the decay $\pi^0 \rightarrow \nu\bar{\nu}$ . . . . .	34
<b>4</b>	<b>Data sample selection . . . . .</b>	<b>36</b>
4.1	Corrections . . . . .	36
4.1.1	Spectrometer momentum correction . . . . .	36
4.1.2	LKr correction . . . . .	37
4.2	One track event selection cuts . . . . .	38
4.3	$K_{\pi 2}$ and $K_{\mu 2}$ separation cuts and efficiency evaluation . . . . .	48
4.3.1	Overview of separation cuts . . . . .	48
4.3.2	Efficiency . . . . .	51
4.4	Final cuts used for selecting the data sample . . . . .	57
4.4.1	Cuts for kinematics suppression study . . . . .	57
4.4.2	Cuts for the $\pi^0$ suppression study and $\pi^0 \rightarrow \nu\bar{\nu}$ study . . . . .	58
<b>5</b>	<b>Photon veto cuts . . . . .</b>	<b>60</b>
5.1	LKr photon . . . . .	60
5.1.1	LKr standard photon . . . . .	60
5.1.2	LKr extra photon . . . . .	61
5.2	LAV photons . . . . .	62
5.3	SAC and IRC photons . . . . .	62
5.3.1	SAV-LAVFEE photons . . . . .	63
5.3.2	SAV-CREAM photons . . . . .	63
5.4	False veto effect . . . . .	64
<b>6</b>	<b>Analysis results . . . . .</b>	<b>67</b>
6.1	Kinematics . . . . .	67
6.1.1	Kinematics rejection for $K_{\pi 2}$ . . . . .	67
6.1.2	Kinematics acceptance for $K_{\pi\nu\bar{\nu}}$ . . . . .	68
6.2	$\pi^0$ rejection using photon veto cuts . . . . .	70
6.3	$K_{\pi 2}$ background . . . . .	71

*Table of Contents*

---

6.4	Branching ratio of the decay $\pi^0 \rightarrow \nu\bar{\nu}$ . . . . .	71
<b>7</b>	<b>Conclusions</b> . . . . .	<b>73</b>
	<b>Bibliography</b> . . . . .	<b>75</b>
 <b>Appendices</b>		
<b>A</b>	<b>Gain measurement of the STRAW spectrometer</b> . . . . .	<b>80</b>
<b>B</b>	<b>Study of the false <math>K_{\pi 2}</math> rejection caused by additional <math>\pi^+</math> LKr clusters</b> . . . . .	<b>84</b>

# List of Tables

1.1	Most frequent $K^+$ decays . . . . .	4
1.2	Photon destinations in NA62 . . . . .	9
2.1	Comparison between the measured properties of full intensity beam in 2015 run with the design values . . . . .	14
4.1	Geometrical acceptance cuts for detectors. . . . .	42
4.2	Efficiency of LKr and MUV3 cuts for selecting $K_{\pi 2}$ and $K_{\mu 2}$ events . . . . .	59
5.1	Number of $K_{\mu 2}$ events passing photon cuts . . . . .	66
6.1	Number of $K_{\pi 2}$ events in two momentum ranges passing the photon veto cuts. . . . .	71

# List of Figures

1.1	A bird's-eye view of the SPS and NA62 site . . . . .	1
1.2	The box and penguin diagrams contributing to the $K^+ \rightarrow \pi^+ \nu \bar{\nu}$ decay . . . . .	2
1.3	The seven candidate events of the BNL E787 and E949 experiments. . . . .	3
1.4	Kinematics of the decay $K^+ \rightarrow \pi^+ \nu \bar{\nu}$ . . . . .	5
1.5	$M_{missing}^2$ distribution for the signal and the kinematically constrained $K^+$ decays. . . . .	6
1.6	$M_{missing}^2$ distribution for the signal and generic $K^+$ decays. . . . .	7
1.7	Diagrams contributing to the $\pi^0 \rightarrow \nu \bar{\nu}$ decay . . . . .	9
2.1	Layout of the NA62 experimental setup . . . . .	12
2.2	Scheme of the primary and secondary beams . . . . .	13
2.3	Schematic layout of the GTK . . . . .	15
2.4	Schematic view of the magnetic spectrometer . . . . .	17
2.5	Schematic drawing of the four views of each straw chamber . . . . .	18
2.6	Schematic layout of the CEDAR . . . . .	19
2.7	Schematic layout of the RICH . . . . .	20
2.8	Fitted RICH ring radius for different downstream particles in 2015 run . . . . .	21
2.9	Sketch of two planes of the CHOD . . . . .	22
2.10	Schematic layout of the new CHOD . . . . .	24
2.11	Beam induced background rejected by the CHANTI . . . . .	25
2.12	A layout of a complete CHANTI station . . . . .	26
2.13	Picture of the first LAV station . . . . .	27
2.14	Details of the ribbons and electrodes . . . . .	28
2.15	Shashlyk technology . . . . .	29
2.16	Layout of a scintillator plate in MUV1 and MUV2 . . . . .	31
2.17	A view of the MUV1 and MUV2 . . . . .	32
4.1	Number of straw chambers hit by downstream track . . . . .	39
4.2	Straw momentum difference before and after fit . . . . .	40

*List of Figures*

---

4.3	Diagrams for matching the CHOD Candidate with the Spectrometer track . . . . .	41
4.4	Criteria for matching the LKr Cluster with the Spectrometer track . . . . .	43
4.5	Criteria for matching the CEDAR Candidate with the Spectrometer track . . . . .	43
4.6	Criteria for matching the CHANTI Candidate with the Spectrometer track . . . . .	44
4.7	Diagrams for matching a multi-ring RICH Candidate with the Spectrometer track . . . . .	46
4.8	Diagrams for matching a single-ring RICH Candidate with the Spectrometer track . . . . .	47
4.9	CDA and Z position distribution of decay vertex reconstructed with nominal kaon . . . . .	48
4.10	CDA and Z position distribution of decay vertex reconstructed with GTK kaon . . . . .	49
4.11	RICH mass distributions for one track events . . . . .	50
4.12	$\frac{E}{P}$ distribution for one track events . . . . .	51
4.13	$M_{missing-\pi}^2$ distribution for one track events . . . . .	52
4.14	$M_{missing-\mu}^2$ distribution for one track events . . . . .	53
4.15	$M_{missing-\pi}^2$ and $M_{missing-\mu}^2$ distributions for both $K_{\pi 2}$ and $K_{\mu 2}$ decays . . . . .	55
4.16	Efficiency of $M_{missing-\pi}^2$ cut for selecting $K_{\pi 2}$ sample . . . . .	55
4.17	RICH mass distributions for $K_{\pi 2}$ and $K_{\mu 2}$ decays . . . . .	56
4.18	Efficiency of RICH mass cuts for selecting $K_{\pi 2}$ and $K_{\mu 2}$ events. . . . .	57
4.19	$\frac{E}{P}$ distributions for $K_{\pi 2}$ and $K_{\mu 2}$ decays . . . . .	58
5.1	Time difference between the LKr photon candidates and the associated CHOD track . . . . .	62
5.2	Time difference between the LKr extra photon candidate and the associated CHOD track . . . . .	63
5.3	Time difference between LAV photon candidate and the associated CHOD track . . . . .	64
5.4	Time difference between LAVFEE based SAV photon candidate and the associated CHOD track . . . . .	65
5.5	Time difference between CREAM based SAV photon candidate and the associated CHOD track . . . . .	65
6.1	$M_{missing-\pi}^2$ distribution for $K_{\pi 2}$ MC events . . . . .	68

*List of Figures*

---

6.2	$M_{missing-\pi}^2$ distribution for $K_{\pi 2}$ events using GTK kaon and spectrometer . . . . .	69
6.3	$M_{missing-\pi}^2$ distribution for $K_{\pi\nu\bar{\nu}}$ MC events . . . . .	69
6.4	$K_{\pi 2}$ events surviving each photon veto cut . . . . .	70
A.1	Straw prototype with Gas and HV Input Connected . . . . .	81
A.2	Gain v.s. Voltage for $Ar - CO_2(70-30)$ at 970 mbar . . . . .	81
A.3	Gain v.s. Voltage for $Ar - CO_2(85-15)$ at 970 mbar . . . . .	83
A.4	Gain v.s. Voltage for $Ar - CO_2(93-7)$ at 970 mbar . . . . .	83
B.1	Distance of the selected LKr cluster to the projected position of $\pi^+$ in the LKr . . . . .	85
B.2	The reject efficiency distribution for different radii of the masked region . . . . .	85

# Glossary

<b>BNL</b>	Brookhaven National Laboratory
<b>BR</b>	branching ratio, fraction of particles which decay by an individual decay mode with respect to the total number of particles which decay
<b>CEDAR</b>	CErenkov Differential counter with Achromatic Ring focus
<b>CERN</b>	European Organization for Nuclear Research, the world's largest particle physics laboratory located in Geneva on the Franco-Swiss border
<b>CHANTI</b>	CHarged ANTIcounter
<b>CHOD</b>	Charged particle HODoscopes
<b>C.L.</b>	confidence level
<b>GTK</b>	GigaTracker
<b>IRC</b>	Inner Ring Calorimeter
<b>LAV</b>	Large Angle Veto
<b>LHC</b>	Large Hadron Collider, the world's largest and highest-energy particle accelerator at present.
<b>LKr</b>	Liquid Krypton Calorimeter
<b>MIPs</b>	Minimum Ionizing Particles
<b>MUV</b>	Muon Veto
<b>NAHIF</b>	North Area High Intensity Facility
<b>RICH</b>	Ring Imaging CHerenkov detector
<b>SAC</b>	Small Angle Calorimeter

## *Glossary*

---

<b>SM</b>	Standard Model of Particle physics
<b>SPS</b>	Superconducting Proton Synchrotron (see <a href="http://home.cern/about/accelerators/super-proton-synchrotron">http://home.cern/about/accelerators/super-proton-synchrotron</a> )
<b>S/B</b>	Signal-to-background Ratio

# Acknowledgements

Firstly, I would like to express my sincere gratitude to my supervisor, Doug Bryman, for the support and advice. He was always available when I ran into a problem and had questions on detectors and analysis. His guidance helped me in all the time of research and writing of this thesis.

I would also like to thank Tommaso Spadaro and Giuseppe Ruggiero for their help on data analysis. My particular thanks go to Giuseppe Ruggiero who provided the initial analysis code example and helpful comments. I am also grateful to Antonino Sergi for the reconstruction of physics data and answering questions on the NA62 experiment. Special thanks go to Hans Danielson for his supervision when I was working in STRAW group.

Furthermore, many thanks go to all the other NA62 members for the detector construction and the development of the simulation and reconstruction packages.

I would like to acknowledge Reiner Krucken as the second reader of this thesis.

Finally, I have to express out appreciation to my family and friends for always supporting me throughout my years of study.

*To my parents.*

# Chapter 1

## Introduction

### 1.1 Overview of the NA62 experiment

The NA62 experiment [2] is a fixed target kaon experiment driven by Superconducting Proton Synchrotron (SPS) at the European Organization for Nuclear Research (CERN). Its primary goal is to measure the branching ratio (BR) of the ultra-rare kaon decay  $K^+ \rightarrow \pi^+ \nu \bar{\nu}$  with 10% precision by collecting  $O(100)$   $K^+ \rightarrow \pi^+ \nu \bar{\nu}$  events with less than 10% background, for testing Standard Model (SM) predictions where new physics effects may induce a deviation.



Figure 1.1: A bird's-eye view of the SPS and NA62 site (<http://na62.web.cern.ch/NA62/>).

#### 1.1.1 Motivation for the NA62 experiment

Among many rare flavour changing neutral current  $K$  and  $B$  decays, the extremely rare kaon decay  $K^+ \rightarrow \pi^+ \nu \bar{\nu}$  is very sensitive to new physics

through the underlying mechanisms of flavour dynamics and can be used to explore the short-distance scales up to  $O(1,000 \text{ TeV})$  [3]. This decay is one of the best probes for new physics effects complementary to Large Hadron Collider (LHC) searches, especially within Non-Minimal Flavour Violation models [4, 5].

The  $K^+ \rightarrow \pi^+ \nu \bar{\nu}$  decay is the strongly suppressed second order weak decay in the SM. It arises at the quark level from  $s \rightarrow d \nu \bar{\nu}$  decay, which receives one-loop contributions from electroweak W-box and Z-penguin diagrams in the SM as shown in Figure 1.2 [6].

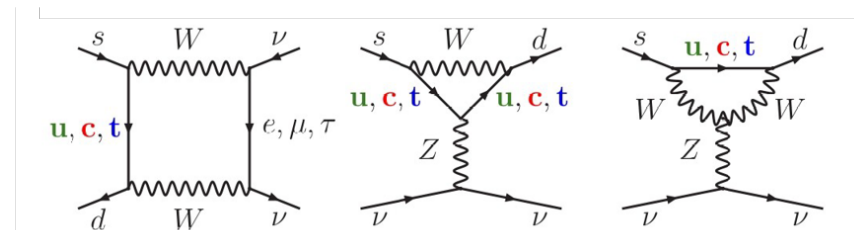


Figure 1.2: The box and penguin diagrams contributing to the  $K^+ \rightarrow \pi^+ \nu \bar{\nu}$  decay.

The predicted SM branching ratio of this decay has been calculated to high precision [7, 8, 9]:

$$Br(K^+ \rightarrow \pi^+ \nu \bar{\nu})_{SM} = (0.781 \pm 0.075 \pm 0.029) \times 10^{-10} \quad (1.1)$$

where the first error comes from quark-mixing parameter uncertainties and the second error is the theoretical input uncertainty, while the most precise experimental result so far is,

$$Br(K^+ \rightarrow \pi^+ \nu \bar{\nu})_{exp} = (1.73^{+1.15}_{-1.05}) \times 10^{-10} \quad (1.2)$$

obtained by the E787 and E949 experiments [10] at the Brookhaven National Laboratory (BNL) based on only 7 observed candidate events shown in Figure 1.3. Although this result agrees with the SM theoretical prediction, the experimental error is quite large. A measurement of the rate with at least 10% precision is needed for a significant test of new physics. This motivates the next generation rare kaon decay experiment, NA62.

### 1.1.2 Decay-in-flight technique

Unlike E797 and E949 which used a stopped- $K^+$  technique, the NA62 Collaboration tries a decay-in-flight technique at beam momentum of 75 GeV/c.

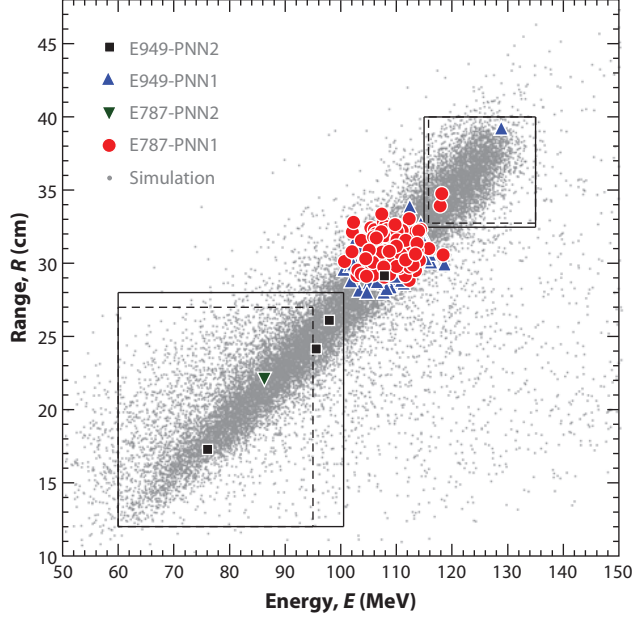


Figure 1.3: This figure shows seven  $K^+ \rightarrow \pi^+ \nu \bar{\nu}$  candidate events of the E787 and E949 experiments in the PNN1 and PNN2. Two signal regions were indicated as boxes. The points near  $E = 110 \text{ MeV}$  are background  $K^+ \rightarrow \pi^+ \pi_0$  events which survive photon veto cuts, and the small grey dots represent the simulated  $K^+ \rightarrow \pi^+ \nu \bar{\nu}$  events passing the trigger [10].

This new technique brings in some advantages. First, it allows us to get high momentum kaons and decay particles, which leads to a more efficient detection of decay particles, particularly photons arising from  $\pi^0$  ( $\pi^0 \rightarrow \gamma\gamma$ )<sup>1</sup> in the  $K^+ \rightarrow \pi^+ \pi^0$  ( $K_{\pi 2}$ ) decay. Besides, this approach does not require tagging of the  $\pi \rightarrow \mu \rightarrow e$  decay chain as needed in stopped- $K^+$  technique [10]. The decay-in-flight technique hence permits a higher rate, which makes it possible to detect more candidate events in a short time.

A detailed description of the NA62 experimental setup is presented in Chapter 2. The 400 GeV/c SPS proton beam at a rate of  $1.1 \times 10^{12}$  Hz produces a secondary charged beam by impinging on a beryllium target. After passing a rigorous selecting system, the secondary beam's momentum is confined to  $(75.0 \pm 1\%)$  GeV/c with a small angular deviation. Then the

<sup>1</sup> $Br(\pi^0 \rightarrow \gamma\gamma) \approx 98.82\%$ ,  $Br(\pi^0 \rightarrow e^+e^-\gamma) \approx 1.17\%$  [11].

### 1.1. Overview of the NA62 experiment

Decay Channel	BR (%)	Rejection Strategies
$K^+ \rightarrow \mu^+ \nu_\mu$	$63.55 \pm 0.11$	$\mu$ -ID, kinematics
$K^+ \rightarrow \pi^+ \pi^0$	$20.66 \pm 0.08$	Photon veto, kinematics
$K^+ \rightarrow \pi^+ \pi^+ \pi^-$	$5.59 \pm 0.04$	Charged Particle Veto, kinematics
$K^+ \rightarrow \pi^0 e^+ \nu_e$	$5.07 \pm 0.04$	Photon veto, $e$ -ID
$K^+ \rightarrow \pi^0 \mu^+ \nu_\mu$	$3.353 \pm 0.034$	Photon veto, $\mu$ -ID
$K^+ \rightarrow \pi^+ \pi^0 \pi^0$	$1.761 \pm 0.022$	Photon veto, kinematics

Table 1.1: List of the six most frequent  $K^+$  decays with corresponding rejection techniques.

high intensity hadron beam ( $\sim 750$  MHz) enters an 117 m long cylindrical vacuum tank with a diameter of 1.92 to 2.8 m and decay there. Nearly  $4.5 \times 10^{12}$  kaons per year are expected to decay in a 60 m long useful decay region starting from the beginning of the tank. Assuming a branching ratio of  $10^{-10}$  and a 10% detection acceptance for  $K^+ \rightarrow \pi^+ \nu \bar{\nu}$  decay, we can detect  $\sim 90$  signal events over two years of data taking.

In order to study the extremely rare decay in this high rate environment, we need powerful background suppression techniques with precise timing ability.

#### 1.1.3 Main background sources and rejection techniques

There are two main kinds of background sources. Primary backgrounds come from  $K^+$  decays; the other sources are beam-related.

##### Generic $K^+$ decay backgrounds

$K^+$  decays with high branching ratio, shown in Table 1.1, can mimic signal events in some cases. Although the very rare decay  $K^+ \rightarrow \pi^+ \nu \bar{\nu}$  is three-body decay, see Figure 1.4, only one secondary particle is detectable. The signature of the signal event is a  $\pi^+$  track matched in time with a  $K^+$  track. So if only one decay particle,  $\pi^+$ , in  $K^+$  decays were detected with other particles escaping the detection, it might produce the same signal as a  $K^+ \rightarrow \pi^+ \nu \bar{\nu}$  event. It happens when the  $\pi^0$  from  $K_{\pi 2}$  decay is undetected. Besides, backgrounds are also contributed by decay modes which have only one detectable decay particle, like  $K^+ \rightarrow \mu^+ \nu$  ( $K_{\mu 2}$ ). If  $\mu^+$  were tagged as  $\pi^+$  by mistake, it would also mimic a signal event.

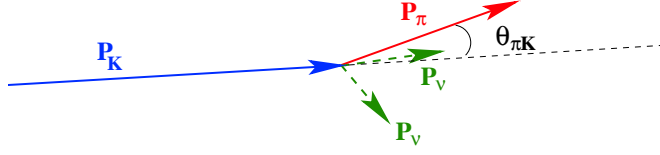


Figure 1.4: Kinematics of the decay  $K^+ \rightarrow \pi^+ \nu \bar{\nu}$ .  $\vec{P}_K$  is the kaon momentum detected by GTK,  $\vec{P}_\pi$  is the pion momentum detected by STRAW, and  $\theta_{K\pi}$  refers to the angle between two tracks.

To achieve the goal of NA62, the Signal-to-background Ratio (S/B) cannot be lower than 10 so that the suppression factor for these kaon decays needs to reach the order of  $10^{12}$ . For this, several techniques were exploited to veto generic  $K^+$  decay backgrounds as shown in Table 1.1: accurate kinematic reconstruction, rigorous particle identification, and powerful decay particle vetoing.

Firstly, kinematics is one of the most discriminating variables for suppressing generic  $K^+$  decay backgrounds. Since  $K^+$  decays have different neutral decay products with each other, we can calculate and use a squared missing mass for backgrounds rejection:

$$m_{missing}^2 \equiv (P_{K^+} - P_{\pi^+})^2 \quad (1.3)$$

where  $P_{K^+}$  and  $P_{\pi^+}$  are four-momentum of the kaon detected by the GigaTracker (GTK, section 2.2.1) and the pion track detected by the STRAW (section 2.2.2). The missing particles are neutral particle which cannot be detected by the STRAW. Given particles are relativistic, and the angles between two tracks are quite small (order of mrad),  $m_{missing}^2$  can be easily calculated as:

$$m_{missing}^2 \approx m_K^2 \left(1 - \frac{|\vec{p}_\pi|}{|\vec{p}_K|}\right) + m_\pi^2 \left(1 - \frac{|\vec{p}_K|}{|\vec{p}_\pi|}\right) - |\vec{p}_K| |\vec{p}_\pi| \theta_{K\pi}^2 \quad (1.4)$$

It should be noted that the detected decay particle is normally assumed as a pion for calculating the  $m_{missing}^2$ . But in some cases, we also assume it has muon mass, i.e.  $m_{missing-\mu}^2 = (P_{K^+} - P_{\mu^+})^2$ , for convenience. As shown in Figure 1.5, three largest background decays,  $K_{\mu 2}$ ,  $K_{\pi 2}$  and  $K^+ \rightarrow \pi^+ \pi^+ \pi^-$  ( $K_{\pi 3}$ ), are well kinematically constrained in the  $m_{missing}^2$  spectrum. Two signal regions can be defined to reject these decay events:

- Region I :  $0 < m_{missing}^2 < m_{\pi^0}^2 - \sigma(m_{\pi^0}^2)$

### 1.1. Overview of the NA62 experiment

- Region II :  $m_{\pi^0}^2 + \sigma(m_{\pi^0}^2) < m_{missing}^2 < \min([m_{missing}^2(K_{\pi 3})])$

where  $\sigma(m_{\pi^0}^2)$  represents the resolution of the  $K_{\pi 2}$  peak to exclude the Gaussian tails. The region I and region II were set to be  $0 \sim 0.01 \text{ GeV}^2/c^4$  and  $0.026 \sim 0.068 \text{ GeV}^2/c^4$  [12]. Due to factors like the resolution effects, the multiple Coulomb scattering and the non-Gaussian tails, backgrounds of the kinematically constrained decays may leak into defined signal regions. A detailed Monte Carlo (MC) simulation of the whole tracking system, based on GEANT4 [13], shows the inefficiencies of kinematics rejection on the decays  $K_{\pi 2}$  and  $K_{\mu 2}$  are about  $5 \times 10^{-3}$  and  $1.5 \times 10^{-4}$ , respectively [2]. However,  $10^{-4}$  is insufficient to achieve the necessary rejection ability ( $10^{-12}$ ). Let alone there are other decay modes, like  $K^+ \rightarrow \pi^0 e^+ \nu_e$ , which cannot be constrained as can be seen in Figure 1.6.

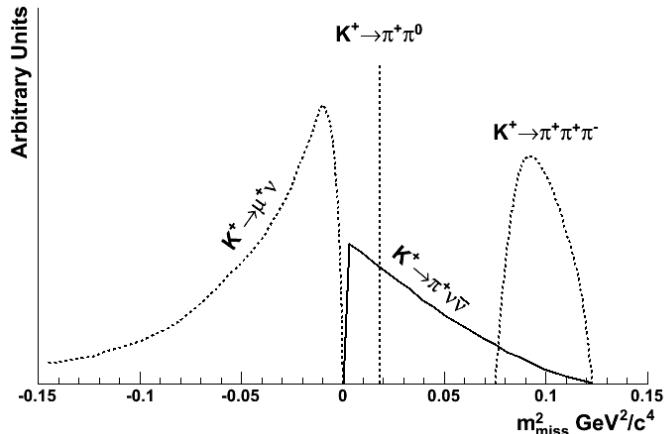


Figure 1.5:  $M_{missing}^2$  distribution under the hypothesis that the detected downstream particle is a pion, for the signal (solid curve) and the kinematically constrained  $K^+$  decays (dotted curves). The spectra are plotted in arbitrary units, not weighted with the branching ratios, and neglecting resolution effects [1].

Further techniques are needed to achieve the rejection goal. Muon veto system described in section 2.4.3 and  $\pi/\mu$  separation achieved by a Ring Imaging Cherenkov (RICH, see section 2.3.2) counter further suppress the decay modes with muons. A powerful photon veto system described in section 2.4.2 is used to detect photons and electrons generated by  $\pi^0$  decays. It rejects the decay modes with  $\gamma$  and  $\pi^0$ . Not only does the liquid Krypton (LKR, see section 2.4.2) electromagnetic calorimeter provide the great

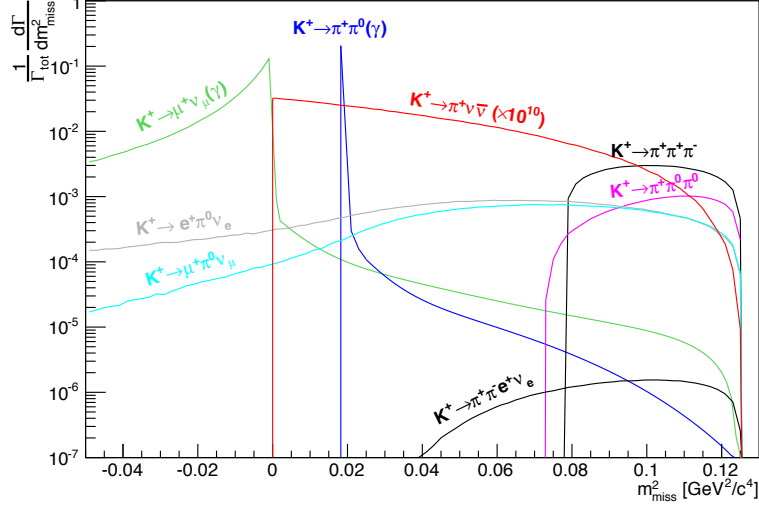


Figure 1.6:  $M_{missing}^2$  distribution under the hypothesis that the detected downstream particle is a pion, for the signal (red line) and generic  $K^+$  decays (both kinematically constrained and not constrained) indicated in other colours. The backgrounds are normalized according to their branching ratio, and the signal is multiplied by a factor of  $10^{10}$  [14].

photon veto ability, but it can also act as a powerful particle identifier for  $\mu^+$  and  $e^+$  which suppress the decays with muons and positrons.

### Beam related background

Besides generic  $K^+$  decays, there are several beam related backgrounds. For example, beam particles undergoing inelastic interaction in the GTK may produce a low-angle  $\pi^+$  detected by the STRAW, which may mimic a signal event. Thanks to the CHANTI, this inelastic interaction can be detected as discussed in section 2.4.1. Besides, mistagging beam particles can also contribute to the accidental background in high rate environment. Like, a beam particle, pion or proton, may be accidentally mistagged as a decaying kaon in the upstream and is unexpectedly associated to a downstream  $\pi^+$  coming from interactions of beam with the residual gas. To avoid this, we need main detectors to have high-resolution timing ability and also an upstream kaon identification detector, a Cerenkov threshold detector (CEDAR, see section 2.3.1), for precisely tagging  $K^+$ .

## 1.2 $K_{\pi 2}$ background study

As shown in Table 1.1, there are two techniques for rejecting the  $K_{\pi 2}$  background: kinematics suppression and  $\pi^0$  vetoing<sup>2</sup>. Although MC simulations were conducted for evaluating the rejection inefficiency of these two techniques, no experimental result has been achieved so far. In this thesis, we analyzed the 2015 physics run data and several MC event samples to achieve the experimental evaluation for two suppression factors, providing the estimated S/B for the  $K_{\pi 2}$  background in NA62.

### Previous simulation results

A MC study suggests that the kinematics inefficiency for rejecting  $K_{\pi 2}$  background is  $5 \times 10^{-3}$  as mentioned in section 1.1.3.

For photon vetoing, a simulation using an estimation of the inefficiency of photon veto detectors based on NA48 experimental measurements indicates that the average  $\pi^0$  veto inefficiency with (without)  $\pi^+$  momentum cut<sup>3</sup> is  $1.6 \times 10^{-8}$  ( $8.4 \times 10^{-8}$ ) [1]. The momentum cut on  $\pi^+$ , 15 to 35  $GeV/c$ , guarantees the  $\pi^0$  has at least 40  $GeV$ . There are four photon veto modules, which are LKr, LAV, SAC, and IRC (see Section 2.4.2), providing a hermetic coverage for photons up to 50 mrad and down to 100 MeV in NA62. Two simulation studies show that destination of photons from  $K_{\pi 2}$  decay can only have three possible configurations: both photons hit the LKr, SAC or IRC; one photon hits the LKr, SAC or IRC and the other one hits the LAV; and one photon hits the LKr, SAC or IRC, and the other one with an angle larger than 50 mrad is undetected. Corresponding fractions of configurations are shown in Table 1.2. The major contribution to the overall photon veto inefficiency comes from the third configuration, containing 0.2% events, where only one photon is detected in the forward direction. Although only one photon is detected, this photon normally has an energy in the 10 GeV range or even more, which makes it easier to be detected.

### 1.3 $\pi^0 \rightarrow \nu\bar{\nu}$ study

The NA62 experiment is like a unique  $\pi^0$  “factory” due to abundant  $K_{\pi 2}$  decays in the fiducial region which provide a great number of tagged  $\pi^0$ . We can take advantage of this enormous  $\pi^0$  sample and powerful photon veto

<sup>2</sup> $\pi^0$  vetoing totally depends on photon veto detectors in NA62.

<sup>3</sup>15 to 35  $GeV/c$ , see section 2.3.2

### 1.3. $\pi^0 \rightarrow \nu\bar{\nu}$ study

	Study 1 [1]	Study 2 [15]
<b>Destination of two photons</b>	<b>Fractions (%)</b>	
Both LKr, IRC, SAC	81.22	80.05
LAV / one of LKr, IRC, SAC	18.58	19.90
One of LKr, IRC, SAC/ Undetected	0.2	0.05 <sup>a</sup>
LAV / Undetected	0	0
Both undetected	0	0

Table 1.2: Destinations of photons from  $K_{\pi 2}$  decay in NA62 from previous simulations

<sup>a</sup>smaller than the result of study 1 since beam pipe is not considered here

ability of the NA62 photon veto system to improve the measurement on the branching ratio of the rare decay  $\pi^0 \rightarrow \nu\bar{\nu}$ .

This decay is forbidden by angular momentum conservation if the neutrino is the purely massless left-handed particle. As demonstrated by the discovered neutrino oscillation [16, 17], neutrinos do have a finite mass. Hence the SM-forbidden decay  $\pi^0 \rightarrow \nu\bar{\nu}$  can occur due to Z-boson exchange shown in Figure 1.7.

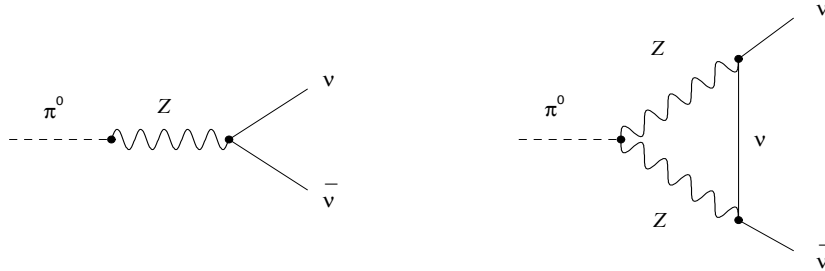


Figure 1.7: Diagrams contributing to the  $\pi^0 \rightarrow \nu\bar{\nu}$  decay. [18]

### Theoretical and experimental branching ratio

The theoretical branching ratio of this rare decay depends on the neutrino mass[19, 20, 21]. It can be given as

$$Br(\pi^0 \rightarrow \nu\bar{\nu}) = 3 \times 10^{-8} \left(\frac{m_\nu}{m_{\pi^0}}\right)^2 \times \sqrt{1 - 4\left(\frac{m_\nu}{m_{\pi^0}}\right)^2} \quad (1.5)$$

for a single neutrino type in the case of Dirac neutrino [22]. Using the upper limit of neutrino mass,  $m_\nu < 0.23$  eV, reported by Planck collaboration [23], the branching ratio of the  $\pi^0 \rightarrow \nu\bar{\nu}$  decay is constrained to be lower than  $1.65 \times 10^{-24}$ , while another study shows it should be lower than  $3 \times 10^{-15}$  assuming  $m_\nu \sim 1$  eV [24].

The present experimental upper limit on the branching ratio of this SM-forbidden decay was set by the E949 experiment with  $Br(\pi^0 \rightarrow \nu\bar{\nu}) < 2.7 \times 10^{-7}$  at 90% confidence level (C.L.) to all possible  $\nu\bar{\nu}$  states [22], which is much larger than what above studies suggested. In E949, the upper limit is entirely determined by how well photons, coming from  $\pi^0$  decays, can be rejected.

In this thesis, we used the similar method but with  $\pi^0$  samples from the NA62 for exploring a new upper limit. With a much more powerful photon detection system in NA62, we are expected to lower this limit to  $10^{-8}$ .

## 1.4 Outline of the thesis

The setup of the NA62 experiment is described in Chapter 2. Chapter 3 presents strategies for studying the  $K_{\pi 2}$  background, and the branching ratio of the rare decay  $\pi^0 \rightarrow \nu\bar{\nu}$ . A set of selection cuts is illustrated in Chapter 4, where the efficiency results of several  $\pi^+/\mu^+$  suppression techniques are also presented. Chapter 5 shows how we set photon veto cuts using a small part of data taken in 2015. Finally, Chapter 6 presents analysis results based on different runs taken in 2015 and Monte Carlo simulations.

## Chapter 2

# NA62 Experimental Apparatus

The layout of the NA62 experimental setup is shown in Figure 2.1. Beam properties are described in section 2.1. There are two tracking detectors for measuring the momentum and position of the  $K^+$  track (section 2.2.1) and  $\pi^+$  track (section 2.2.2). Besides, a particle identification system is used to tag the incident  $K^+$  (section 2.3.1) and distinguish  $\pi^+$  from  $\mu^+$  (section 2.3.2) and  $e^+$  (section 2.4.2). Furthermore, veto modules for rejecting beam background (section 2.4.1), photons (section 2.4.2) and muons (section 2.4.3) are designed to reach the required sensitivity. A detail description of the apparatuses and their working status during the 2015 data taking can be found below.

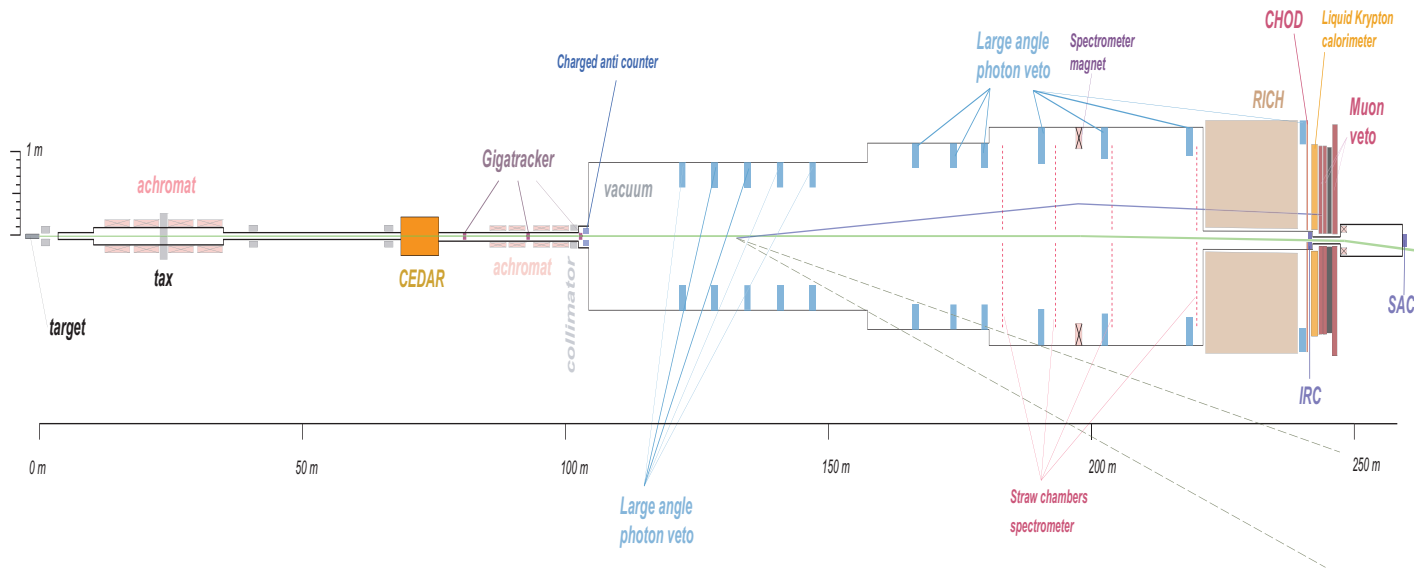


Figure 2.1: Layout of the NA62 experimental setup (scaled model) [25].

## 2.1 Beam line

The SPS is a particle synchrotron accelerator with a circumference of nearly 7 km. It takes particles from the Proton Synchrotron and accelerates them up to 400 GeV/c, providing beams for the LHC and the other three fixed-target experiments including the NA62 in the North Area. As shown in Figure 2.2, the proton beam extracted from the SPS is split onto three target stations (T2, T4, and T6) to generate secondary beams for those experiments. Not all beam particles interact in T4 and T6 stations due to the presence of the magnets. The non-interacted proton beam is then transported via a series of tunnels (P42 beamline<sup>4</sup>) for approximately 823 m to the North Area High Intensity Facility (NAHIF) [26]. At the beginning of the P42, there are two vertically-motorized beam-dump/collimator modules, TAX 1 and TAX 2, whose apertures can be changed to get different proton beam flux intensity.

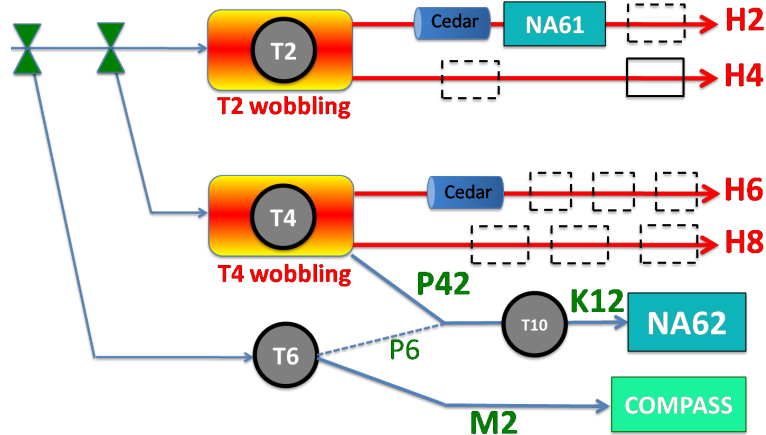


Figure 2.2: This diagram shows how extracted proton beam from the SPS feeds the NA62 experiment.

On the exit of the P42, the proton beam is focused and directed onto a beryllium target in the T10 target station at a zero angle. This beryllium target is a 400 mm long cylinder with a diameter of 2 mm. After interacting with the target, a secondary hadron beam is produced and passes the two

<sup>4</sup>An alternative path for the protons is available via target T6, which joins P42 after ~130 m

## 2.2. Tracking devices

Parameter	Measured	Design value
Average particle momentum (GeV/c)	74.9	75
Proton flux on T10 target per 4.8s spill (full intensity)	$3.3 \times 10^{12}$	$3.3 \times 10^{12}$
Total flux per pulse (full intensity)	$2.2 \times 10^9$	$2.25 \times 10^9$
RMS divergence at CEDAR horizontal (mrad)	0.07	0.07
Fraction of proton in beam (%)	22.4	23
Fraction of $K^+$ in beam (%)	6.6	6
Fraction of $\pi^+$ in beam (%)	70.2	70
Fraction of $\mu^+$ in beam (%)	N.A.	< 1

Table 2.1: Comparison between the measured beam properties in 2015 run with designed values [27]

collimators with an adjustable aperture which select particles with the angle lower than  $\sim 4$  mrad. Beam optics consist of quadrupole magnets (Q1, Q2, and Q3) and a beam dump element consisting of a momentum-defining slit are used to select hadrons with a central momentum of 75 GeV/c ( $\pm 1\%$ ). Also, another series of quadrupole magnets (Q4, Q5, and Q6) serve to preserve the beam alignment and sweep aside external muons and positrons.

The choice of momentum at 75 GeV/c is a result of the trade-off between several factors mentioned in the NA62 technique design [1]. In one word, the purpose is to maximize the accepted rate of the  $K^+ \rightarrow \pi^+ \nu \bar{\nu}$  events in the useful 60 m fiducial region. At the momentum of 75 GeV/c, the ratio of production rate  $K^+/K^-$  is about 2.1, and the ratio of  $\frac{K^+/\pi^+}{K^-/\pi^-}$  equals  $\sim 1.2$ , which is the reason why we chose to use a positive hadron beam rather than negative one. Only 6% of the secondary particles are  $K^+$ , the others are protons and  $\pi^+$ . During the 2015 data taking, the K12 beam line was successfully commissioned. Its properties at full intensity can be checked in Table 2.1. Although it could reach the full intensity, most of the data were taken in low intensity to protect the electronics from the radiation.

## 2.2 Tracking devices

There are two tracking spectrometers; one is placed in the upstream of the decay region for measuring the momentum and position of beam particles, and the other is put in the downstream for detecting charged decay particles. The whole experiment cannot succeed without knowing the precise

## 2.2. Tracking devices

momentum of two tracks, which makes the tracking system an essential part in NA62. Not only does it give the signature of  $K^+ \rightarrow \pi^+ \nu \bar{\nu}$  events, but it also provides the  $m_{missing}^2$  to veto backgrounds of the kinematically constrained decays. Besides, the decay vertex reconstructed by two tracks' momentum is useful for checking whether the decay happens in the fiducial region or not, further suppressing accidental beam background caused by hadronic interactions. With the precise position and direction of the decay particles, tracks can be propagated to other detectors, providing more cross check criteria to reject the background.

### 2.2.1 GTK

The GigaTracker (GTK), operating in the vacuum, measures the momentum of beam particles with a total rate  $\sim 750$  MHz. It was placed along the beam line behind the kaon tagging detector (CEDAR) but before the fiducial region. It is composed of three stations interleaved within four achromat magnets, as shown in Figure 2.3. Each station is a silicon pixel detector with a total number of 18000 pixels ( $300\mu\text{m} \times 300\mu\text{m}$ ) arranged in a matrix of  $90 \times 200$  elements. This configuration provides the precise positions of the charged particles with a spatial resolution of  $\sim 0.087$  mm. The thickness of the pixel is set to be  $200\mu\text{m}$  corresponding to  $0.22 X_0$  (radiation length).

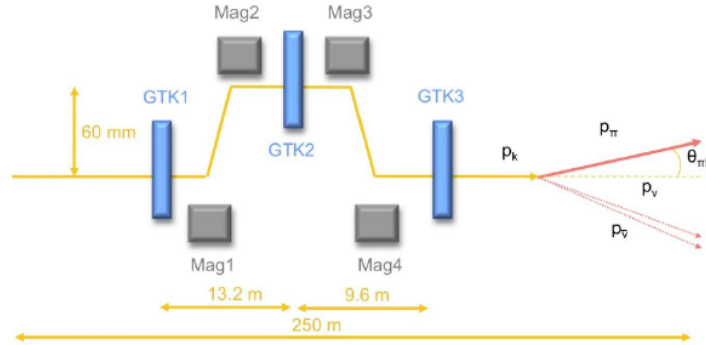


Figure 2.3: Here is the GTK schematic layout. Three GTK stations (in blue) and four dipole magnets (in grey) are visible. The yellow line show the path of the  $K^+$  beam.

To measure the direction and momentum of the charged particles, the first two magnets (Mag1 and Mag2) bent the beam off-axis, and then the

## 2.2. Tracking devices

---

other two magnets (Mag3 and Mag4) reflect it back to its original path. We can measure the value of the momentum by checking how much the off-axis displacement of the beam particle is. The GTK provides a 0.2% RMS momentum resolution and nearly 16  $\mu\text{rad}$  angular resolution [1].

Due to the high rate of particles, and the fact that kaons are ten times less than pions in the beam, a time resolution lower than 200 ps of the GTK must be achieved to avoid accidental background mentioned in section 1.1.3. Thanks to the fast readout electronics consisting of ten Application Specific Integrated Circuit (ASIC) chips [28], the estimated track time resolution using all three stations can be better than 150 ps. In order to reduce the radiation-induced leakage current on sensors, an innovative cooling system circulating a flow of liquid  $C_6F_{14}$  in micro-channels was designed to keep the temperature of the detector at 0  $C^\circ$  (upper limit: 5  $C^\circ$ ).

There are three more beam elements between GTK2 and GTK 3: a muon scraper for sweeping away most of the muon halo from the beam line by means of a toroidal magnetic field, a collimator to clean up the residual hadron halo, and a dipole magnet (TRIM5) to deflect the beam by 1.2 mrad towards positive X <sup>5</sup>.

During 2015 data taking, all three GTK stations were installed but not fully commissioned. Since the readout channels of GTK are noisy in 2015 run, more than 90% events were lost if requesting GTK candidate. But the data with GTK is still enough for investigating the detect's performance, such as the kinematic suppression efficiency for the  $K_{\pi 2}$  background. Except noisy readout, all infrastructure, such as vacuum, mechanics, and cooling, worked properly. The time resolution of three GTK stations measured under the bias voltage <sup>6</sup> in 2015 run is:  $\sigma_{GTK1} = 235$  ps,  $\sigma_{GTK2} = 233$  ps, and  $\sigma_{GTK3} = 257$  ps [27]. This is a little bit worse than the required value, 200 ps, which is caused by the systematic errors of the time offsets.

### 2.2.2 STRAW spectrometer

The STRAW is a spectrometer placed nearly 80 m downstream away from the GTK3 for tracking charged decay particles and vetoing decays, which have multiple charged tracks, like  $K_{\pi 3}$  decay. The Straw spectrometer also works in vacuum to minimize multiple scattering. It consists of four chambers intercepted in the middle by a high aperture dipole magnet (MNP33) providing a vertical B-field of 0.36T for measuring the momentum. A

---

<sup>5</sup>The NA62 reference frame is right-handed, with the Y axis pointing to the zenith and the Z axis on the direction of the beam line.

<sup>6</sup>GTK1 and GTK2 were at 300 V, and GTK3 was at 216V.

## 2.2. Tracking devices

schematic view of the detector is shown in Figure 2.4. Each chamber is made of 1792 straw tubes has two modules providing the measurement of four coordinates  $(x, y)$  and  $(u, v)$  [29], see Figure 2.5. For each coordinate view, it has four layers each with 112 straws. The layout configuration of straws was designed to make sure that at least two hits per view are always present. Straw tubes are filled with working gas  $Ar/CO_2(70/30)$ . They are made of  $30 \mu\text{m}$  tungsten anode wire and  $36 \mu\text{m}$  thick polyethylene terephthalate film coated on the inside with  $0.05 \mu\text{m}$  of Cu and  $0.02 \mu\text{m}$  of Au. Internal diameter and length of tubes are  $9.8 \text{ mm}$  and  $2.1 \text{ m}$ , respectively.

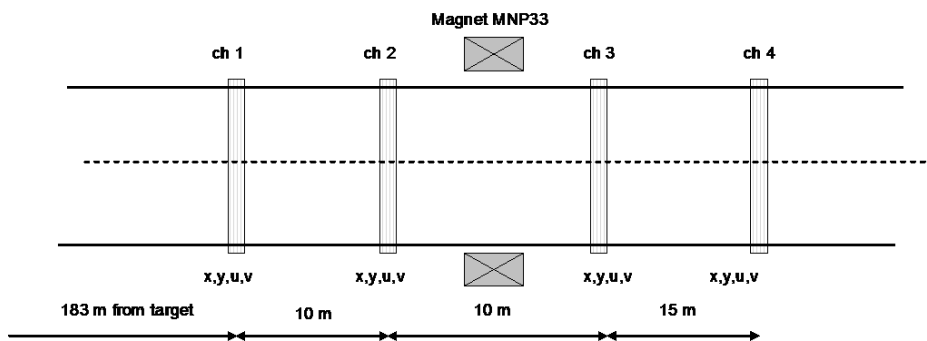


Figure 2.4: Schematic view of the magnetic spectrometer.

MNP33 provides a momentum kick of  $270 \text{ MeV}/c$  towards negative X, roughly compensating for the  $1.2 \text{ mrad}$  deviation introduced by GTK, see section 2.2.1.

To provide enough kinematical constraints, the straw tracker should satisfy two requirements:  $\frac{\Delta P}{P} < 0.01$  and  $\Delta\theta_{K\pi} < 60 \mu\text{rad}$ . For this, the spatial resolution should be better than  $130 \mu\text{m}$  per coordinate. The spatial resolution highly depends on the detector's gain, one of the most important parameters of gaseous chamber. Different working voltage and the gas mixture would end up with different gain values. The first gain measurement of the straw is shown in Appendix A. Besides, a detailed description of the straw readout system can be found in reference [30].

During 2015 data taking, all four straw chambers were commissioned, and all straws except one participated on a regular basis. The time resolution of the STRAW is not so good,  $\sim 5 \text{ ns}$ , that we usually use other downstream detectors, such as RICH or CHOD, to provide the time of downstream track.

### 2.3. Particle identification and timing

---

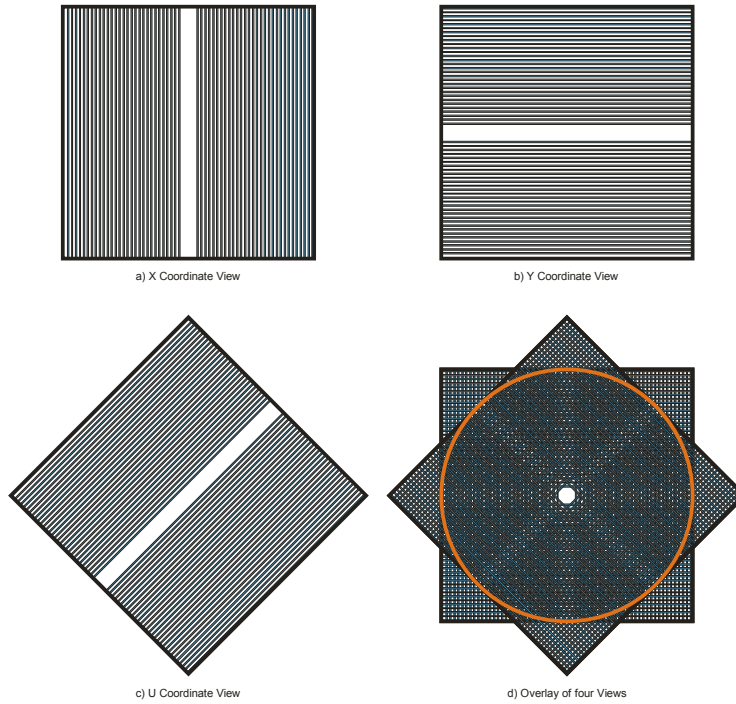


Figure 2.5: Schematic drawing of the four views of each straw chamber. a, b, c show the views of x coordinate with vertical tubes, y coordinate with horizontal tubes and u coordinator with  $45^\circ$  oriented tubes<sup>7</sup>, respectively. d shows a full chamber with all four views.

## 2.3 Particle identification and timing

### 2.3.1 CEDAR

To distinguish kaons from pions and protons in the incoming beam of about 750 MHz particles, a Cerenkov Differential counter with Achromatic Ring focus (CEDAR) was placed before the GTK. The CEDAR is designed to only detect the Cerenkov light produced by particles of kaon mass because the Cerenkov light produced by particles of different masses would have different angles so that it cannot pass optics selection and is absorbed on its way. Overall, the particle rate that the CEDAR observes is nearly 45 MHz.

The CEDAR is a  $\sim 7$  m long vessel filled with hydrogen or nitrogen gas at room temperature, which reduces multiple Coulomb scattering. The

### 2.3. Particle identification and timing

internal optical system consists of a Mangin mirror, a chromatic corrector, lenses and a diaphragm as shown in Figure 2.6. The Cerenkov light emitted by particles is reflected by a spherical Mangin mirror at the end of the vessel; then it passes through a chromatic corrector which makes sure that light of all wavelengths arrives at the same radius onto a ring-shaped diaphragm of 100 mm radius with adjustable aperture width. The aperture was set to only allow the light produced by kaons to hit on the photodetector made of 384 photomultipliers (PMTs) divided into 8 light boxes called octants.

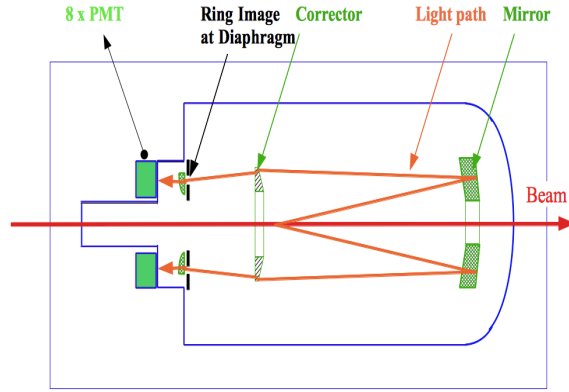


Figure 2.6: Schematic layout of the CEDAR.

The CEDAR detector is required to achieve a kaon tagging efficiency above 95%, with a time resolution of 100 ps, and a contamination of the kaon sample smaller than  $10^{-4}$  [31].

#### 2.3.2 RICH

The Ring Imaging Cherenkov (RICH) is another particle identification detector placed after the fourth straw chamber along the beam line. Its main purpose is to provide a further muon suppression factor of more than 100 by identifying  $\pi^+$  and  $\mu^+$ . The RICH consists of a 17 m long, 4 m wide cylindrical vessel, filled with neon gas at atmospheric pressure. There is a beam pipe inside the vessel to allow free passage to the undecay beam.

A mosaic of 20 mirrors placed at the end of the vessel is used to reflect the Cherenkov light and focus it onto photon detector placed in the front. The mirror mosaic is composed of 18 spherical mirrors of hexagonal shape (350 mm side) and 2 mirrors of semi-hexagonal shape located close to the

### 2.3. Particle identification and timing

beam pipe. The semi-hexagonal mirrors have a thickness of 2.5 cm. These mirrors have a focal length of 17 m. And the photon detector is made of 2000 photomultipliers (PMT) arranged into two groups to avoid the shadow induced by the beam pipe. A schematic layout of the RICH detector is shown in Figure 2.7.

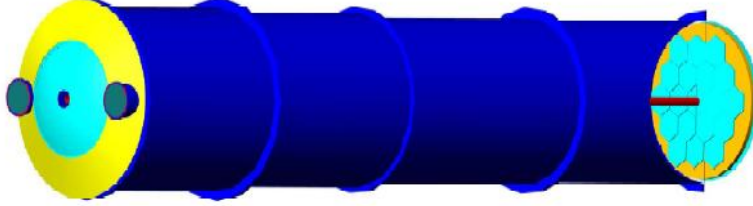


Figure 2.7: Schematic layout of the RICH. A beam pipe is shown in red line, and a mosaic of 20 mirror is visible.

The Cherenkov light emitted by a particle would form a ring on the photon detector. The radius of this ring

$$r = f \tan \theta = f \tan(\arccos(\frac{c}{nv})) \quad (2.1)$$

only depends on the velocity of the particle assume the refractive index ( $n$ ) of gas medium and focal length ( $f$ ) is set. So particles with different mass at same momentum would end up with different radius shown in Figure 2.8. From knowledge of the ring radius in the RICH and particle's momentum measured by the STRAW, the mass of the detected particle can be deduced as,

$$m = \frac{P\sqrt{1-\beta^2}}{c\beta}, \text{ therein } \beta = \frac{1}{n \cos(\arctan(\frac{r}{f}))} \quad (2.2)$$

This is how RICH detector works to identify particles with different masses.

A particle can emit Cherenkov radiation once its momentum is greater than a threshold,  $P_t = \frac{m}{\sqrt{n^2-1}}$ . For the neon gas at atmospheric pressure, this threshold is nearly 12.5 GeV/c. Hence, the  $\pi^+$  momentum should be greater than 15 GeV/c in order to have a full efficiency of detecting  $\pi^+$ . As momentum (velocity) increase, the radius signal of the  $\pi^+$  and  $\mu^+$  would become indistinguishable from each other as shown in Figure 2.8. At same momentum, particles with lower mass, like electrons, are corresponding to larger radius as indicated by Equation 2.2. However, as particle momentum increases,

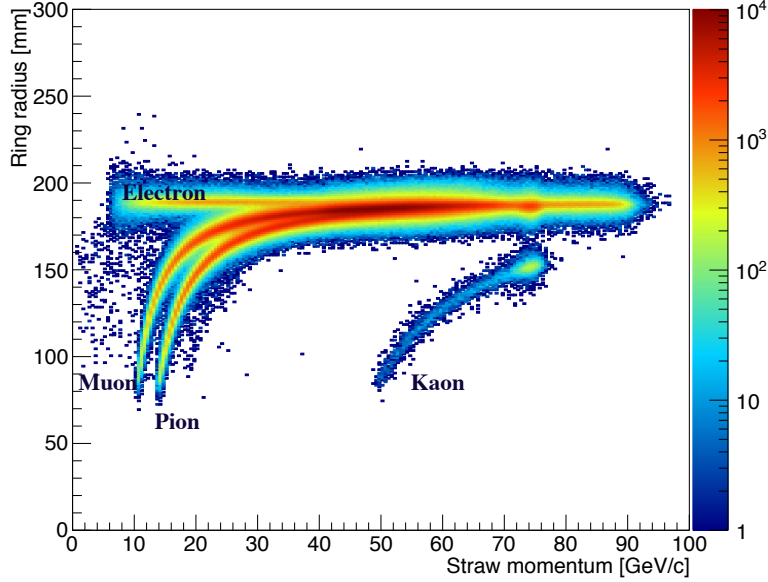


Figure 2.8: Here is the events distribution of fitted RICH ring radius of decay particle versus its straw momentum for a 2015 data run.

the ring radius will reach a limit. When momentum is above  $\sim 35$  GeV/c, it is difficult to distinguish the radius between pions and muons. Hence, the upper limit of track momentum is set to be 35 GeV/c for  $K^+ \rightarrow \pi^+ \nu \bar{\nu}$  study. Overall, the momentum range of straw track for  $\pi^+/\mu^+$  separation is from 15 and 35 GeV/c. A test on a RICH prototype shows the  $\mu^+$  suppression inefficiency is 0.7%, and the time resolution is better than 100 ps averaged over the momentum range [32]. The remarkable timing ability of the RICH makes it a perfect timing device for decay particles. Besides, it can also be used to reject multi-track events and provide a cross-check to the  $\pi^+$  momentum measured by the straw spectrometer assuming the particle is a pion.

It should be noted that mirrors alignment was not optimal during the 2015 run. The taken data indicates that the pion-muon separation factor of RICH is worse than expected; a cut on reconstructed rich mass,  $[0.1325, 0.2]$  GeV/c<sup>2</sup>, rejects 98.51% muons with the pion passing efficiency at 85.31%, see section 4.3.2.

### 2.3.3 CHOD

The Charged particle HODoscopes (CHOD), also used at NA48, is a fast scintillator system which produces signals when crossed by charged particles. It provides information on the positions of the track impact point and precise time with a resolution of nearly 200 ps [33]. This powerful timing ability can be used in the trigger to select decay events with charged particles in the final state. It can also be used to detect photonuclear reactions in the RICH mirror plane. Since the RICH mirror system amounts to nearly 20% of radiation length, it is possible that the high energy photon produced by  $\pi^0$  in  $K_{\pi 2}$  decay would undergo photonuclear interactions with mirror and produce lower energy hadrons which cannot be detected by the LKr, hence increase the photon veto inefficiency. Fortunately, the CHOD, placed after the RICH tank and before the LKr, can detect low energy charged hadrons and re-establish the photon veto sensitivity of the LKr.

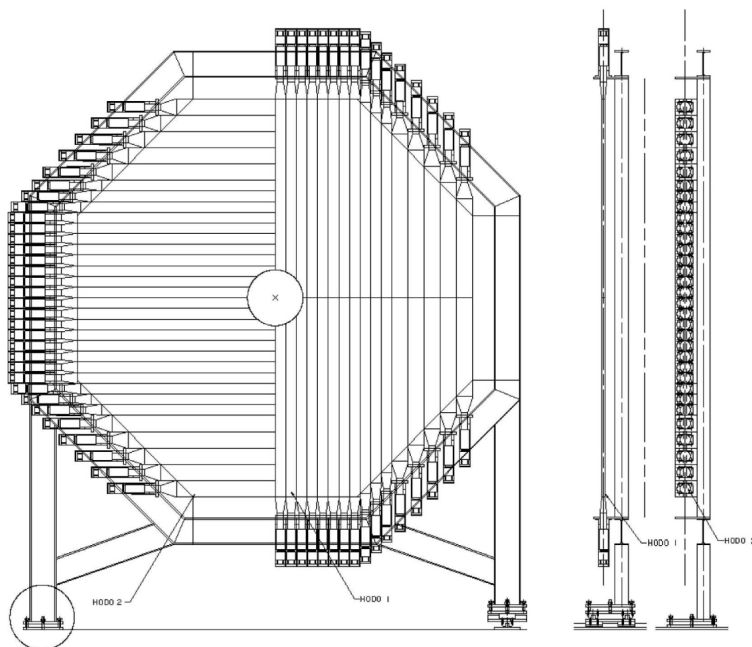


Figure 2.9: Sketch of two planes of the CHOD.

CHOD is composed of 128 plastic scintillator counters which are arranged in two planes, providing x and y coordinates, see Figure 2.9. The upstream plane has 64 vertical counters, while the downstream plane has 64 horizontal

counters. Each plane is divided into four quadrants with 16 counters so that specific triggers could require various combinations of hit locations in each plane. Two planes are separated by around 30 cm. The time difference between two planes' signal can be used to reject fake coincidences caused by the back-scattering from the LKr calorimeter. Each counter has a thickness of 2 cm corresponding to 0.05 radiation length. The length of counters varies from 60 cm to 121 cm and the width changes from 6.5 cm to 9.9 cm [6]. The scintillation light produced by the cross of a charged particle in each counter is read by a Photonis XP2262B photomultiplier (PMT) through a fishtail plexiglass light guide. Four modules of the front-end electronics developed for the LAV are exploited to process CHOD signals [34].

During the 2015 run, the CHOD provides level 0 trigger signal and level 0 reference time to select events. A loose trigger selection requires at least two counter hits within a time window, while a strict one required the coincidence between the signals of at least one vertical and one horizontal counter of adjoining quadrants. The coincidence allows track time to be corrected for the hit impact point. Since the CHOD cannot handle a high hit rate, a new CHOD with a higher level of segmentation was built, see Figure 2.10. It has been installed and is ready for the 2016 run.

## 2.4 Veto system

### 2.4.1 CHANTI

The CHarged ANTIcounter (CHANTI), placed behind GTK, is used to identify inelastic interactions of the beam with the collimator and the GTK stations as well as to tag beam halo muons in the region immediately close to the beam. The critical events are the ones in which inelastic interactions of the hadron beam with the silicon detector of the GTK3 take place. This inelastic interaction would bring in the beam related background in case only  $\pi^+$  of the produced particles is detected by the STRAW. The presence of the CHANTI can reject this event as shown in Figure 2.11. It is shown by a GEANT4 simulation that around 0.1% beam kaons may undergo inelastic interactions with GTK3 [35], so left rejection factors contributed by the CHANTI veto and analysis cuts must reach the  $10^8$  in order to sufficiently suppress this background.

The CHANTI is composed of six square shape stations, placed inside the vacuum tube respectively at 27 - 77 - 177 - 377 - 777 - 1577 mm distance from the GTK3. Each station has a length of 300 mm and a rectangle hole (95 mm×65 mm) present in the centre. It is made of two layers, x

## 2.4. Veto system

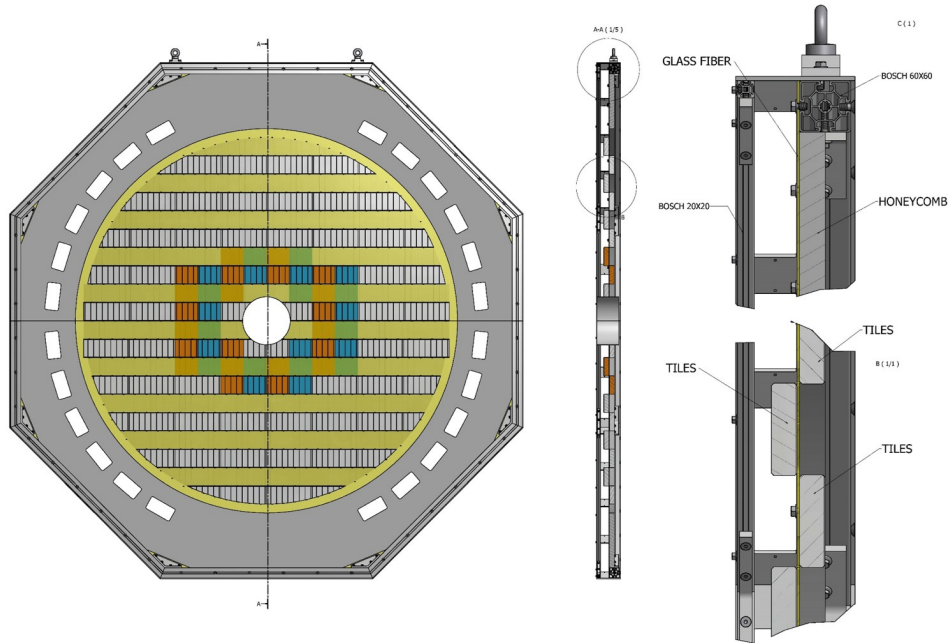


Figure 2.10: Schematic layout of the new CHOD [27].

(y) layer, which is composed of 24 (22) scintillator bars arranged in the vertical (horizontal) direction. Each layer has two sublayers, made of 10+12 (10+14) bars. A schematic layout of a complete CHANTI station is shown in Figure 2.12. For particles hitting the centre of the GTK3, the CHANTI covers hermetically the angular region between 38 mrad and 1.38 rad, while a coverage between 57 mrad and 1.16 rad is expected for the particle hitting the corner of the GTK [35].

To work in the expected detect rate around 2 MHz, the CHANTI must have a time resolution better than 2 ns to keep the random veto rate at an acceptable level. The CHANTI is able to veto about 95% of all kaon inelastic interactions with the GTK3. This vetoing efficiency reaches almost 99% if restricting to potentially signal-like events [35].

During the 2015 data taking period, CHANTI has been working smoothly, and its time resolution is steadily better than 1 ns. The single layer efficiency has been measured to be higher than 99% for straight tracks.

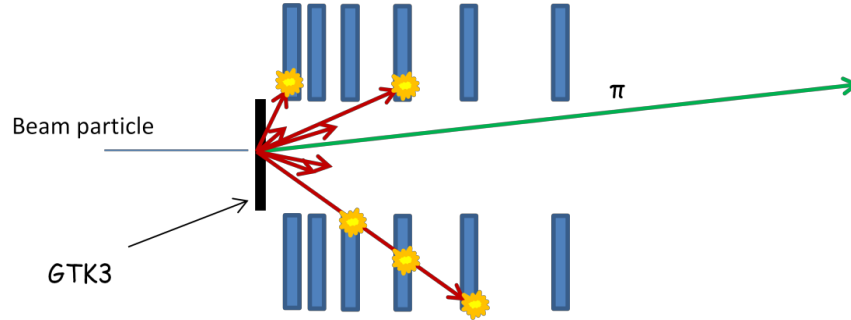


Figure 2.11: This figure illustrates how inelastic interactions of beam with the GTK3 can mimic an event signal. The interactions produces multiple particles including low angle  $\pi^+$  whose path is indicated in green lines. If  $\pi^+$  is the only particle reaching the STRAW, it may mimic a  $K^+ \rightarrow \pi^+ \nu \bar{\nu}$  event signal ( $\pi^+$  matches with  $K^+$ ). However, with the presence of CHANTI shown in blue colour, this event would be rejected due to hits on CHANTI from other particles.

### 2.4.2 Photon veto

The photon veto system is composed of several calorimeters providing nearly complete hermeticity for decay photons with polar angles from 0 to 50 mrad. The large angle region, from 8.5 to 50 mrad, is covered by a system of 12 calorimeters (LAV), while a Liquid-Krypton electromagnetic calorimeter (LKr) covers the angular region between 1 mrad and 8.5 mrad. The other two calorimeters, the IRC and SAC, are used for the angular region below 1 mrad. Overall, the photon veto system must provide a suppression factor of  $10^8$  for rejecting  $K_{\pi 2}$  decays.

#### LAV

The LAV is composed of 12 stations situated between 120 and 240 m (see Figure 2.1). The first eleven calorimeters incorporated into the decay tank work in the vacuum, while the last one is placed after the RICH detector and exposed to air. Each station is made up of four or five rings of lead glass blocks, recycled from the OPAL electromagnetic calorimeter [36]. Figure 2.13 is the picture of the first station, A1, with lead glass installed. The number of the blocks in each station increases from 160 to 256 as the diameter of the stations increases.

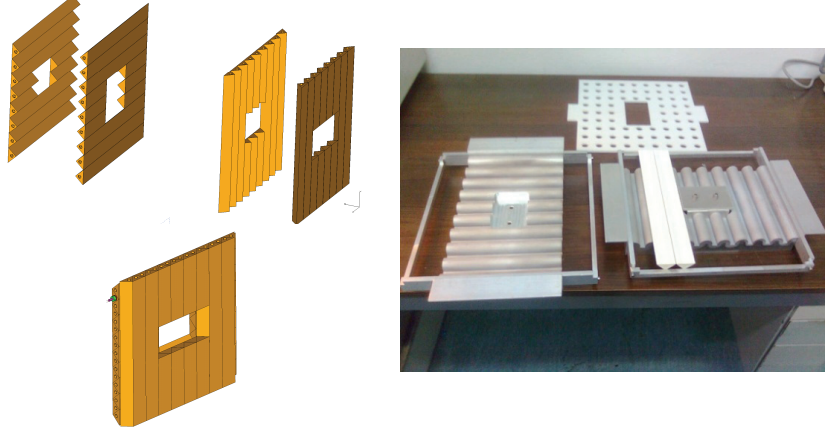


Figure 2.12: A layout of a complete CHANTI station.

The particles crossing the LAV detectors mainly are photons from kaon decays, as well as muons and pions in the beam halo. When photons traverse the lead glass block, produced electromagnetic showers would emit the Cherenkov light which is detected by the PMTs via a 4 cm long cylindrical light guide. A test on the prototype with lead glass modules shows the inefficiency for the detection of the electron is  $1.2_{-0.8}^{+0.9} \times 10^{-4}$  at 203 MeV and  $1.1_{-0.7}^{+1.9} \times 10^{-5}$  at 483 MeV [37], which satisfies the requirement that the detection inefficiency of LAV for photons with energies as low as 200 MeV should reach  $10^{-4}$ .

The LAV provide time and energy measurements based on the time-over-threshold (ToT) technique. Results [6] show the time resolution of a single block is

$$\sigma_t = \frac{220ps}{\sqrt{E(GeV)}} \oplus 140 ps \quad (2.3)$$

and the energy resolution is

$$\frac{\sigma_E}{E} = \frac{9.2\%}{\sqrt{E(GeV)}} \oplus \frac{5\%}{E(GeV)} \oplus 2.5\% \quad (2.4)$$

The readout chain for the LAV is composed of two different types of boards, a dedicated front-end board (LAV-FEE) board and a common digital readout board called TEL62, used by many of the NA62 detectors.



Figure 2.13: Here is the first LAV station which has 5 rings of OPAL lead glass blocks. The glasses are wrapped.

### LKr

The Liquid Krypton Calorimeter (LKr) is a key detector for the NA62 experiment. First, it has powerful photon veto ability. To meet the required photon rejection factor, LKr must have a detected inefficiency better than  $10^{-5}$  for photon with energy larger than 35 GeV. A study shows its photon veto inefficiency is lower than  $0.9 \times 10^{-5}$  at 90% C.L. for detecting photons whose energies are greater than 10 GeV [38]. It also plays an important role in separating muons, pions and electrons which have different deposited properties, such as the size of particle showers and deposited energy over STRAW momentum ( $\frac{E}{p}$ ).

The LKr calorimeter is a quasi-homogeneous ionization chamber [39], filled with liquid krypton at the temperature of 120 K. Its volume is an octagonal cylinder with surface area of  $5.3 \text{ m}^2$  and depth of 1.27 m. The volume was divided into 13248 ionization cells of a cross section  $2 \text{ cm} \times 2 \text{ cm}$  by 18 mm wide,  $40 \text{ }\mu\text{m}$  thick copper-beryllium ribbons which are used as electrodes to collect the ionization signal. An anode was set in the centre of two cathodes as shown in Figure 2.14. A photon or an electron entering the LKr produces an electromagnetic shower composed of low energy photons and electrons which produce a certain number of electron-ion pairs proportional to the deposited energy. The shower is called a cluster, normally encompassing quite a few LKr cells. The number of radiated cells depend

## 2.4. Veto system

on the incident angle and the type of particles.

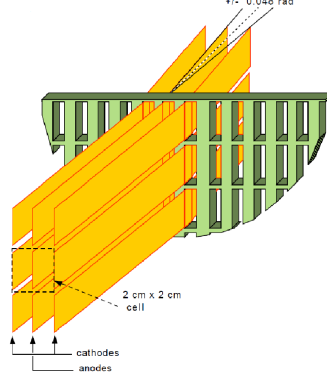


Figure 2.14: Details of the ribbons and electrodes

The LKr also provides the energy, position and time measurement of the particle. The energy resolution of the LKr, measured using an electron beam, can be presented as:

$$\frac{\sigma_E}{E} = \frac{3.2\%}{\sqrt{E(\text{GeV})}} \oplus \frac{9\%}{E(\text{GeV})} \oplus 0.42\% \quad (2.5)$$

For particle energy at 20  $\text{GeV}$ , the energy resolution is around 1%. On the other hand, the space resolution is 1.1 mm in each coordinator, using the test result:

$$\frac{\sigma_{x,y}}{E} = \left( \frac{0.42}{\sqrt{E(\text{GeV})}} \oplus 0.06 \right) \text{cm} \quad (2.6)$$

The time resolution of a single shower is nearly 500 ps.

For working at high rate environment, a new readout system, the Calorimeter REAdout Module (CREAM), is designed and used to provide 40 MHz sampling of 13248 calorimeter channels, zero suppression, and programmable trigger sums for the experiment trigger processor [40].

## IRC

The Inner Ring Calorimeter (IRC) is situated before the LKr. It is a cylindrical tube consisting of two parts: the first one has 25 layers of lead and scintillator, while another has 45 layers. The layout of lead and scintillator is based on the Shashlyk technology: alternating lead and plastic scintillator

## 2.4. Veto system

---

plates as shown in Figure 2.15. The incoming electron or photon interacts with the lead and produces an electromagnetic shower where charged particles produce scintillation light. Then light is then absorbed by fluorescent material and re-emitted to longer wavelengths which can transverse the plastic as attenuation length increases. Finally, the longer wavelength light can be detected by four PMTs via the wavelength shifting fibers. IRC is segmented into 4 parts, hence it has 4 channels.

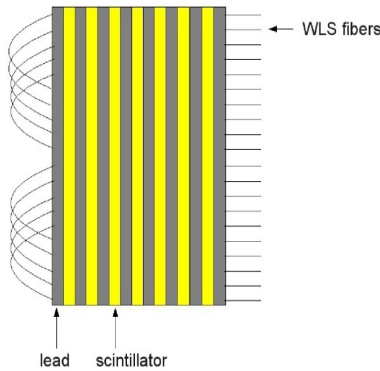


Figure 2.15: Shashlyk technology.

### SAC

The Small Angle Calorimeter (SAC) is placed at the end of the experiment to cover small angular region not covered by the IRC. A magnet located at 248 m from the target is used to deflect the non-interacting charged particles of the beam so that only neutral particles, like photons, can reach the SAC. It also exploits the Shashlyk technology and has four channels.

Both the SAC and IRC are exposed to photons with energies higher than 5 GeV, and must provide the detection inefficiency better than  $10^{-4}$ . During 2015 run, both detectors readout was connected to LAV-FEE and CREAM so they have two readout modules.

### 2.4.3 Muon veto

Muon veto system consists of three detectors, called the MUV1, MUV2, and MUV3, expected to provide a further  $\mu^+$  suppression of the order of  $10^5$  with respect to  $\pi^+$ .

## 2.4. Veto system

---

Although the MUV1 and MUV2 are a part of muon veto system, they are actually hadronic calorimeters instead of fast veto detectors like MUV3. They are used as complementary calorimeters to the LKr, measuring additional deposited energy and also shower shapes of incident particles. Most muons deposit less energy in the LKr and these two hadronic calorimeters than pions do. This can be exploited as a criterion, not significant deposited energy, for distinguishing muons from pions. However, in some cases, muons may also deposit a major fraction of their energy via catastrophic bremsstrahlung or direct pair production. To distinguish these muons from pions, we should compare the difference between the shape of the electromagnetic muon cluster and that of the hadronic pion cluster and find a cut.

The MUV3 is a hodoscope, similar as the CHOD, for detecting non-showering muons. It can act as a fast veto in the level 0 trigger to suppress the high rate of the  $K_{\mu 2}$  decays.

### MUV1-2

The MUV1 and MUV2, placed after the LKr, are classic iron-scintillator sandwich calorimeters with 24 (MUV1) and 22 (MUV2) layers of scintillator strips which are alternatively oriented in the horizontal and vertical directions. Each scintillator layer consists 48(44) scintillator strips in MUV1 (MUV2), the layout of one scintillator plate of both detectors is shown in Figure 2.16.

In the MUV1, there are 23 inner steel layers with a dimension of  $2700 \times 2600 \times 25 \text{ mm}^3$  and 2 outer steel layers with a dimension of  $3200 \times 3200 \times 25 \text{ mm}^3$ . The larger outer layers serve as support for the whole structure and for the WLS fibers, the photon detectors, and the read-out. Each iron plate is separated by 12 mm and contains a central hole of 212 mm diameter to allow the passage of undecayed beam particles. While for MUV2, 23 steel layers have a similar dimension of  $2600 \times 2600 \times 25 \text{ mm}^3$  and also have 12 mm gap and 212 mm diameter central hole. The MUV1 and MUV2 are constructed by simply stacking alternating iron and scintillator layers onto each other. A view of the MUV1 and MUV2 is shown in Figure 2.17.

In the MUV1, the scintillator light is collected by WLS fibers, while the MUV2 routes the light by light guides. The MUV1 and MUV2 calorimeters are read via the same ADC-based CREAM module used by the LKr calorimeter [40].

## 2.4. Veto system

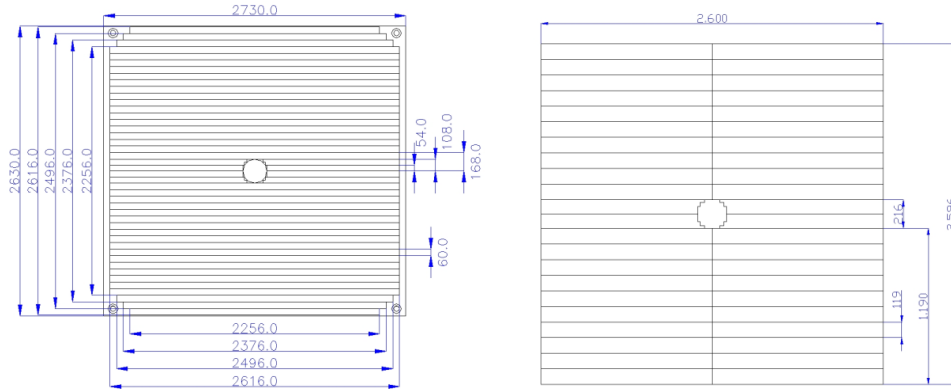


Figure 2.16: Layout of a scintillator plate in MUV1 (left) and MUV2 (right). The dimension of the scintillator strips is indicated in blue number with a unit of mm.

### MUV3

The MUV3 is located after MUV2 and an 80 cm thick iron wall filter. It consists of  $12 \times 12$  scintillator tiles with a dimension of  $220 \times 220 \times 50 \text{ mm}^3$ . The light produced by traversing charged particles is collected by PMTs positioned about 20 cm downstream. Due to this geometry, the maximum time jitter between photons from particles hitting different parts of the scintillator tiles is less than 250 ps, thus preserving the required time resolution of this detector.

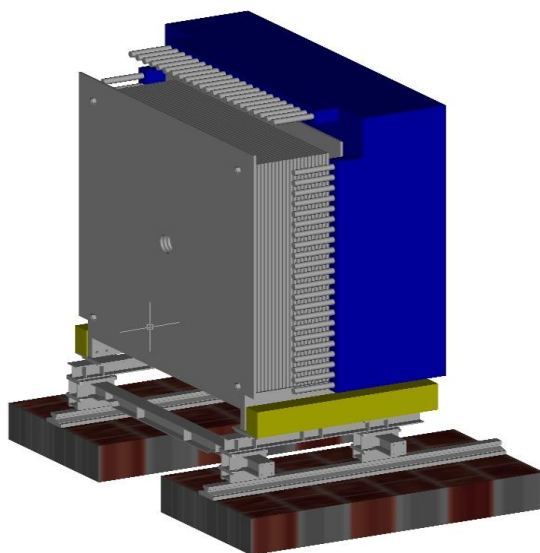


Figure 2.17: A view of the MUV1 (grey) and MUV2 (blue).

# Chapter 3

## Analysis strategies

### 3.1 $K_{\pi 2}$ background evaluation

We have two tools to suppress the  $K_{\pi 2}$  background:  $\pi^0$  vetoing and kinematics suppression. Almost all  $\pi^0$  decay into two photons, so  $\pi^0$  rejection entirely relies on the photon rejection ability in NA62 and is usually referred as photon vetoing. Assuming there is no correlation between rejection factors, the overall rejection level for the  $K_{\pi 2}$  background can be obtained by multiplying two rejection factors with the branching ratio for  $K_{\pi 2}$  decay. The estimated the S/B for the  $K_{\pi 2}$  background in NA62 is:

$$\begin{aligned} S/B &\approx \frac{Br(K_{\pi\nu\bar{\nu}}) \cdot A_{kinematics} \cdot A_{PV} \cdot A_{K_{\pi\nu\bar{\nu}}}}{Br(K_{\pi 2}) \cdot S_{kinematics} \cdot S_{PV} \cdot A_{K_{\pi 2}}} \\ &= \frac{8 \times 10^{-11} \cdot A_{kinematics} \cdot A_{PV} \cdot A_{K_{\pi\nu\bar{\nu}}}}{0.207 \cdot S_{kinematics} \cdot S_{PV} \cdot A_{K_{\pi 2}}} \end{aligned} \quad (3.1)$$

To get the S/B, we first need to assess suppression factors of the kinematics ( $S_{kinematics}$ ) and photon veto cuts ( $S_{PV}$ ) for  $K_{\pi 2}$  events. Then MC simulations should be generated to evaluate the acceptance of selection cuts for both decays ( $A_{K_{\pi 2}}$  and  $A_{K_{\pi\nu\bar{\nu}}}$ ) and the acceptance factor of kinematics cuts ( $A_{kinematics}$ ) for  $K^+ \rightarrow \pi^+\nu\bar{\nu}$  events. Moreover, the acceptance factor of the photon veto cuts for  $K^+ \rightarrow \pi^+\nu\bar{\nu}$  events,  $A_{PV}$ , can be estimated by studying the efficiency of photon veto cuts for rejecting  $K_{\mu 2}$  decays since both decay modes do not have photons in decay products.

#### 3.1.1 Kinematics suppression

The kinematic cut we used is squared missing mass,  $M_{missing}^2$ , defined in Equation 1.3. To get the kinematics suppression factor,  $S_{kinematics}$ , of the kinematic cut for  $K_{\pi 2}$  decay, we first need a pure  $K_{\pi 2}$  sample identified by a series of  $K_{\pi 2}$  selection cuts, listed in section 4.4.1. The momentum of the  $\pi^+$  in the  $K_{\pi 2}$  sample must be within the range from 15 GeV/c to 35 GeV/c, which defines  $K^+ \rightarrow \pi^+\nu\bar{\nu}$  signal region. To make sure we get the accurate result, we used the GTK tracks, rather than the nominal

### 3.2. Upper limit on the branching ratio of the decay $\pi^0 \rightarrow \nu\bar{\nu}$

---

kaons, for calculating  $M_{missing}^2$  even though this costs more than 90% data as mentioned in section 2.2.1. Once acquiring the pure  $K_{\pi 2}$  decay sample, we just need to check how many  $K_{\pi 2}$  events leak into the  $M_{missing}^2$  signal regions. Based on that we can estimate the  $S_{kinematics}$  for  $K_{\pi 2}$  decay.

#### 3.1.2 $\pi^0$ suppression

For studying the  $\pi^0$  suppression,  $S_{PV}$ , we also need a pure  $K_{\pi 2}$  sample in the right momentum range to provide tagged  $\pi^0$ . But  $K_{\pi 2}$  selection cuts used here are different from those for the kinematics study (see section 4.4.2 for the details of selection cuts). The  $\pi^0$  suppression factor in NA62 is expected to reach  $10^{-8}$ , much lower than the expected kinematics  $K_{\pi 2}$  rejection factor,  $10^{-3}$ . So we have to use the nominal kaon tracks with the momentum of near 75 GeV/c in order to get a large number of  $K_{\pi 2}$  events.

The critical part for the  $\pi^0$  suppression study lies in how we set photon veto cuts. Unlike the above kinematics study where  $M_{missing}^2$  signal regions are set in advance (see section 1.1.3), we need to set photon identification cuts based on the response of photon detectors for  $K_{\pi 2}$  events. This process can be biased and brings in large uncertainties. Certainly, wider cuts can increase photon veto efficiency, but it also leads to large accidental veto effects. Fortunately, we can use a  $K_{\mu 2}$  data sample and a  $K_{\pi 2}$  MC sample where  $\pi^0$  was forced to decay into  $\nu\bar{\nu}$  to estimate the false veto effect. Moreover, to avoid bias we can use a set of  $K_{\pi 2}$  events as a training sample to set the photon veto cuts first. And then we can apply these cuts on other (unbiased)  $K_{\pi 2}$  events to check their suppression inefficiency  $S_{PV}$ :

$$\begin{aligned} S_{PV} &= \frac{N_{left}}{N_{K^+} \cdot Br(K_{\pi 2}) \cdot A_{K_{\pi 2}} \cdot C_{False}} \\ &= \frac{N_{left}}{N_{K_{\pi 2}} \cdot C_{False}} \end{aligned} \quad (3.2)$$

where  $A_{K_{\pi 2}}$  is the acceptance of  $K_{\pi 2}$  events,  $N_{K_{\pi 2}}$  is the total number of  $K_{\pi 2}$  events in the unbiased data sample,  $N_{left}$  is the number of remaining events surviving photon veto cuts, and the correction factor  $C_{False}$  which corrects the signal losses due to the false rejection of the photon veto cuts.

### 3.2 Upper limit on the branching ratio of the decay $\pi^0 \rightarrow \nu\bar{\nu}$

This study is similar to the above  $\pi^0$  rejection study because the upper limit on the branching ratio of the SM-forbidden decay is entirely determined by

### 3.2. Upper limit on the branching ratio of the decay $\pi^0 \rightarrow \nu\bar{\nu}$

---

how efficient we can detect  $\pi^0$  in tagged  $K_{\pi 2}$  events as shown below:

$$\begin{aligned}
 N_{K^+} &= \frac{N_{\pi^0 \rightarrow \nu\bar{\nu}}}{Br(K_{\pi 2}) \cdot Br(\pi^0 \rightarrow \nu\bar{\nu}) \cdot A_{K_{\pi 2}(\pi^0 \rightarrow \nu\bar{\nu})} \cdot C_{False}} = \frac{N_{K_{\pi 2}}}{Br(K_{\pi 2}) \cdot A_{K_{\pi 2}}} \\
 Br(\pi^0 \rightarrow \nu\bar{\nu}) &= \frac{N_{\pi^0 \rightarrow \nu\bar{\nu}} \cdot A_{K_{\pi 2}}}{N_{K_{\pi 2}} \cdot C_{False} \cdot A_{K_{\pi 2}(\pi^0 \rightarrow \nu\bar{\nu})}} \\
 &= \frac{N_{left}}{N_{K_{\pi 2}} \cdot C_{False} \cdot \frac{A_{K_{\pi 2}(\pi^0 \rightarrow \nu\bar{\nu})}}{A_{K_{\pi 2}}}} \quad (3.3)
 \end{aligned}$$

Hence, it follows the same analysis strategy as the  $\pi^0$  suppression study, except that we need to consider the difference between acceptance factors of selection cuts,  $\frac{A_{K_{\pi 2}(\pi^0 \rightarrow \nu\bar{\nu})}}{A_{K_{\pi 2}}}$ . It can be computed by comparing the acceptance of select cuts in  $K_{\pi 2}$  MC sample which had common  $\pi^0$  decays with that in another  $K_{\pi 2}$  MC sample where  $\pi^0$  were forced to decay into neutrino pairs.

Besides, the other difference between is that we do not have to apply a  $\pi^+$  momentum cut, [15, 35] GeV/c, for selecting  $K_{\pi 2}$  events here, which enables us to get more  $\pi^0$  events in this study. However, requesting events with high  $\pi^+$  momentum would potentially weaken the photon detection efficiency and the RICH identification ability, so a cut on momentum,  $\leq 40$  GeV/c, is still needed for studying the branching ratio of the decay  $\pi^0 \rightarrow \nu\bar{\nu}$ .

Our study is sensitive to any decays of the form  $\pi^0 \rightarrow$  “nothing”, where “nothing” refers to any system of weakly interacting neutral particles.

## Chapter 4

# Data sample selection

In this chapter, we go through all cuts we used to acquire pure  $K_{\pi 2}$  and  $K_{\mu 2}$  samples. These cuts consist of two parts. The first part contains various cuts used for getting one track events, where a valid straw track is required to match with an upstream CEDAR track and also track candidates of the several downstream detectors. It is a prerequisite step for getting the  $K_{\pi 2}$  and  $K_{\mu 2}$  events samples since both decay modes only have one observable decay track. The second part of cuts contain different combinations of the  $K_{\pi 2}$  or  $K_{\mu 2}$  identification cuts which are applied on one track events to select desired events for different study purposes. There are a few  $K_{\pi 2}$  and  $K_{\mu 2}$  separation techniques contributed by kinematics, photon detection, calorimeters and the RICH. Before setting suitable separations cuts for different studies, we check the efficiency of these identification cuts using one minimum bias run <sup>8</sup> taken in 2015.

### 4.1 Corrections

Before selecting one track events, we need to correct the reconstructed momentum of the candidate in order to account for the change in the field integral of the dipole bending magnet, and for misalignment of the drift chambers. Besides, the reconstructed energy of the LKr cluster must be corrected for non-linearity (zero suppression), energy loss in the entrance window of the cryostat and the global energy scale. The position of LKr cluster should also be shifted for alignment.

#### 4.1.1 Spectrometer momentum correction

The magnetic field correction (parameterized by  $\beta$ ) has the same sign for all tracks, while the correction required for the chamber misalignment (parameterized by  $\alpha$ ) depends on the charge of the track so the correction has the

---

<sup>8</sup>Run: A series of SPS bursts taken under uniform data collection conditions; Each run has its own ID number (a 32-bit unsigned integer).

## 4.1. Corrections

---

form:

$$P_{after} = P_{before}(1 + \beta)(1 + \alpha \cdot q \cdot P_{before}) \quad (4.1)$$

Therein,  $q$  is the charge of the track, and the values of  $\alpha$  and  $\beta$  for each run were determined by reconstructing the invariant mass in the decay  $K^+ \rightarrow \pi^+\pi^+\pi^-$  and comparing it with the nominal kaon mass provided by the Particle Data Group (PDG) [41]. It should be noted that  $\alpha$  and  $\beta$  values vary between runs and can be acquired in the online table <sup>9</sup>. For run 3811,  $\alpha = -10.85 \times 10^{-8}$ ,  $\beta = 1.57 \times 10^{-3}$  when the unit for momentum is MeV.

### 4.1.2 LKr correction

#### 1. Energy (GeV)

- Non-linearity correction if the number of cells in the cluster is greater than 9 [42]:

$$E_{corr1} = \begin{cases} \frac{E_{uncorr}}{0.7666 + 0.0573489 \cdot \ln(E_{uncorr})}, & \text{if } E_{uncorr} < 22 \\ \frac{E_{uncorr}}{0.828962 + 0.0369797 \cdot \ln(E_{uncorr})}, & \text{if } 22 \leq E_{uncorr} \leq 65 \\ \frac{E_{uncorr}}{0.828962 + 0.0369797 \cdot \ln(65)}, & \text{if } E_{uncorr} \geq 65 \end{cases} \quad (4.2)$$

- Global scale factor:

$$E_{corr2} = E_{corr1} \cdot 1.03 \quad (4.3)$$

- Energy loss in the hole depends on the distance of cluster to the centre(D):

$$E_{corr3} = \begin{cases} \frac{E_{corr2} \cdot 0.9999}{0.97249 + 0.0014692 \cdot D}, & \text{if } 140 \leq D \leq 185 \text{ mm} \\ E_{corr2}, & \text{otherwise} \end{cases} \quad (4.4)$$

$$E_{corr4} = E_{corr3} \cdot (1 - r) \quad (4.5)$$

---

<sup>9</sup><https://na62-sw.web.cern.ch/reprocessing>

Therein,

$$r = \begin{cases} 0.0042 - 3.7 \cdot 10^{-4} \cdot D, & \text{if } 140 \leq D < 180 \text{ mm} \\ -0.00211, & \text{if } 180 \leq D < 200 \text{ mm} \\ -0.01694 - 7.769 \cdot 10^{-4} \cdot D, & \text{if } 200 \leq D < 220 \text{ mm} \end{cases}$$

- Energy loss at low energy:

$$E_{final} = \frac{(E_{corr4} + 0.015) \cdot 15 \cdot 0.9999}{15 + 0.015}, \quad \text{when } E_{corr4} < 15 \quad (4.6)$$

2. Position (mm)

$$x_{after} = x_{before} + 1.3 \quad (4.7)$$

$$y_{after} = y_{before} + 0.8 \quad (4.8)$$

## 4.2 One track event selection cuts

In this section, we used data from Run 3811, taken in 2015 with proton beam at 1% nominal intensity<sup>10</sup>, to demonstrate how we set the one track event cuts. We also used the data to check the efficiency of  $K_{\pi 2}$  and  $K_{\mu 2}$  separation cuts in section 4.3.

Nearly four hundred official reconstructed bursts<sup>11</sup> were analyzed. They are reconstructed by the NA62Reconstruction package (version 834). After reconstruction we can easily get access to the information like positions, momentum, and energy of the hits or clusters produced by particles in detectors.

The trigger schemes in Run 3811 are minimum bias triggers: CHOD/3 and CHOD×!MUV3/1, where 3 and 1 are downscale factors. The CHOD trigger, requiring a coincidence of hits from the same quadrant in the horizontal and vertical planes of the CHOD plastic scintillator slabs, guarantees that at least one charged particle reaches the CHOD in the event. The !MUV3 trigger rejects events with the MUV3 hit whose energy is above the threshold. Although the CHOD×!MUV3 trigger kills most  $K_{\mu 2}$  events, both

<sup>10</sup>All 2015 minimum bias run were taken with proton beam at 1% nominal intensity

<sup>11</sup>Burst: the basic data-taking time unit; each burst lasts 3-4 s and is delivered every 30 s (the SPS duty-cycle.)

## 4.2. One track event selection cuts

triggers contribute to  $K_{\pi 2}$  events sample. Hence, we do not have to just select data with CHOD trigger but requesting all data for the analysis. Other 2015 minimum bias runs also have same triggers.

Selection criteria for getting one track event are as follows:

1. Select events with at least one but less than ten spectrometer tracks. The event should have at least one LKr hit and one CHOD hit.
2. Loop over every spectrometer candidate in each event. Select valid spectrometer candidate which satisfies following requirements:
  - (a) Good spectrometer track:
    - Track leaves hits on four straw chambers, i.e.  $N_{chamber} == 4$ , see Figure 4.1.



Figure 4.1: Number of straw chambers hit by downstream track.

- $\chi^2 \leq 20$
  - $|P_{before-fit} - P_{after-fit}| \leq 20 \text{ GeV}/c$ , see Figure 4.2
  - Track has less than two common hits with another spectrometer track
- (b) Track doesn't form a good vertex<sup>12</sup> with another not fake spectrometer track<sup>13</sup>

<sup>12</sup>Good vertex: ( $CDA < 15$ ) mm && ( $60 < Vertex.Z < 200$ ) m && ( $|T_{track1} - T(tracks2)| < 50$  ns)

<sup>13</sup>Fake spectrometer track: ( $N_{chamber!} = 4$ ) && [ $(\chi^2 \geq 30)$  or (has less than two common hits with another spectrometer track)]

## 4.2. One track event selection cuts

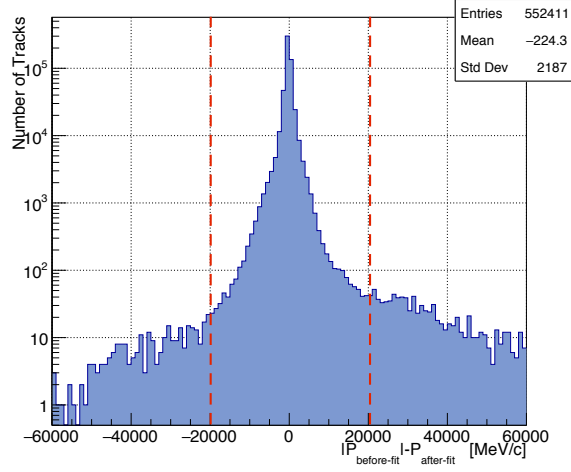


Figure 4.2: Straw momentum difference before and after fit.

- (c) Its linear extrapolated positions on other detectors are within detectors' geometrical acceptance shown in Table 4.1
- (d) Spectrometer track should match with a CHOD candidate. The CHOD candidates are reconstructed at analysis level by pairing two hits from vertical and horizontal planes. Hits are required to be in the same quadrant. Time of the candidate is corrected for T0 and slewing using the same corrections applied at reconstruction level. A best CHOD candidate is selected by minimizing a discriminant  $D_{CHOD}$  [42] which depends on the time difference between two CHOD hits, the time difference between spectrometer time and reconstructed CHOD time, and the distance of extrapolated CHOD position to reconstructed CHOD position.

$$D_{CHOD} = \frac{(T_{CHOD} - T_{track})^2}{(3 \cdot \sigma_{\delta T})^2} + \frac{(T_{Vhit} - T_{Hhit})^2}{(3 \cdot \sigma_{\delta T_{hits}})^2} + \frac{D_{CHOD-to-track}^2}{D_{cut}^2}$$

Therein,  $\sigma$  is the parameter of the fitted gaussian function and  $D_{cut} = 60 \text{ mm}$  as shown in Figure 4.3. A cut on discriminant,  $D < 1.1$ , is set to check whether the spectrometer track match with the selected CHOD candidate or not. If no, then reject this the spectrometer track.

- (e) Spectrometer track should match with a LKr cluster
  - Look for a LKr cluster which is closest to the extrapolated track position at LKr from all reconstructed clusters. And see

## 4.2. One track event selection cuts

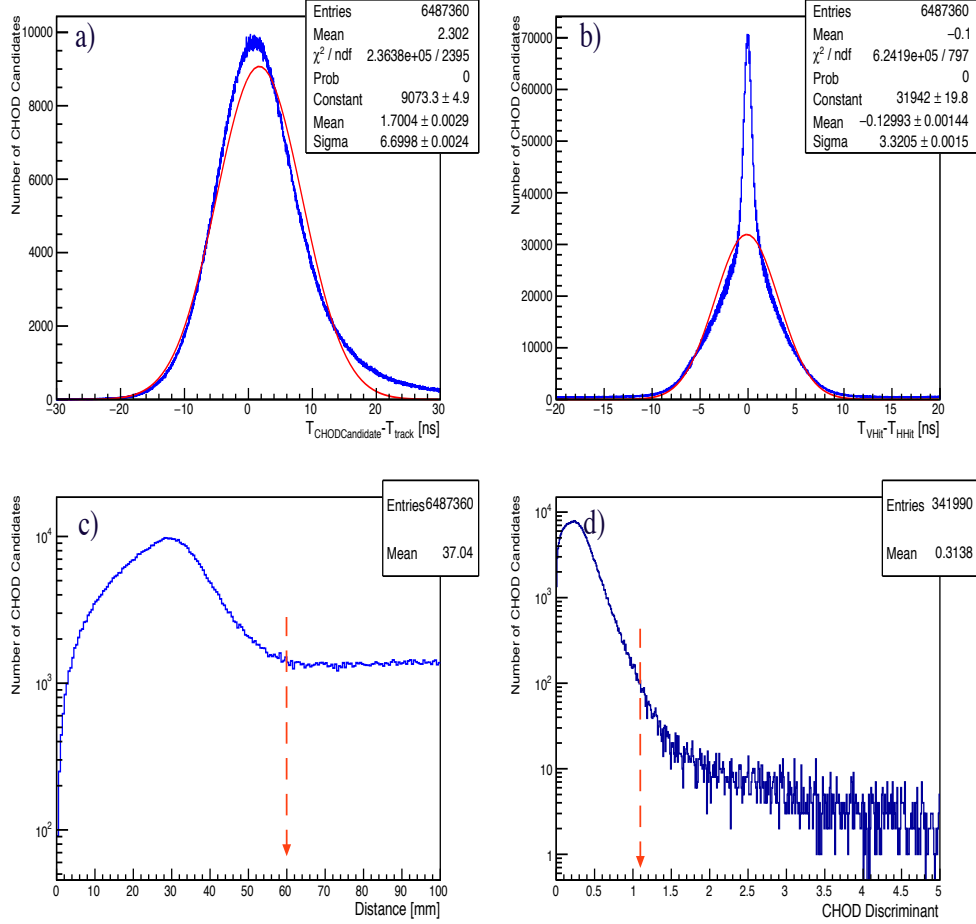


Figure 4.3: Diagrams for matching the CHOD Candidate with the Spectrometer track. a) to c) show the parameters for calculating the CHOD discriminant: a) Time difference between CHOD candidate and spectrometer track with the fitted gaussian distribution whose fitted parameters are shown in statistics table parameters. b) Time difference between CHOD V-plane-hit and H-plane-hit. c) The distance of extrapolated CHOD position to reconstructed CHOD position. The parameter,  $D_{\text{cut}} = 60 \text{ mm}$ , is indicated with red arrow line. d) CHOD discriminant distribution. Red line shows the cut value.

## 4.2. One track event selection cuts

Detector	Geometrical Acceptance Cut
STRAW(4 Chamber Stations)	$75 < D^a < 1000 \text{ mm}$
RICH (Front and end surface)	$90 < D < 1100 \text{ mm}$
CHOD (V and H plane)	$125 < D < 1199 \text{ mm}$
LKr	$D > 150 \text{ mm}$ and within a octagon <sup>b</sup>
MUV1	$130 < D < 1100 \text{ mm}$
MUV3	$130 < D < 1100 \text{ mm}$

Table 4.1: Geometrical acceptance cuts for detectors.

<sup>a</sup>Distance of extrapolated impact point on a detector's station to the centre of that station. It should be noted that the centre of station is not exact (0,0), it varies between detector's station even for the same detector. The position of each centre can be found in Reference [1]

<sup>b</sup>The surface of the LKr is a regular octagon with 1130 mm apothem. It also has a circle hole with the radius of 150 mm in the centre to let undecayed beam particle pass.

whether this cluster can pass the following matched criteria as shown in Figure 4.4:

- $|T_{track} - T_{LKr-cluster}| \leq 20ns$
  - The distance from extrapolated LKr position of the straw track to the position of the reconstructed LKr cluster is less than 150 mm.
  - If no LKr cluster were found, a new LKr cluster is reconstructed at the analysis level by grouping valid LKr hits<sup>14</sup> around the extrapolated impact point of the track on the LKr. The reconstruction succeeds if there is at least one valid LKr hit, and the energy of the most energetic hit is greater than 40 MeV. If this new reconstructed LKr cluster<sup>15</sup> also does not satisfy the above LKr matching criteria, then veto the spectrometer track.
- (f) Spectrometer track should match with a CEDAR candidate. A closest in-time CEDAR candidate is chosen among candidates with  $N_{Sector} \geq 4$ . Time different distribution is shown in Figure 4.5. The spectrometer track would be rejected unless the chosen CEDAR track pass the time cut,  $-2 \leq (T_{CEDAR} - T_{CHOD}) \leq 4 \text{ ns}$ .

<sup>14</sup>Valid LKr hits should satisfy:  $D < 150 \text{ mm}$  &&  $|T_{hit} - T_{track}| \leq 40ns$ .

<sup>15</sup>Its position is the average valid hit positions weighted with energy. Its energy is the sum of all valid hits. Its time is the time of the energetic hit.

## 4.2. One track event selection cuts

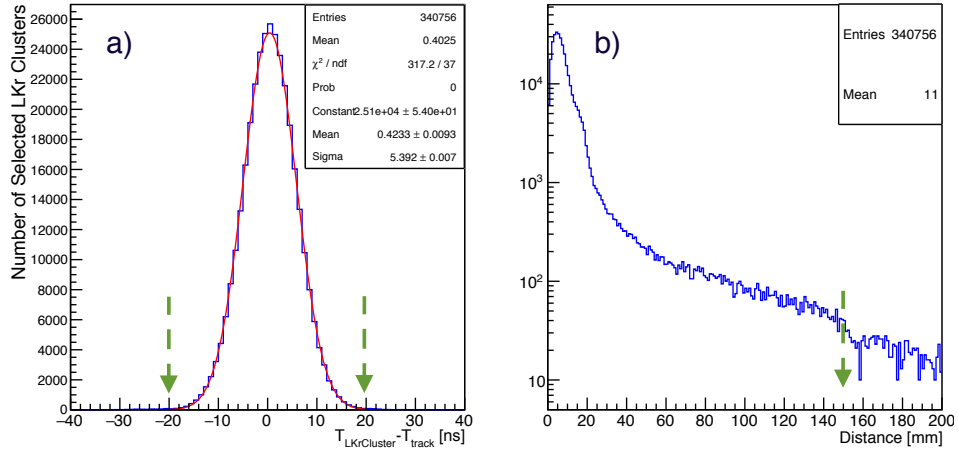


Figure 4.4: Criteria for matching the LKr Cluster with the Spectrometer track. a) time difference between LKr clusters and spectrometer tracks, red line indicates the fitted gaussian distribution b) The distance of extrapolated position of track on the LKr to the centre of the LKr cluster.

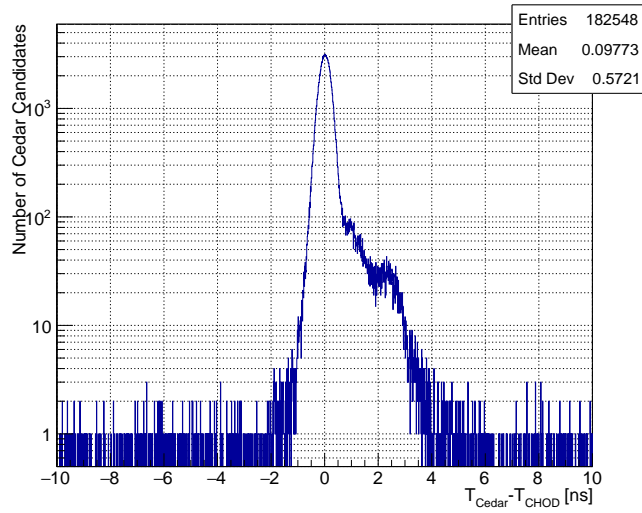


Figure 4.5: Here is the distribution of the time difference between the selected Cedar candidate and the matched CHOD candidate.

## 4.2. One track event selection cuts

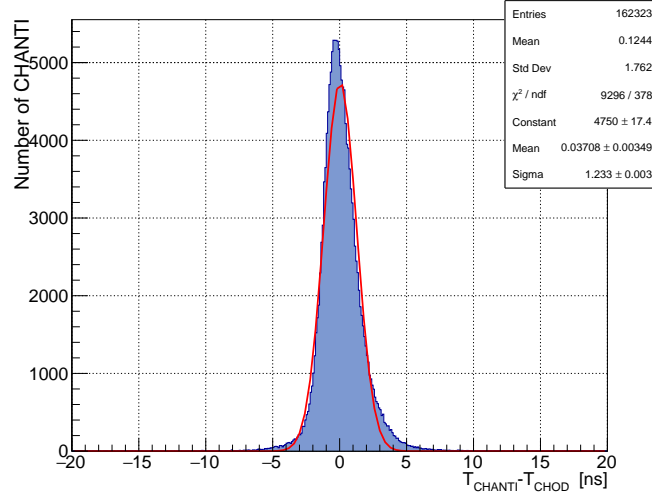


Figure 4.6: Here is the distribution of the time difference between the selected Cedar candidate and the matched CHOD candidate.

- (g) Spectrometer track should not match with a CHANTI candidate. If a CHANTI candidate passed a time cut,  $-6 \leq (T_{CHANTI} - T_{CHOD}) \leq 7 \text{ ns}$ , then reject the straw track. Time difference distribution is shown in Figure 4.6.
- (h) Spectrometer track should match with a RICH candidate (optional). The matching process is similar to that of CHOD candidate. But we considered two types of RICH candidate reconstructed by two different algorithms: multi-ring RICH candidates and single-ring RICH candidates. Multi-ring RICH candidates are reconstructed based on Ptolemy theorem [43] in the standard reconstruction process. A valid multi-ring RICH candidate should have more than three RICH hits and fitted  $\chi^2 < 10$ . In addition, an offset was applied to ring centre to correct the mirror misalignment assuming the light coming from the mirror hit by the spectrometer track. To get a single-ring RICH candidate, the offset corrections were first applied for every hit from a RICH Time candidate<sup>16</sup> at the analysis level and then a least squares fit was redone using these corrected hits. For each type, a best

<sup>16</sup>A group of RICH hits near in time

## 4.2. One track event selection cuts

---

candidate is selected by minimizing a discriminant [42] :

$$D_{RICH} = \frac{(T_{candidate} - T_{track} - \mu_T)^2}{(3 \cdot \sigma_T)^2} + \frac{(D_{candidate} - D_{track})^2}{D_{cut}^2}$$

As shown in Figure 4.7 and 4.8. For multi-ring RICH candidate,  $\sigma_T = 5.12 \text{ ns}$  and  $\mu_T = 0.6 \text{ ns}$ , while for single-ring RICH candidate  $\sigma_T = 5.08 \text{ ns}$  and  $\mu_T = 0.65 \text{ ns}$ . And  $D_{cut} = 13 \text{ mm}$  is set for both types. The distribution of the calculated discriminant is shown in Figure 4.7 c) and 4.8 c) for both types. Cuts on the discriminant,  $D_{RICH-multi} \leq 1.8$  ( $D_{RICH-single} \leq 2.5$ ), and fitted chi-squared,  $\chi^2 \leq 3$ , are set as match cuts.

3. After getting valid spectrometer tracks, we need to check whether the decay happened in the fiducial region or not. We can set cuts on the decay vertex. If straw track passed following vertex cuts, then they would become a one track event.

A decay vertex is defined as the middle of the closest distance (CDA) between the kaon track and selected spectrometer track after blue field correction. There are two ways for setting the kaon track. Firstly, we can select it from GTK candidates which have three hits in three different GTK stations. Among those candidates, a closet in-time GTK track relative to the time of CHOD track was selected to be a GTK kaon candidate. To become a valid GTK kaon track, the candidate must satisfy requirements:  $\chi^2 \leq 40$ ,  $|T_{GTK} - T_{CHOD}| \leq 1.5 \text{ ns}$ ,  $72.7 \leq P_{kaon} \leq 77 \text{ GeV}$ ,  $\theta_x \leq 0.0002$  and  $\theta_y \leq 0.0002$ . If no valid GTK kaon track is found, the event would be rejected. The other way is to set the kaon track as the nominal kaon track assumed using the average momentum near  $75 \text{ GeV}/c$ ,  $\theta_x$  and  $\theta_y$  from the run monitor information in the online table. Obviously, it is more precise to use the GTK kaon track but it costs plenty of data due to noisy GTK readout in 2015. In order to get enough events, the nominal kaon track was assumed for photon veto study in this thesis.

For these two kaon cases, different cuts on the decay vertex were used to select one track event from valid straw tracks.

- Nominal kaon track:
  - (1)  $CDA < 35 \text{ mm}$
  - (2)  $110 \leq Vertex.Z \leq 165 \text{ m}$ , to avoid the decays in the collimator, as shown in Figure 4.9

## 4.2. One track event selection cuts

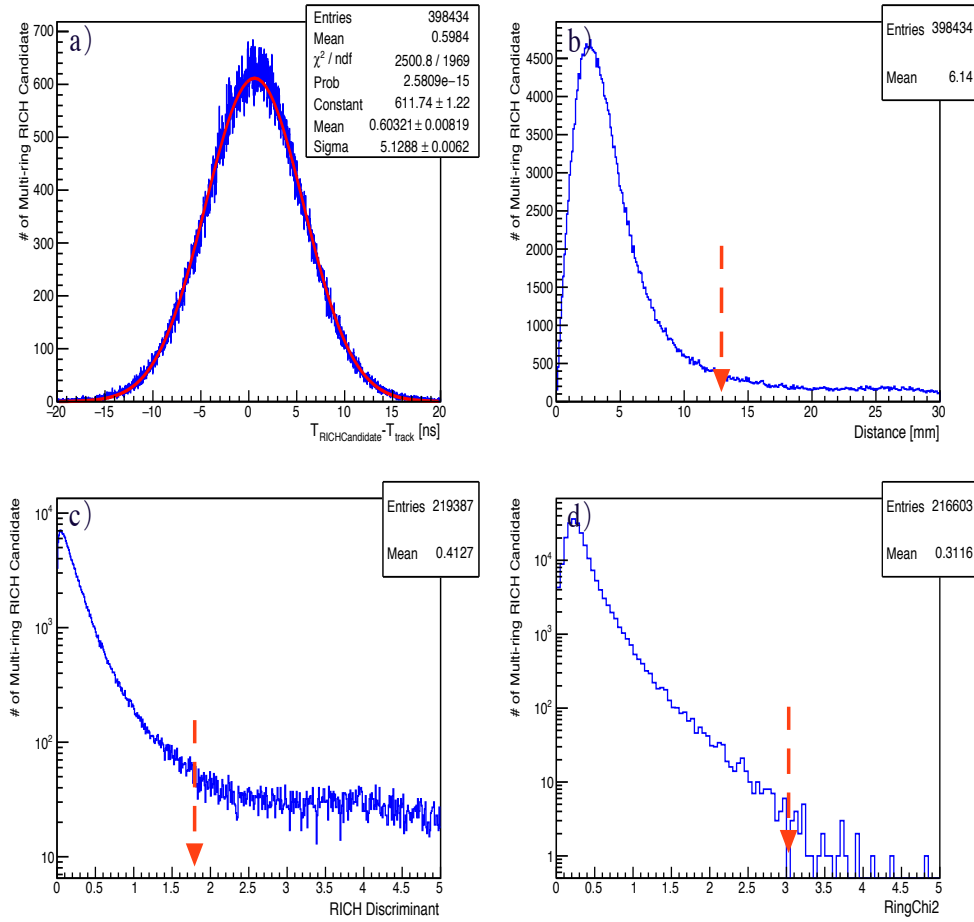


Figure 4.7: Diagrams for matching a multi-ring RICH Candidate with the Spectrometer track. a) time difference between the multi-ring RICH candidate and spectrometer track with the fitted gaussian distribution, fitted sigma is shown in the statistics table b) The distance of extrapolated RICH position to the position of the selected RICH multi-ring Candidate. c) Distribution of the multi-ring RICH discriminant d) Distribution of the fitted  $\chi^2$ . Red lines with an arrow in c) and d) show the match cut.

## 4.2. One track event selection cuts

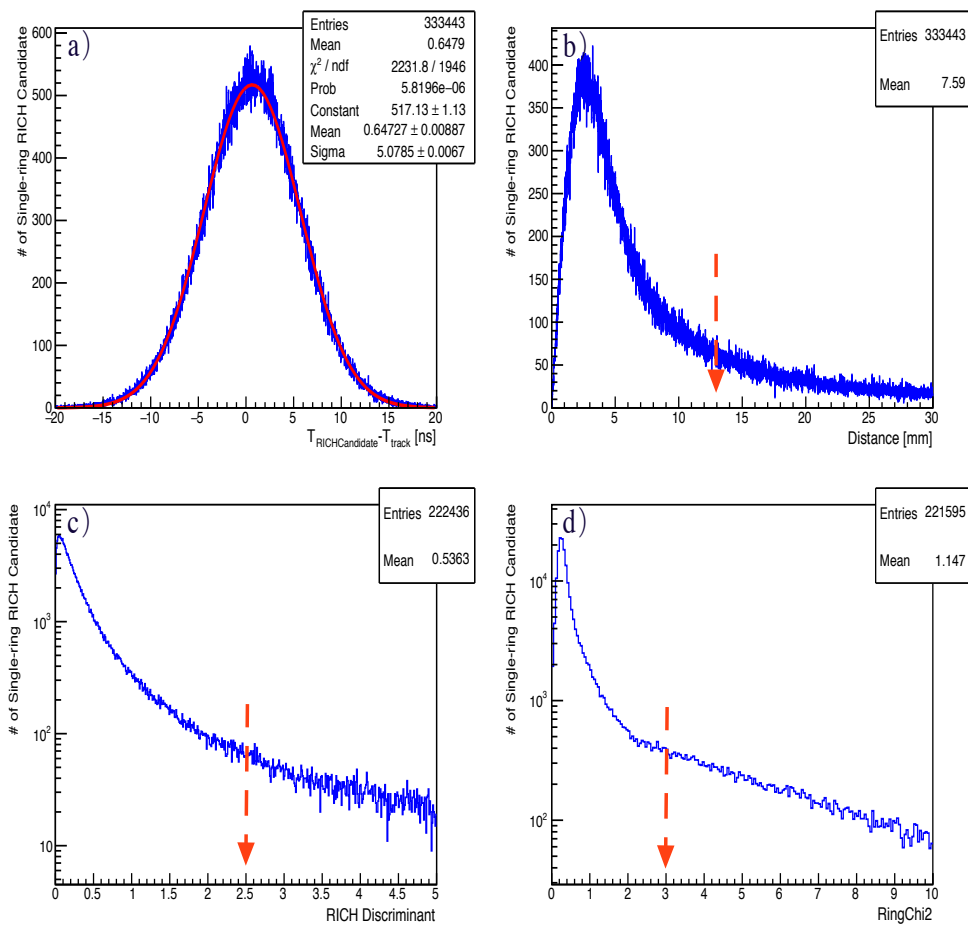


Figure 4.8: Diagrams for matching a single-ring RICH Candidate with the Spectrometer track. Similar as Figure 4.7.

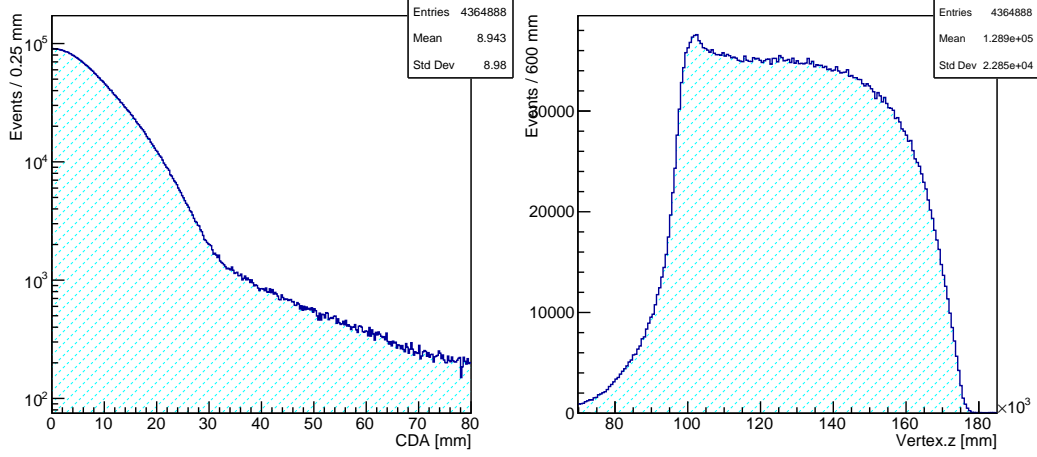


Figure 4.9: Left figure shows CDA of the decay vertex of one track candidates in Run 3811. The vertex was reconstructed using the nominal kaon track and the spectrometer track. Right figure shows the vertex.z distribution.

- Valid GTK kaon track.
  - (1)  $CDA < 7 \text{ mm}$
  - (2)  $105 \leq \text{Vertex.Z} \leq 165 \text{ m}$  , see Figure 4.10.

Once applying above criteria on the data, we get one track events and can start to identify  $K_{\pi 2}$  and  $K_{\mu 2}$  events from them.

### 4.3 $K_{\pi 2}$ and $K_{\mu 2}$ separation cuts and efficiency evaluation

In this section, we present techniques for identifying  $K_{\pi 2}$  and  $K_{\mu 2}$  events. Before using them we should check their efficiency of separating  $K_{\pi 2}$  and  $K_{\mu 2}$ . We used one track events, surviving the above one track event cuts assuming nominal kaon track, from Run 3811 for this study.

#### 4.3.1 Overview of separation cuts

Although both  $K_{\pi 2}$  and  $K_{\mu 2}$  decays can survive one track event cuts, there are a few methods to distinguish them. Some are used to identify  $\pi^+$  and

### 4.3. $K_{\pi 2}$ and $K_{\mu 2}$ separation cuts and efficiency evaluation

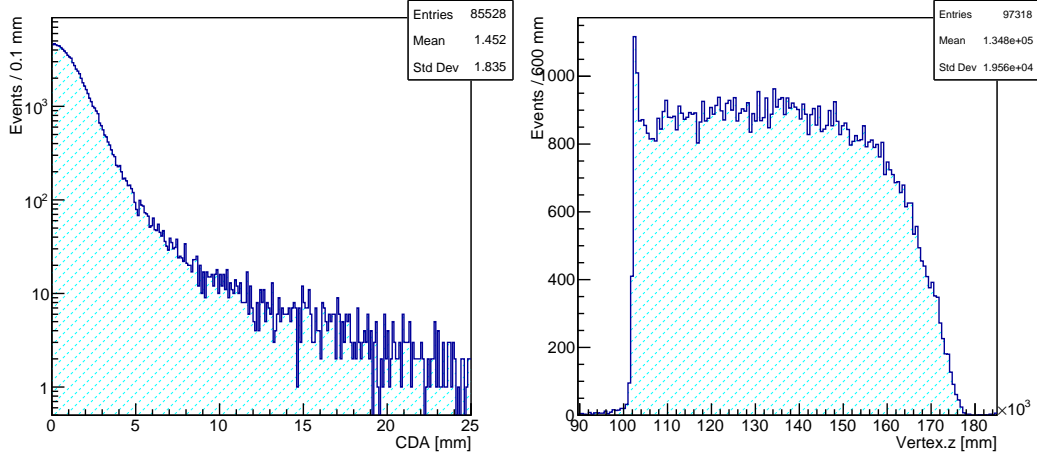


Figure 4.10: Same as Figure 4.9 but the vertex was reconstructed using the GTK kaon track and the spectrometer track.

$\mu^+$ , while other cuts are contributed by distinct properties of  $\pi^0$  and  $\nu$ .

First, different mass between  $\pi^+$  and  $\mu^+$  leads to the discrepancy in RICH signal. We can use Equation 2.2 to calculate the mass of RICH track. The calculated RICH mass distributions of one track events in Run 3811 are shown in Figure 4.11. The left plot shows the mass of RICH multi-ring tracks, and the right is the plot for RICH single-ring tracks.  $K_{\pi 2}$  events are corresponding to the pion peak near  $0.1349 \text{ GeV}/c^2$ , while  $K_{\mu 2}$  events are near the muon mass peak. It can be noticed that though the number of RICH single-ring tracks is less than that of multi-ring tracks, multi-ring mass has worse  $\pi^+$  and  $\mu^+$  separation efficiency. So we only use  $Mass_{RICH-single}$  to set the  $K_{\pi 2}$  and  $K_{\mu 2}$  identification cut.

Apart from the RICH, the electromagnetic calorimeter LKr and the muon veto detector, MUV3, can also be exploited to identify  $\pi^+$  and  $\mu^+$ . As mentioned in Section 2.4.2, different types of particles would deposit different energy in the LKr even though they have same energy. Electrons deposit almost all of energy in the LKr while muons act like Minimum Ionizing Particles (MIPs) and typically deposit only a small fraction of their energy through ionization. Hence, we can use  $\frac{E_{LKr}}{P_{STRAW}}$  (a ratio of deposited energy of track in the LKr to track's straw momentum,  $\frac{E}{P}$ ), to distinguish  $e^+/\pi^+/\mu^+$ . As shown in Figure 4.12, electron normally has  $\frac{E}{P} \approx 1$ , while

### 4.3. $K_{\pi 2}$ and $K_{\mu 2}$ separation cuts and efficiency evaluation

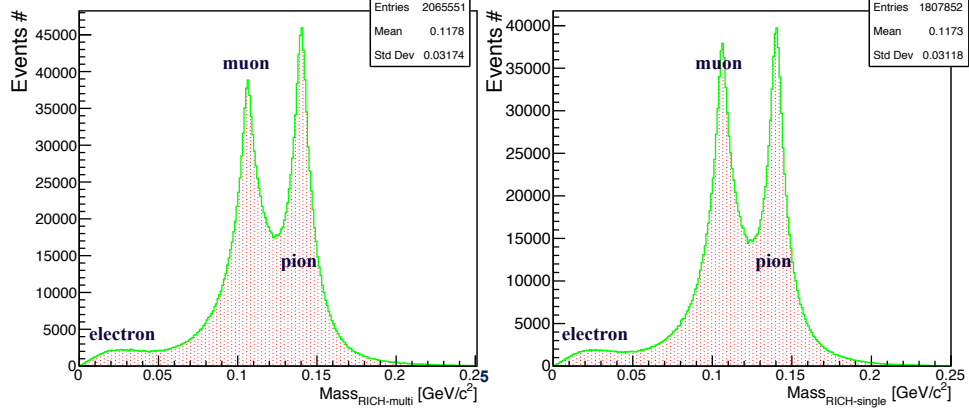


Figure 4.11: Left plot shows the mass distribution of RICH multi-ring candidate for one track events. Right plot is for RICH single-ring Candidate. Pion and muon peaks can be clearly seen in diagram.

muons and pions are corresponding to  $\frac{E}{P} \leq 0.1$  and  $0.1 < \frac{E}{P} < 0.9$ . As for MUV3, almost all pions would be stopped before reaching the MUV3, while most muons can hit it. Hence, we can use it to check whether the track is  $\mu^+$  or not.

In addition, we can use kinematics reconstruction to separate  $K_{\pi 2}$  and  $K_{\mu 2}$  events. Due to the fact that  $\pi^0$  and  $\nu$ , neutral decay product missed by the STRAW spectrometer, have different mass,  $K_{\pi 2}$  and  $K_{\mu 2}$  events would end up with different  $M_{missing}^2$ , the mass squared of missing particles. As shown in Figure 4.13, the  $M_{missing-\pi}^2$  distributions for  $K_{\pi 2}$  and  $K_{\mu 2}$  decays are distinct from each other.  $K_{\pi 2}$  events have the  $M_{missing-\pi}^2$  near the  $Mass_{\pi^0}^2 \approx 0.0182 \text{ GeV}^2/c^4$ , while  $K_{\mu 2}$  events are corresponding to  $M_{missing}^2$  less than 0. We can also assume the straw track has muon mass to get  $M_{missing-\mu}^2$  for convenience sometimes. For example, it is easy to use  $M_{missing-\mu}^2$  for selecting  $K_{\mu 2}$  events since most  $K_{\mu 2}$  events lie at  $0 \text{ GeV}^2/c^4$  in  $M_{missing-\mu}^2$  distribution as shown in Figure 4.14.

Finally, it comes to photon detection. The  $\pi^0$  from  $K_{\pi 2}$  decay can further decay into photons or electrons which can be detected by photon veto detectors, LKr, LAV, IRC, and SAC mentioned in Section 2.4.2. However, for  $K_{\mu 2}$  events, decay product neutrino cannot be observed, i.e., have no matched photon. The cuts for finding photons are discussed in Chapter 5. Photon detection plays an important role in getting pure  $K_{\pi 2}$  and  $K_{\mu 2}$  de-

### 4.3. $K_{\pi 2}$ and $K_{\mu 2}$ separation cuts and efficiency evaluation

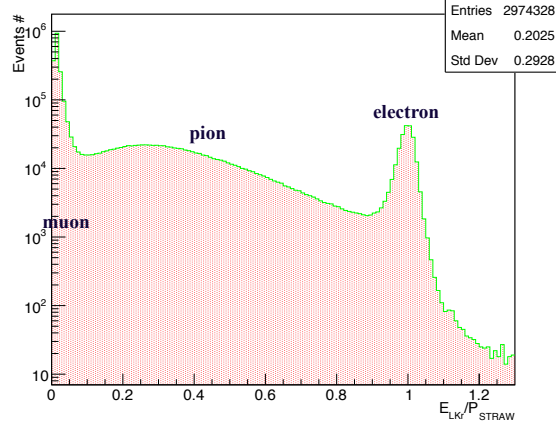


Figure 4.12: The  $\frac{E}{P}$  distribution for one track events.

cay samples for studying the efficiency of above cuts as well as  $S_{kinematics}$  in Section 3.1.1.

In next subsection, we check the efficiency of above techniques except photon veto for separating  $K_{\pi 2}$  and  $K_{\mu 2}$  events.

#### 4.3.2 Efficiency

##### Tight cuts for getting $K_{\pi 2}$ and $K_{\mu 2}$ events

To study the efficiency of one cut, we need to get pure  $K_{\pi 2}$  and  $K_{\mu 2}$  decay samples by applying other three cuts on one track events. The details of cuts are as follows:

- $M_{missing}^2$  cut
  - $K_{\pi 2}$ :  $0.013 \leq M_{missing-\pi}^2 \leq 0.023 \text{ GeV}^2/c^4$
  - $K_{\mu 2}$ :  $|M_{missing-\mu}^2| \leq 0.005 \text{ GeV}^2/c^4$
- RICH single-ring mass cut
  - $K_{\pi 2}$ :  $0.133 \leq Mass_{RICH-single} \leq 0.17 \text{ GeV}/c^2$
  - $K_{\mu 2}$ :  $0.05 \leq Mass_{RICH-single} \leq 0.115 \text{ GeV}/c^2$
- LKr and MUV3 cut
  - $K_{\pi 2}$ :  $0.1 < \frac{E}{P} < 0.8$  and no matched MUV3 candidate

4.3.  $K_{\pi 2}$  and  $K_{\mu 2}$  separation cuts and efficiency evaluation

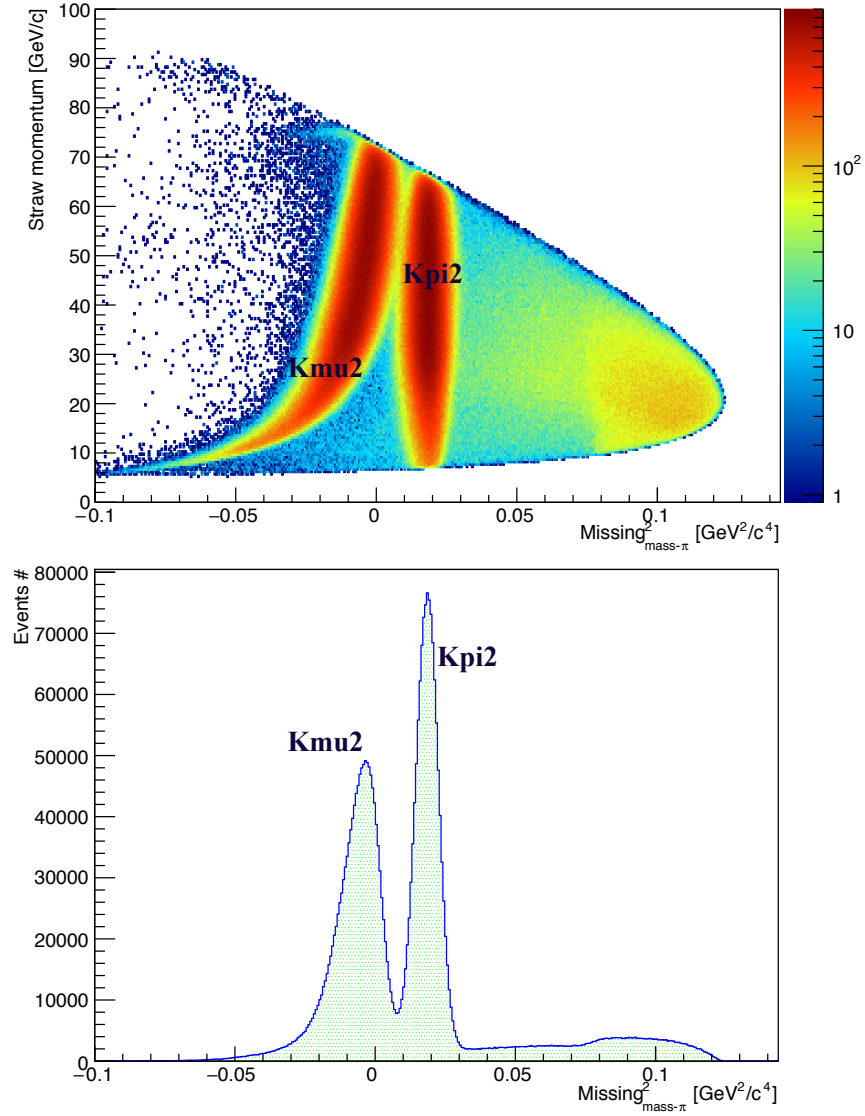


Figure 4.13: Upper plot shows the momentum of straw track versus the calculated  $M^2_{missing-\pi}$  of one track event assuming the straw track has  $\pi^+$  mass. Lower plot is the projection of upper plot in x axis, i.e.,  $M^2_{missing-\pi}$  distribution.  $K_{\pi 2}$  and  $K_{\mu 2}$  decay peaks are denoted in both plots.

4.3.  $K_{\pi 2}$  and  $K_{\mu 2}$  separation cuts and efficiency evaluation

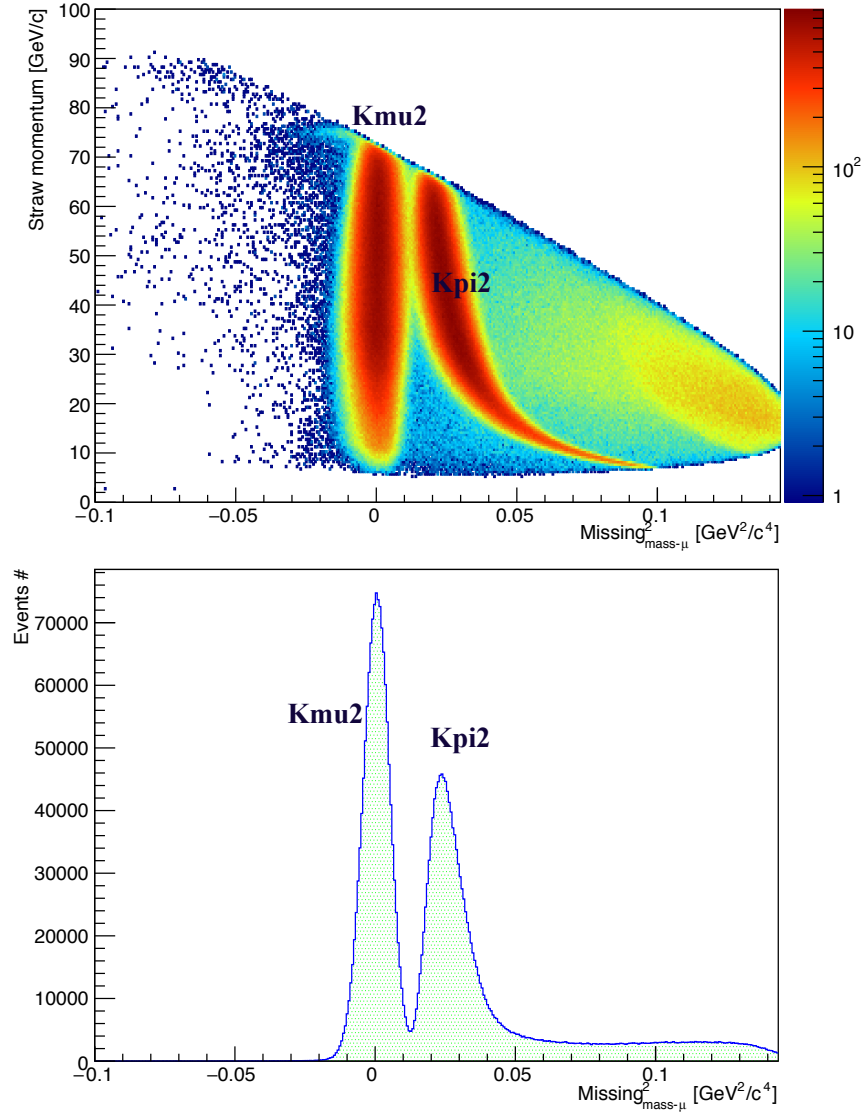


Figure 4.14: Upper plot shows the momentum of straw track versus the calculated  $M_{missing-\mu}^2$  of one track event assuming the straw track has  $\mu^+$  mass. Lower plot is the projection of upper plot in x axis, i.e.,  $M_{missing-\mu}^2$  distribution.  $K_{\pi 2}$  and  $K_{\mu 2}$  decay peaks are denoted in both plots.

### 4.3. $K_{\pi 2}$ and $K_{\mu 2}$ separation cuts and efficiency evaluation

---

$K_{\mu 2}$ :  $\frac{E}{P} \leq 0.1$  and has matched MUV3 candidate

- Photon cut

$K_{\pi 2}$ :

see  $\pi^0$  cut in section 4.4.1

$K_{\mu 2}$ :

No matched photon in the LKr, LAV, IRC, and SAC.

These cuts are stricter than we normally use in order to get fewer background events in the samples.

$M_{missing}^2$

Once applying the sample selection cuts except the  $M_{missing}^2$  cut on one track events in Run 3811, we got pure  $K_{\pi 2}$  and  $K_{\mu 2}$  samples to set efficient  $M_{missing}^2$  cuts to distinguish  $K_{\pi 2}$  and  $K_{\mu 2}$  events. Figure 4.15 shows the  $M_{missing-\pi}^2$  (right) and  $M_{missing-\mu}^2$  (left) distribution for selected  $K_{\pi 2}$  and  $K_{\mu 2}$  events.

We can set a cut,  $0.01 \leq M_{missing-pion}^2 \leq 0.026 \text{ GeV}^2/c^4$ , to select  $K_{\pi 2}$  events. As shown in Figure 4.15 right, the  $M_{missing-\pi}^2$  distribution of  $K_{\pi 2}$  events has a peak at  $0.01819 \text{ GeV}^2/c^4$  which is close to the square value of pion mass  $0.13498^2 \text{ GeV}^2/c^4$ , while  $M_{missing-\pi}^2$  for most  $K_{\mu 2}$  events is less than 0. The resolution of  $M_{missing}^2$  of the  $K_{\pi 2}$  events is about  $4 \times 10^{-3} \text{ GeV}^2/c^4$ , a little bit worse than the design value because nominal kaon momentum was used for calculating  $M_{missing}^2$  rather than that of GTK kaon candidate. Three times better resolution can be acquired if using GTK kaon candidate, see Figure 6.2. To choose a suitable cut, we examine several cuts whose range are  $[0.018-i-n, 0.018+i-n]$  where  $i$  is the step (set it as  $0.001 \text{ GeV}/c^2$  here) and check the  $K_{\pi 2}$  and  $K_{\mu 2}$  passing efficiency of those cuts. The efficiency plot for two situations, non-momentum cut and moment cut (15 to 35  $\text{GeV}/c$ ) on straw track, is shown in Figure 4.16. It is clear that those cuts are quite efficient, with the maximum muon efficiency at  $10^{-3}$  ( $10^{-4}$ ) level before (after) momentum cut. In order to get large statistics and the  $M_{missing}^2$  signal regions (see section 1.1.3) for  $K^+ \rightarrow \pi^+ \nu \bar{\nu}$  events, we chose a cut with wider range,  $[0.01, 0.026] \text{ GeV}^2/c^4$ . This cut has  $(95.17 \pm 0.07)\%$   $K_{\pi 2}$  selection efficiency and  $(2.77 \pm 0.32) \times 10^{-4}$   $K_{\mu 2}$  veto efficiency after momentum cut.

Similarly, we also set a cut on  $M_{missing-\mu}^2$  to select  $K_{\mu 2}$  events. Since we do not need a great number of  $K_{\mu 2}$  events to obtain  $C_{random}$  in section

### 4.3. $K_{\pi 2}$ and $K_{\mu 2}$ separation cuts and efficiency evaluation

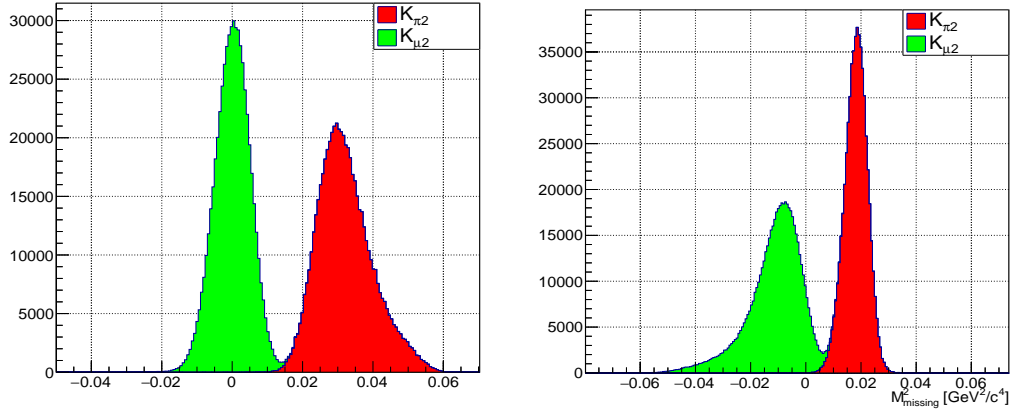


Figure 4.15: The  $M_{missing}^2$  distributions for  $K_{\pi 2}$  (red) and  $K_{\mu 2}$  (green) decay samples. The right plot shows  $M_{missing-\pi}^2$  which was calculated assuming a straw track has pion mass, i.e.  $(P_{K^+} - P_{\pi^+})^2$ , while the left plot shows  $M_{missing-\mu}^2 = (P_{K^+} - P_{\mu^+})^2$ .

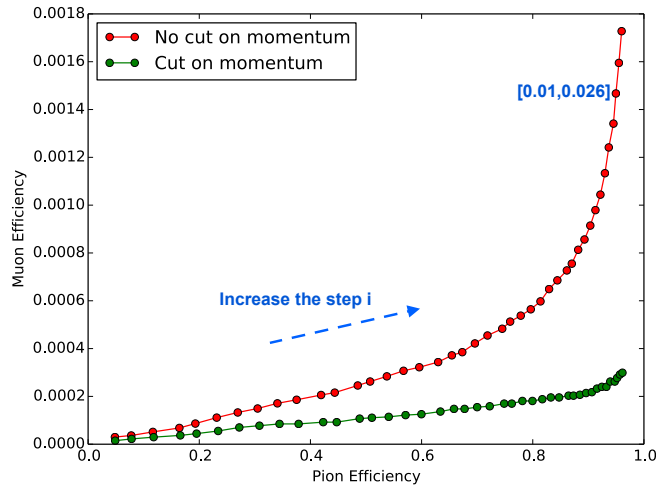


Figure 4.16: Here shows the efficiency of several  $M_{missing-\pi}^2$  cuts for selecting the  $K_{\pi 2}$  sample. The arrow shows the direction of increasing steps.

### 4.3. $K_{\pi 2}$ and $K_{\mu 2}$ separation cuts and efficiency evaluation

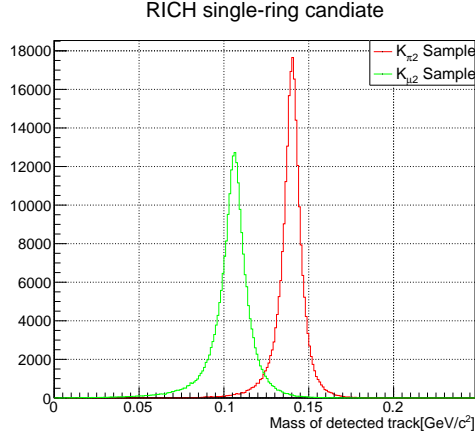


Figure 4.17: The RICH mass distributions for  $K_{\pi 2}$  (red) and  $K_{\mu 2}$  decays (green) sample selected by the other three tight cuts. Only tracks with straw momentum from 15 to 35 GeV/c were chosen in samples. RICH mass was calculated by using the radius of single-ring RICH candidate and straw momentum.

3.1.2, the cut we chose is  $[-0.007, 0.007] \text{ GeV}^2/c^4$  which gives 83.9% (84.5%)  $K_{\mu 2}$  selection efficiency and  $10^{-4}$  ( $2.14 \times 10^{-5}$ )  $K_{\pi 2}$  veto efficiency before (after) momentum cut.

#### RICH single-ring mass cut

The efficiency study of RICH single-ring cut follows a similar process, but we used different selection cuts to select  $K_{\pi 2}$  and  $K_{\mu 2}$  samples. The cuts include  $M_{missing}^2$  cut, calorimeter cut and photon cuts in section 4.3.2 as well as the momentum cut (15 to 35 GeV/c). After getting the samples, we calculated the RICH mass whose distribution is shown in Figure 4.17.

As shown in Figure 4.18, we examine the efficiency of a few RICH mass cuts,  $[0.02 \cdot i, 0.02] \text{ GeV}/c^2$  where the step  $i$  is set as  $0.0005 \text{ GeV}/c^2$ , for selecting  $K_{\pi 2}$  and  $K_{\mu 2}$  events. It is obvious that RICH separation cut is worse than the kinematics. The cut we chose for selecting  $K_{\pi 2}$  is  $0.1325 \leq Mass_{RICH-single} \leq 0.2 \text{ GeV}/c^2$ , which has 85.31% pion efficiency and 1.49% muon efficiency.

While for getting  $K_{\mu 2}$  events, we set  $0.05 < Mass_{RICH-single} < 0.11 \text{ GeV}/c^2$  which has 70.69% muon efficiency and 1.07% pion efficiency.

#### 4.4. Final cuts used for selecting the data sample

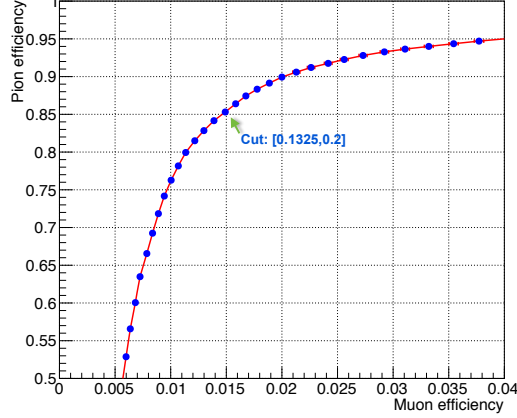


Figure 4.18: This figure shows the efficiency of different RICH mass cuts for selecting  $K_{\pi 2}$  and  $K_{\mu 2}$  events.

#### Calorimeters

Three tight cuts other than the calorimeter cut were used to select the  $K_{\pi 2}$  and  $K_{\mu 2}$  samples. The  $\frac{E}{P}$  distributions for two samples are shown in Figure 4.19. We can set an upper limit at 0.85 to decrease the electron contamination in the pion sample by at least a factor of 200 [44], while a cut  $\frac{E}{P} > 0.1$  is needed to efficiently reject muons. In summary, we can use  $0.1 < \frac{E}{P} < 0.85$  and required no MUV3 matched candidate for selecting  $K_{\pi 2}$  decays. The efficiency of this cut is shown in Table 4.2.

Since we plan to use  $K_{\mu 2}$  events to study the random veto effect of the LKr, we did not use this LKr related cut  $\frac{E}{P}$  for selecting  $K_{\mu 2}$  events. But a cut on matched MUV3 candidates can be used.

### 4.4 Final cuts used for selecting the data sample

In summary, we can use following cuts to select desired events for the different study purposes.

#### 4.4.1 Cuts for kinematics suppression study

For the kinematics suppression study, we need to get a pure  $K_{\pi 2}$  sample from one-track events with valid GTK kaon tracks. Obviously, we cannot use  $M_{missing-\pi}^2$  for selection. The  $K_{\pi 2}$  selection cuts are:

#### 4.4. Final cuts used for selecting the data sample

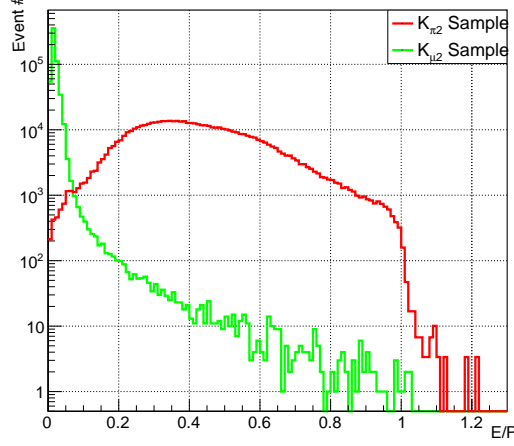


Figure 4.19: The  $\frac{E}{P}$  distributions of  $K_{\pi 2}$  (red) and  $K_{\mu 2}$  (green) decays for run 3811. No cut on STRAW track momentum is set.

- $15 \leq P_{STRAW-track} \leq 35 \text{ GeV}/c$
- $0.1325 \leq Mass_{RICH-single} \leq 0.2 \text{ GeV}/c^2$
- $0.1 \leq \frac{E}{P} \leq 0.85, !MUV3$
- $\pi^0$  cut:
  - Events with only two LKr standard photons but no other photons (see details in Chapter 5).
  - Cut on average time of two photons:  $|T_{photons} - T_{STRAW}| \leq 12 \text{ ns}$ .
  - Cut on the  $\pi^0$  decay vertex reconstructed by using the energy and positions of two photons:  $105 \leq Vertex - \pi^0_Z \leq 180 \text{ m}$ .
  - Cut on the energy of two photons deposited in LKr and MUV1 ( $E_{two-photons}$ ) and energy of  $\pi^+$  track using RICH:  $E_{RICH-track} + E_{two-photons} \geq 70 \text{ GeV}$ .

#### 4.4.2 Cuts for the $\pi^0$ suppression study and $\pi^0 \rightarrow \nu\bar{\nu}$ study

Since the  $\pi^0 \rightarrow \nu\bar{\nu}$  study here entirely depends on the  $\pi^0$  suppression, the procedures for studying the  $\pi^0$  suppression and  $\pi^0 \rightarrow \nu\bar{\nu}$  are almost the same. The difference is that a momentum cut,  $15 \leq P_{STRAW-track} \leq 35$

#### 4.4. Final cuts used for selecting the data sample

Separation cuts	$\mu^+$ Efficiency	$\pi^+$ Efficiency
	15 to 35 GeV/c	15 to 35 GeV/c
	Non-momentum cut	Non-momentum cut
LKr cut: $0.1 < \frac{E}{P} < 0.85$	$(6.45 \pm 0.18) \times 10^{-3}$	$(73.58 \pm 0.13)\%$
	$(5.67 \pm 0.12) \times 10^{-3}$	$(73.51 \pm 0.11)\%$
!MUV3	$(3.38 \pm 0.42) \times 10^{-4}$	$(73.56 \pm 0.11)\%$
	$(2.64 \pm 0.25) \times 10^{-4}$	$(73.48 \pm 0.11)\%$

Table 4.2: Efficiency of LKr and MUV3 cuts for selecting  $K_{\pi 2}$  events and  $K_{\mu 2}$  events

GeV/c, must be applied for the  $\pi^0$  suppression study. Hence, we used the same cuts as follows and leave the momentum cut till the last step for the  $\pi^0$  suppression study. To guarantee the performance of the photon veto detectors,  $P_{STRAW-track} \leq 40$  GeV/c was requested for  $\pi^0 \rightarrow \nu\bar{\nu}$  study.

After applying one-track selection cuts (nominal kaon) on the data sample, we can use the following cuts to select  $K_{\pi 2}$  and  $K_{\mu 2}$  events:

- $K_{\pi 2}$ 
  - $0.01 \leq M_{missing-\pi}^2 \leq 0.026 \text{ GeV}^2/\text{c}^4$
  - $0.1325 \leq Mass_{RICH-single} \leq 0.2 \text{ GeV}/\text{c}^2$
  - $0.1 < \frac{E}{P} < 0.85$ , !MUV3
- $K_{\mu 2}$ 
  - $|M_{missing-muon}^2| \leq 0.007 \text{ GeV}^2/\text{c}^4$
  - $0.05 < Mass_{RICH-single} < 0.11 \text{ GeV}/\text{c}^2$
  - Matched MUV3 candidate

# Chapter 5

## Photon veto cuts

We can set photon identification (veto<sup>17</sup>) cuts by checking the photon detectors' response in a "training"  $K_{\pi 2}$  sample, since almost all photons in the  $K_{\pi 2}$  sample are supposed to leave signals in photon detectors and be detected. In this study, photon veto cuts are time cuts, which can be used to check whether there is a photon detected by four photon veto modules, the LKr, LAV, SAC, and IRC. A photon can leave a cluster in the LKr or a hit in the other three detectors. For each detector, one or several photon candidates were selected for setting photon veto cuts.

The "training"  $K_{\pi 2}$  sample were identified from four 2015 minimum bias runs (3789, 3799, 3801, 3805), which have the same running and trigger conditions as Run 3811, using  $K_{\pi 2}$  selection cuts in section 4.4.2. For executing a "blind" analysis, these  $K_{\pi 2}$  events were not included in the final result for  $\pi^0$  rejection.

No matter how we set photon veto cuts, there is always false veto effect due to the presence of additional  $\pi^+$  clusters in the LKr and the noise in all photon detectors. As it shown in section 5.4, a MC simulation and a  $K_{\mu 2}$  sample identified by cuts in section 4.4.2 from Run 3809 were used to evaluate the additional false rejection factor caused by the accidental rejection of photon veto cuts.

### 5.1 LKr photon

#### 5.1.1 LKr standard photon

A LKr standard photon is an in-time LKr cluster reconstructed by the standard algorithm. Beside the photon from  $\pi^0$  decay, a  $\pi^+$  track can also leave one or several clusters in the LKr. To make sure a LKr cluster did come from a photon rather than a  $\pi^+$  track, we had to define a circular region, with the centre at the projected position of the  $\pi^+$  track in the LKr, which

---

<sup>17</sup>In the  $\pi^0$  suppression study, the event would be rejected once it has a identified photon. So we consider photon identification as photon veto.

## 5.1. LKr photon

---

was masked for searching LKr photon candidates. In other words, we believed all LKr clusters inside this circular region were associated with the  $\pi^+$  track, and all other LKr clusters beyond this region became LKr photon candidates. However, it is possible that additional LKr clusters left by  $\pi^+$  track may exist outside this region and mimic photons. Hence, we need to consider the rejection effect brought by additional  $\pi^+$  LKr clusters as a contribution to false veto factor,  $C_{False}$ . The larger the radius of the masked region is, the smaller the chance of the false rejection would be. As demonstrated by a MC study in Appendix B, nearly 5.64% of  $K_{\pi 2}$  events were rejected by  $\pi^+$  clusters if the radius of the circular region were set to be 150 mm, which leads to  $C_{False-\pi^+} = 94.36\%$ .

Figure 5.1 shows the time difference between the LKr photon candidates and the associated CHOD track of all  $K_{\pi 2}$  training events for two energy ranges. We can set time cuts to identify a LKr photon among selected LKr photon candidates. For candidates whose energy is lower or equal to 2 GeV in Figure 5.1 left, a time cut was set as  $-5 \leq T_{LKr-Cluster} - T_{CHOD} \leq 8$  ns (i.e. [-5, 8] ns) to check if they are LKr photons, while two time ranges [-11,16] ns and [-30, -20] ns were set for left LKr photon candidates having larger energy due to several peaks shown in Figure 5.1 right. As long as only one LKr photon candidate satisfied time cuts, we believed there was a photon presented in the event.

### 5.1.2 LKr extra photon

Since LKr standard reconstruction for 2015 runs was reported to be inefficient for detecting photons, an alternative LKr reconstruction was used as a supplementary photon veto cut after all LKr, LAV, SAC and IRC photon cuts. Details of the algorithm can be found in meeting report [45]. The alternative LKr reconstruction was only activated when there was no standard LKr photon.

Among all newly reconstructed clusters which are 150 mm away from the projected position of the  $\pi^+$  track in the LKr, the most energetic cluster was selected to become a LKr extra photon candidate in every event. For avoiding large noise, this candidate should have energy greater than 1 GeV otherwise no LKr extra photon was identified. Figure 5.2 shows the time difference distribution of all LKr extra photon candidates relative to CHOD tracks in “training”  $K_{\pi 2}$  events. A slightly wider time cut, [-8, 6.5] ns, was set to identify the LKr extra photon.

## 5.2. LAV photons

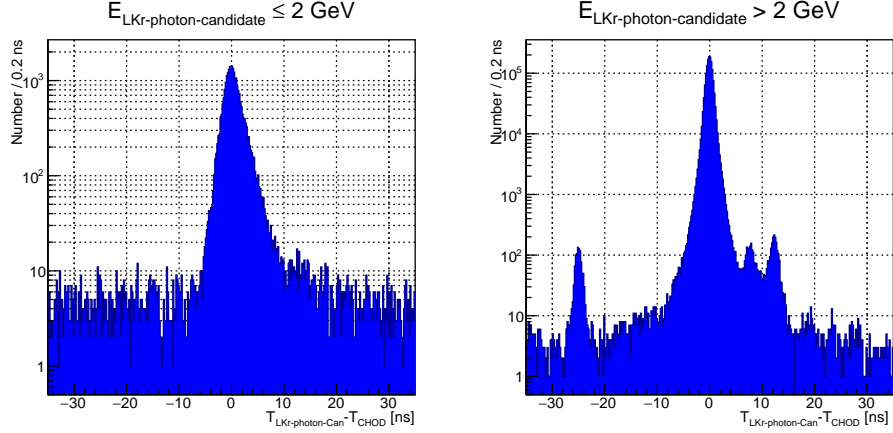


Figure 5.1: Distribution of the time difference between the LKr photon candidates and the associated CHOD track for candidates whose energy is  $\leq 2$  GeV (left), and  $> 2$  GeV (right) in all “training”  $K_{\pi 2}$  events. There are more peaks in the right diagram so a wider time window is required.

## 5.2 LAV photons

LAV photon is an in-time LAV hit. Among all reconstructed LAV hits, only hits with specific edge-combination types were considered [46]. Besides, a valid hit should not come from the identified noisy LAV channels in 2015 run. Among all valid LAV hits in every  $K_{\pi 2}$  event, only the closest-in-time hit relative to the CHOD time was selected to become the LAV photon candidate. Figure 5.3 shows its timing information for corresponding LAV stations. If hit candidates come from the station LAV12, two time cuts,  $[-3.5, 7]$  ns and  $[12, 21]$  ns, were set for checking whether candidates are LAV photons or not. While for candidates from the other stations, a time cut,  $[-5, 5]$  ns, should be set.

## 5.3 SAC and IRC photons

Like the LAV photon, SAC and IRC photons are also in-time hits. But there are two readout modules for small angle veto (SAV) detectors: the LAVFEE and the CREAM board [47]. As can be seen in section 6.2, we treated CREAM based SAC photon veto cut as a supplementary cut and put it after SAV-CREAM photon rejection cut.

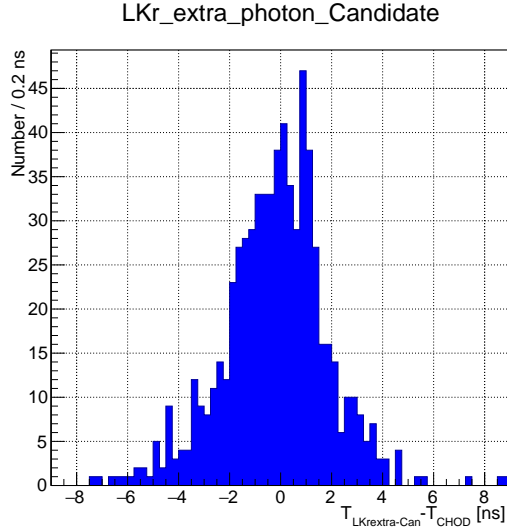


Figure 5.2: Distribution of the time difference between the LKr extra photon candidates and the associated CHOD tracks in all “training”  $K_{\pi 2}$  events.

### 5.3.1 SAV-LAVFEE photons

There is no reconstructed energy information for LAVFEE based hits. But we can exploit the time-over-threshold (TOT) value which is almost proportional to deposit energy [48, 49]. Among all LAVFEE based SAC hits in every event, we selected one hit having the largest TOT value as LAVFEE based SAC photon candidate. Same for the IRC. Figure 5.4 left and right shows the timing of LAVFEE based SAC photon candidates and LAVFEE based IRC photon candidates in  $K_{\pi 2}$  events from run 3801, respectively. Time cuts,  $[-5, 5]$  ns and  $[-6.5, 6.5]$ , were set for identifying (rejecting) SAC photons and IRC photons, respectively.

### 5.3.2 SAV-CREAM photons

Unlike LAVFEE, we do have the energy of CREAM based hits. Energy cuts,  $\geq 1$  GeV and  $\geq 2.5$  GeV, was placed on SAC and IRC hits, respectively, to reduce noise. As a supplementary cut to LAVFEE, we selected the closest-in-time hits instead of the most energetic hits as photon candidates. As you can see in Figure 5.5,  $[-5, 5]$  ns and  $[-8, 8]$  ns can be set for identifying CREAM based SAC photons and IRC photons.

#### 5.4. False veto effect

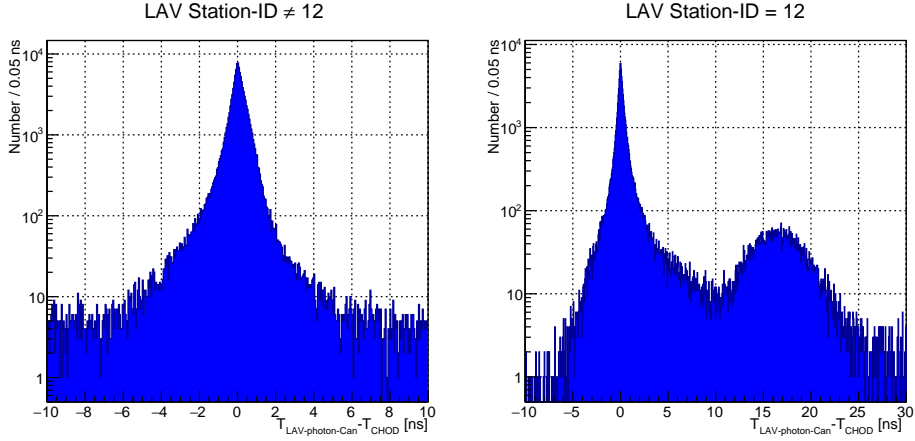


Figure 5.3: Distribution of the time difference between the LAV photon candidates and the associated CHOD tracks in all “training”  $K_{\pi 2}$  events. The right diagram shows the time difference of LAV photon candidates from the LAV12, while the left diagram is for candidates from left eleven LAV stations.

#### 5.4 False veto effect

Apart from the  $\pi^+$  clusters, false rejection is also contributed by the accidental rejection caused by the photon detector’s noise which was not taken into account in the MC simulation. Hence, we estimated the additional random veto factor,  $C_{False-random}$ , by applying above photon veto cuts on the  $K_{\mu 2}$  sample from Run 3809. As we can see in Table 5.1, there is a tiny difference between the  $C_{False-random}$  for momentum range  $[15, 35]$  GeV/c and that for  $\leq 40$  GeV/c. This factor was evaluated to be nearly 0.983, which could also be used as  $A_{PV}$  in Equation 3.1 since photon veto cuts should have almost same accidental veto effect on  $K^+ \rightarrow \pi^+ \nu \bar{\nu}$  events.

Combined with  $C_{False-\pi^+}$  in section 5.1.1, total false rejection factor  $C_{False}$  is estimated to be 92.77%.

#### 5.4. False veto effect

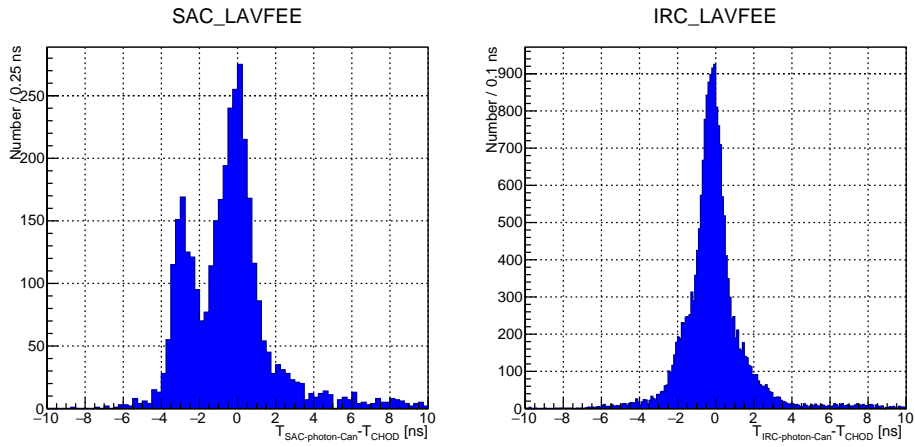


Figure 5.4: Distribution of the time difference between the LAVFEE based SAV photon candidate and the associated CHOD track in  $K_{\pi 2}$  events from run 3801. The left diagram shows the time difference of LAVFEE based SAC photon candidates, while the right diagram is for LAVFEE based IRC photon candidates.

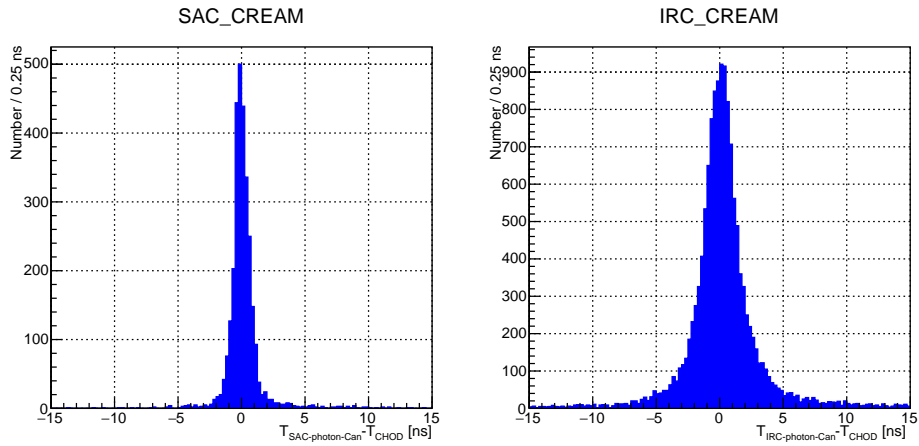


Figure 5.5: Distribution of the time difference between the CREAM based SAV photon candidate and the associated CHOD track in  $K_{\pi 2}$  events from run 3801. The left diagram shows the time difference of CREAM based SAC photon candidates, while the right diagram is for CREAM based IRC photon candidates.

5.4. False veto effect

---

$K_{\mu 2}$	Events number 15 to 35 GeV/c	Events number $\leq 40$ GeV/c
Trial events	406560	565836
Reject LKr standard photons	405785	564737
Reject LAV photons	400148	557111
Reject SAV-LAVFEE photons	400044	556963
Reject SAV-CREAM photons	399745	556541
Reject LKr extra photons	399675	556435
$C_{False-random}$	98.31%	98.34%

Table 5.1: This table shows how many  $K_{\mu 2}$  events from Run 3809 passed each photon cut.

# Chapter 6

## Analysis results

In this chapter, we followed the analysis strategies in Chapter 3 to evaluate the  $K_{\pi 2}$  background and the branching ratio of the decay  $\pi^0 \rightarrow \nu\bar{\nu}$  using other 2015 minimum bias runs and MC data. These runs were reconstructed by the NA62Reconstruction<sup>18</sup> package v0.9.1 (latest revision). To estimate  $A_{kinematics}$  and  $C_{missreco}$ , we generated some  $K_{\pi\nu\bar{\nu}}$  and  $K_{\pi 2}$  events using NA62MC package v0.9.1 and reconstructed them with the same NA62Reconstruction package.

### 6.1 Kinematics

#### 6.1.1 Kinematics rejection for $K_{\pi 2}$

##### MC simulation

300K  $K_{\pi 2}$  MC events were generated for studying kinematics rejection efficiency. After applying selection cuts in section 4.4.1, except the  $\pi^0$  cut, on MC events, we got 19288 trial events whose  $M_{missing-\pi}^2$  distribution is shown in Figure 6.1, where the NA62 accessible  $K^+ \rightarrow \pi^+\nu\bar{\nu}$  phase space regions I and II are roughly indicated by green lines. Almost all events reside in a narrow core with resolution of  $1.14 \times 10^{-3} \text{ GeV}^2/c^4$ . There are 21 events leaking into two signal regions: 11 events entered in region I,  $[0, 0.01] \text{ GeV}^2/c^4$ , and 10 events were found in region II,  $[0.026, 0.068] \text{ GeV}^2/c^4$ . In summary, MC results suggest that the inefficiency of kinematics rejection for  $K_{\pi 2}$  events is  $(1.09 \pm 0.24) \times 10^{-3}$ .

##### Data

We also analyzed nearly 2500 bursts from Run 3821 and identified 49077  $K_{\pi 2}$  events using all selection cuts in section 4.4.1. Figure 6.2 shows the  $M_{missing-\pi}^2$  spectrum for these events. It can be seen that the spectrum of  $K_{\pi 2}$  events from data has slightly wider distribution than MC simulation

---

<sup>18</sup>NA62 Software contains NA62MC, NA62Reconstruction, NA62Analysis and NA62DB packages, see <https://na62-sw.web.cern.ch/software> for details

## 6.1. Kinematics

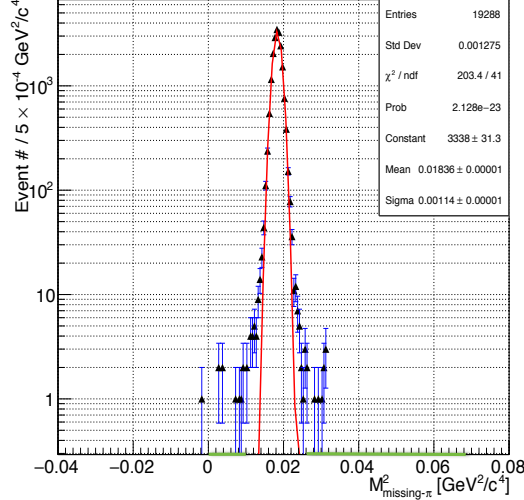


Figure 6.1: The  $M^2_{missing-\pi}$  distribution for  $K_{\pi 2}$  MC events.  $M^2_{missing-\pi}$  was calculated using momentum of a GTK kaon track and a spectrometer track.  $K^+ \rightarrow \pi^+ \nu \bar{\nu}$  signal regions were indicated by green lines.

and is a little bit noisy. This might be caused by accidentals since part of the GTK system suffered from high noise during the run. Of the 49077 trial events, 52 events entered in region I and 54 events were found in region II, which results in  $S_{kinematics} \approx (2.16 \pm 0.21) \times 10^{-3}$ .

### 6.1.2 Kinematics acceptance for $K_{\pi \nu \bar{\nu}}$

In addition to 300K  $K_{\pi 2}$  MC events, we also generated 300K  $K_{\pi \nu \bar{\nu}}$  MC events to estimate the  $A_{kinematics}$  in Equation 3.1. The analysis process is same as MC study in section 6.1.1. Compared with the  $K_{\pi 2}$  MC simulation, there are more  $K_{\pi \nu \bar{\nu}}$  events surviving one track selection cuts and  $K_{\pi 2}$  selection cuts, which means those cuts have different efficiency for  $K_{\pi 2}$  and  $K_{\pi \nu \bar{\nu}}$  decays. Based on the simulation  $\frac{A_{K_{\pi \nu \bar{\nu}}}}{A_{K_{\pi 2}}} = \frac{26269}{19288} \approx 1.362$ . The  $M^2_{missing-\pi}$  distribution of selected  $K_{\pi \nu \bar{\nu}}$  events is shown in Figure 6.3. Out of 26269  $K_{\pi \nu \bar{\nu}}$  events, 15077 events enter into two signal region, which gives  $A_{kinematics} = 57.39\%$ .

## 6.1. Kinematics

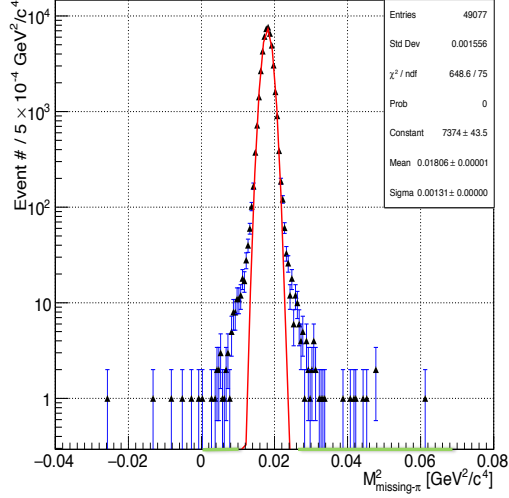


Figure 6.2: The  $M^2_{missing-\pi}$  distribution for  $K_{\pi 2}$  events in Run 3821.  $M^2_{missing-\pi}$  was calculated using momentum of a GTK kaon track and a spectrometer track.  $K^+ \rightarrow \pi^+ \nu \bar{\nu}$  signal regions were indicated by green lines.

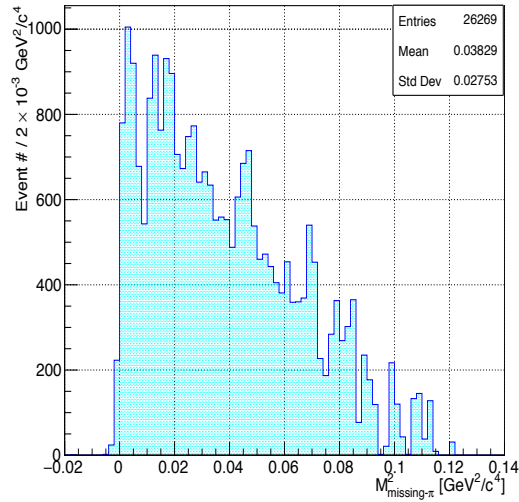


Figure 6.3: The  $M^2_{missing-\pi}$  distribution for  $K_{\pi \nu \bar{\nu}}$  MC events.  $M^2_{missing-\pi}$  was calculated using momentum of a GTK kaon track and a spectrometer track.

## 6.2. $\pi^0$ rejection using photon veto cuts

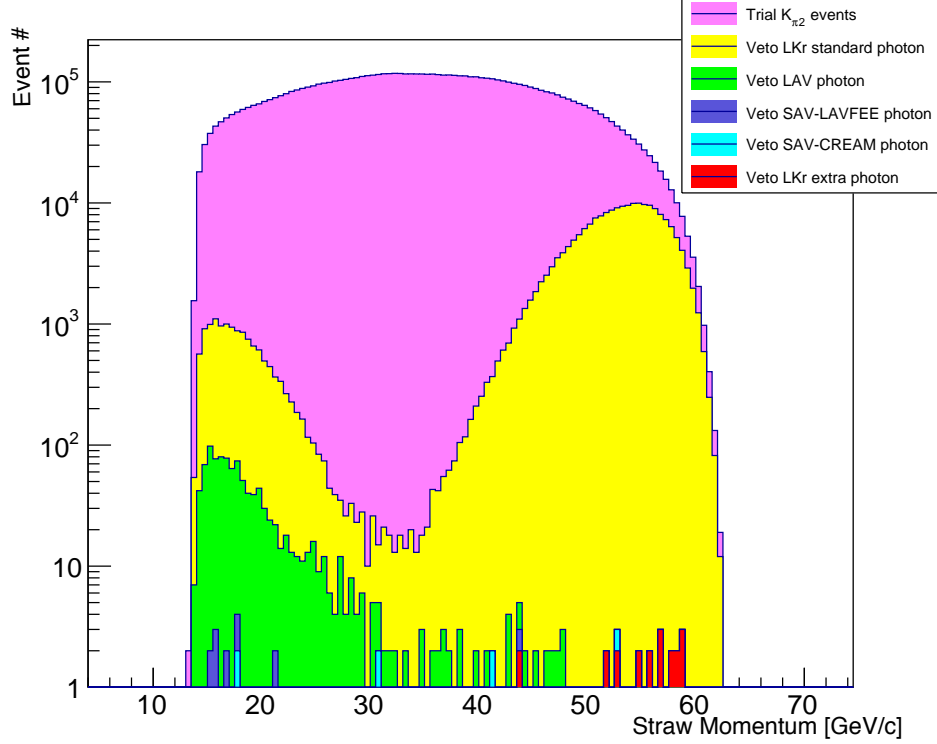


Figure 6.4: This figure shows how  $K_{\pi^2}$  events from six 2015 minimum bias runs survived each photon veto cut.

## 6.2 $\pi^0$ rejection using photon veto cuts

Using the cuts described in section 4.4.2, we got 7.1M  $K_{\pi^2}$  events from six minimum bias runs (3809, 3810, 3811, 3813, 3818, 3821) before placing the momentum cut. Then we checked the  $\pi^0$  veto efficiency by applying photon veto cuts one by one on the selected  $K_{\pi^2}$  sample. As shown in Figure 6.4, most remaining  $K_{\pi^2}$  events (red bars) have high  $\pi^+$  momentum. This is not surprising since photon detectors have small efficiency of detecting low energy photons. We got no events left in the desired momentum ranges after placing all photon veto cuts.

Only  $K_{\pi^2}$  events with  $\pi^+$  momentum in [15, 35] GeV/c were used for this study. As shown in Table 6.1, we got zero events left out of 3553586 trial

### 6.3. $K_{\pi 2}$ background

$K_{\pi 2}$	15 to 35 GeV/c	$\leq 40$ GeV/c
Trial events	3553586	4735650
Final events	0	0

Table 6.1: Number of  $K_{\pi 2}$  events in two momentum ranges passing the photon veto cuts.

events. When zero events were observed, the number of remaining events was limited to be  $< 2.3$  at 90% C.L. using Poisson statistics, which results in:

$$\begin{aligned}
 S_{PV} &= \frac{N_{left}}{N_{\pi^0} \cdot C_{False}} \\
 &< \frac{2.3}{3553586 \times 0.9277} = 7.0 \times 10^{-7} \text{ (90\% C.L.)}
 \end{aligned}$$

### 6.3 $K_{\pi 2}$ background

Plugging all the factors into Equation 3.1, the S/B ratio for the  $K_{\pi 2}$  background should be:

$$S/B > \frac{8 \times 10^{-11} \times 0.574 \times 0.983 \times 1.362}{0.207 \times 2.16 \times 10^{-3} \times 7.0 \times 10^{-7}} = 0.2$$

### 6.4 Branching ratio of the decay $\pi^0 \rightarrow \nu\bar{\nu}$

We generated another 300K  $K_{\pi 2}$  MC events where  $\pi^0$  was forced to decay into  $\nu\bar{\nu}$  to compute  $\frac{A_{K_{\pi 2}(\pi^0 \rightarrow \nu\bar{\nu})}}{A_{K_{\pi 2}}}$ . Smaller  $A_{K_{\pi 2}}$  was expected due to misreconstruction of the  $\pi^+$  track, which may happen when photons or electrons from  $\pi^0$  decays overlap with the  $\pi^+$  track but doesn't occur if  $\pi^0$  decays into neutrino pairs. We got 23479 events surviving the selection cuts in section 4.4.1 (except the  $\pi^0$  cut) from this MC sample, compared to 19288 events from the  $K_{\pi 2}$  MC sample where neutral pions went through common decays. Hence,  $\frac{A_{K_{\pi 2}(\pi^0 \rightarrow \nu\bar{\nu})}}{A_{K_{\pi 2}}} = \frac{23479}{19288} \approx 1.217$ .

As shown in Table 6.1, after photon veto cuts no events were left from 4735650  $K_{\pi 2}$  events where  $\pi^+$  momentum is below 40 GeV/c. Actually, we found one interesting event from Run 3813 (burst number:889, event number: 4112) which survived all  $K_{\pi 2}$  selection cuts in section 4.4.2, except

#### 6.4. Branching ratio of the decay $\pi^0 \rightarrow \nu\bar{\nu}$

---

$\frac{E}{P}$  cut<sup>19</sup>, and all photon veto cuts. However, this event is probably not  $\pi^0 \rightarrow \nu\bar{\nu}$  candidate since it has a few in-time MUV1 candidates with large deposited energy. We added the energy of all in-time MUV1 candidates in that event and found that the ratio of total energy deposited in MUV1 to the momentum of straw track, ( $\frac{E_{MUV1}}{P_{straw}}$ ) is 2.37. This ratio is abnormally large for a  $\pi^0 \rightarrow \nu\bar{\nu}$  event since the maximum  $\frac{E_{MUV1}}{P_{straw}}$  we acquired from 58073  $K_{\pi 2(\pi^0 \rightarrow \nu\bar{\nu})}$  MC events is only 1.24. This event motivated us to set another  $\pi^0 \rightarrow \nu\bar{\nu}$  identification cut,  $\frac{E_{MUV1}}{P_{straw}} < 0.6$ , besides photon veto cuts, for future  $\pi^0 \rightarrow \nu\bar{\nu}$  study. The efficiency of this cut for observing  $\pi^0 \rightarrow \nu\bar{\nu}$  decay in tagged  $K_{\pi 2}$  event was estimated to be 99.63% using  $K_{\pi 2(\nu\bar{\nu})}$  MC events.

In summary, based on zero remaining events the 90% C.L. upper limit of the branching ratio of the decay  $\pi^0 \rightarrow \nu\bar{\nu}$  was obtained as:

$$Br(\pi^0 \rightarrow \nu\bar{\nu}) < \frac{2.3}{4735650 \times 0.9277 \times 1.217} = 4.3 \times 10^{-7}$$

---

<sup>19</sup>The  $\frac{E}{P}$  of this event is 0.8993, failing the  $0.1 < \frac{E}{P} < 0.85$  cut. But the mass of matched sing-ring RICH candidate is 0.138747 GeV/c<sup>2</sup>, close to the  $\pi^+$  mass. It should be noted that this event does not have matched multi-ring RICH candidate and the straw momentum of  $\pi^+$  is 15.03 GeV/c.

## Chapter 7

# Conclusions

This study provided the preliminary result of the S/B for the  $K_{\pi 2}$  background in the measurement of  $K^+ \rightarrow \pi^+ \nu \bar{\nu}$  in NA62. The S/B was estimated to be greater than 0.2 based on the efficiency results of the kinematics suppression and  $\pi^0$  veto vetoing and some efficiency factors acquired from MC simulations. The required S/B should be at least 10 for the success of the NA62. Our result was limited by insufficient  $K_{\pi 2}$  events, which made it difficult to determine the real inefficiency of  $\pi^0$  rejection in NA62.

Several 2015 minimum bias runs were analyzed to provide the  $K_{\pi 2}$  and  $K_{\mu 2}$  samples for studying the kinematics and  $\pi^0$  vetoing factors. To set cuts for identifying  $K_{\pi 2}$  and  $K_{\mu 2}$  events, the RICH performance for distinguishing  $\pi^+/\mu^+$  in 2015 run was evaluated; a RICH mass cut,  $0.1325 \leq Mass_{RICH-single} \leq 0.2$  GeV/c<sup>2</sup>, would kill 98.53% muons with the efficiency of getting pions at 85.31%. The efficiency of other identification cuts such as kinematics and calorimeters was also evaluated. The kinematic rejection of  $K_{\pi 2}$  events using GTK kaon tracks was found to be  $(2.16 \pm 0.21) \times 10^{-3}$  based on 101 survived events out of 49077 trial  $K_{\pi 2}$  events. This inefficiency was at the same level with what MC simulation found,  $(1.09 \pm 0.24) \times 10^{-3}$ . Nominal kaon tracks were assumed for  $\pi^0$  veto study to acquire more trial  $K_{\pi 2}$  events. Based on zero remaining events out of nearly 3.55M  $K_{\pi 2}$  events, the  $\pi^0$  veto inefficiency of  $< 6.98 \times 10^{-7}$  (90% C.L.) was obtained.

Besides, a slightly larger number of identified  $K_{\pi 2}$  decays obtained with wider momentum range were used to search for the helicity-suppressed decay  $\pi^0 \rightarrow \nu \bar{\nu}$ . We got zero  $\pi^0 \rightarrow \nu \bar{\nu}$  candidates out of approximately 4.74M trial events, which leads to an upper limit of the branching ratio at  $4.3 \times 10^{-7}$  (90% C.L.) Although at present this result is 1.6 times larger than what E949 reported, the limit of  $\pi^0$  detection in NA62 has not been reached yet.

We need more  $K_{\pi 2}$  decays from future runs in NA62 to explore the limit of  $\pi^0$  detection and get the precise results for the S/B of the  $K_{\pi 2}$  background in NA62 and the branching ratio of the decay  $\pi^0 \rightarrow \nu \bar{\nu}$ . In future study, if possible the GTK kaon tracks rather than the nominal kaon tracks should be used to reconstruct kinematics variable for studying the  $\pi^0$  rejection. Once we get remaining events in future, an estimation of background events in

$K_{\pi 2}$  trial events should be achieved. Also, it should be noted although zero  $K_{\pi 2}$  events survived our present photon veto cuts, these cuts may not be the most efficient for rejecting  $\pi^0$ . We should optimize these cuts one by one to get maximum real  $\pi^0$  rejection ( $N_{real} = N_{rejected-\pi^0} \times C_{False}$ ) in the “training” sample. This method was adapted in the E949 [22]. In future multivariate techniques will also be used to improve the optimization of the photon veto cuts for greatest efficiency and rejection.

# Bibliography

- [1] NA62 collaboration et al. NA62 technical design. *CERN European Organization for Nuclear Research*, 2010.
- [2] G. Ruggiero. The NA62 Experiment: Prospects for the  $K^+ \rightarrow \pi^+ \nu \bar{\nu}$  measurement. *PoS*, page 032, 2013.
- [3] D. Bryman, W. J. Marciano, R. Tschirhart, and T. Yamanaka. Rare kaon and pion decays: Incisive probes for new physics beyond the standard model. *Annual Review of Nuclear and Particle Science*, 61:331–354, 2011.
- [4] G. Isidori, F. Mescia, P. Paradisi, C. Smith, and S. Trine. Exploring the flavour structure of the mssm with rare k decays. *Journal of High Energy Physics*, 2006(08):064, 2006.
- [5] M. Blanke, A. J. Buras, B. Duling, S. Recksiegel, C. Tarantino, et al. Arcadia. *Acta Physica Polonica B*, 2010.
- [6] B. Angelucci. Trigger for rare kaon decays searches at the CERN NA62 experiment. 2015.
- [7] A. J. Buras, M. Gorbahn, U. Haisch, and U. Nierste. Charm quark contribution to  $K^+ \rightarrow \pi^+ \nu \bar{\nu}$  at next-to-next-to-leading order. *Journal of High Energy Physics*, 2006(11):002, 2006.
- [8] D. Bryman, A. J. Buras, G. Isidori, and L. Littenberg.  $K_L \rightarrow \pi^0 \nu \bar{\nu}$  as a probe of new physics. *International Journal of Modern Physics A*, 21(03):487–504, 2006.
- [9] J. Brod, M. Gorbahn, and E. Stamou. Two-loop electroweak corrections for the  $K^+ \rightarrow \pi^+ \nu \bar{\nu}$  decays. *Physical Review D*, 83(3):034030, 2011.
- [10] A. Artamonov, B. Bassalleck, B. Bhuyan, E. W. Blackmore, D. A. Bryman, S. Chen, I. Chiang, I.-A. Christidi, P. Cooper, M. Diwan, et al. New measurement of the  $K^+ \rightarrow \pi^+ \nu \bar{\nu}$  branching ratio. *Physical review letters*, 101(19):191802, 2008.

- [11] K. A. Olive, P. D. Group, et al. Review of particle physics. *Chinese Physics C*, 38(9):090001, 2014.
- [12] M. Lenti. The detector for the kaon rare decays experiment NA62 at CERN. *Nuclear Physics B-Proceedings Supplements*, 215(1):287–290, 2011.
- [13] S. Agostinelli, J. Allison, K. a. Amako, J. Apostolakis, H. Araujo, P. Arce, M. Asai, D. Axen, S. Banerjee, G. Barrand, et al. Geant4—a simulation toolkit. *Nuclear instruments and methods in physics research section A: Accelerators, Spectrometers, Detectors and Associated Equipment*, 506(3):250–303, 2003.
- [14] M. Pepe. Rare and forbidden kaon decays at NA62. In *EPJ Web of Conferences*, volume 95, page 03029. EDP Sciences, 2015.
- [15] W. Kalderon. The  $K^+ \rightarrow \pi^+\pi^0\gamma$  (ib) background to the  $K^+ \rightarrow \pi^+\nu\nu$  decay. 2012.
- [16] Y. Fukuda, T. Hayakawa, E. Ichihara, K. Inoue, K. Ishihara, H. Ishino, Y. Itow, T. Kajita, J. Kameda, S. Kasuga, et al. Evidence for oscillation of atmospheric neutrinos. *Physical Review Letters*, 81(8):1562, 1998.
- [17] Q. Ahmad, R. Allen, T. Andersen, J. Anglin, J. Barton, E. Beier, M. Bercovitch, J. Bigu, S. Biller, R. Black, et al. Direct evidence for neutrino flavor transformation from neutral-current interactions in the sudbury neutrino observatory. *Physical Review Letters*, 89(1):011301, 2002.
- [18] A. C. Kalloniatis, J. D. Carroll, and B.-Y. Park. Neutral pion decay into  $\nu\bar{\nu}$  in dense skyrmion matter. *Physical Review D*, 71(11):114001, 2005.
- [19] T. Kalogeropoulos, J. Schechter, and J. Valle. A test for neutrino masses. *Physics Letters B*, 86(1):72–74, 1979.
- [20] P. Herczeg and C. M. Hoffman. On the decays  $\pi^0 \rightarrow \nu\bar{\nu}$ . *Physics Letters B*, 100(4):347–350, 1981.
- [21] L. Arnellos, W. J. Marciano, and Z. Parsa. The decay  $\pi^0 \rightarrow \nu\bar{\nu}\gamma$ . *Nuclear Physics B*, 196(3):365–377, 1982.
- [22] A. Artamonov, B. Bassalleck, B. Bhuyan, E. Blackmore, D. Bryman, S. Chen, I. Chiang, I.-A. Christidi, P. Cooper, M. Diwan, et al. Upper

## Bibliography

---

- limit on the branching ratio for the decay  $\pi^0 \rightarrow \nu\bar{\nu}$ . *Physical Review D*, 72(9):091102, 2005.
- [23] Planck Collaboration et al. Planck 2015 results. xiii. cosmological parameters. *arXiv preprint arXiv:1502.01589*, 2015.
- [24] P. Wang. *Neutrino mass implications for physics beyond the Standard Model*. PhD thesis, Citeseer, 2007.
- [25] V. Kozhuharov. NA62 experiment at CERN SPS. In *EPJ Web of Conferences*, volume 80, page 00003. EDP Sciences, 2014.
- [26] G. Brianti and N. T. Doble. The sps north area high intensity facility. Technical report, CM-P00040064, 1977.
- [27] NA62 collaboration et al. 2016 NA62 status report to the CERN SPSC. Technical report, CERN-SPSC, 2016.
- [28] A. Kluge, G. A. Rinella, S. Bonacini, P. Jarron, J. Kaplon, M. Morel, M. Noy, L. Perktold, and K. Poltorak. The TDCpix readout ASIC: A 75ps resolution timing front-end for the NA62 Gigatracker hybrid pixel detector. *Nuclear Instruments and Methods in Physics Research Section A: Accelerators, Spectrometers, Detectors and Associated Equipment*, 732:511–514, 2013.
- [29] A. Sergi. NA62 spectrometer: a low mass straw tracker. *Physics Procedia*, 37:530–534, 2012.
- [30] P. Lichard. The NA62 straw detector read-out system. *Journal of Instrumentation*, 5(12):C12053, 2010.
- [31] E. Goudzovski, M. Krivda, C. Lazzeroni, K. Massri, F. O. Newson, S. Pyatt, A. Romano, X. Serghi, A. Sergi, R. J. Staley, et al. Development of the kaon tagging system for the NA62 experiment at CERN. *Nuclear Instruments and Methods in Physics Research Section A: Accelerators, Spectrometers, Detectors and Associated Equipment*, 801: 86–94, 2015.
- [32] B. Angelucci, G. Anzivino, C. Avanzini, C. Biino, A. Bizzeti, F. Bucci, A. Cassese, P. Cenci, R. Ciaranfi, G. Collazuol, et al. Pion–muon separation with a RICH prototype for the NA62 experiment. *Nuclear Instruments and Methods in Physics Research Section A: Accelerators, Spectrometers, Detectors and Associated Equipment*, 621(1):205–211, 2010.

- [33] V. Fanti, A. Lai, D. Marras, L. Musa, A. Nappi, R. Batley, A. Bevan, R. Dosanjh, R. Galik, T. Gershon, et al. The beam and detector for the NA48 neutral kaon CP violation experiment at CERN. *Nuclear Instruments and Methods in Physics Research Section A: Accelerators, Spectrometers, Detectors and Associated Equipment*, 574(3):433–471, 2007.
- [34] A. Antonelli, G. Corradi, M. Moulson, C. Paglia, M. Raggi, T. Spadaro, D. Tagnani, F. Ambrosino, D. Di Filippo, P. Massarotti, et al. The NA62 LAV front-end electronics. *Journal of Instrumentation*, 7(01):C01097, 2012.
- [35] F. Ambrosino, G. Corradi, D. Di Filippo, P. Massarotti, C. Paglia, V. Palladino, M. Napolitano, G. Saracino, L. Roscilli, and D. Tagnani. The charged anticounter for the NA62 experiment at CERN. *Physics Procedia*, 37:675–682, 2012.
- [36] K. Ahmet, M. Akrawy, and G. Alexander. The OPAL detector at LEP. 1991.
- [37] F. Ambrosino, A. Antonelli, E. Capitolo, P. Cooper, R. Fantechi, L. Iannotti, G. Lamanna, E. Leonardi, M. Moulson, M. Napolitano, et al. A prototype large-angle photon veto detector for the P326 experiment at CERN. In *Nuclear Science Symposium Conference Record, 2007. NSS'07. IEEE*, volume 1, pages 57–64. IEEE, 2007.
- [38] A. Ceccucci. NA62/P-326 status report. Technical report, 2007.
- [39] G. D. Barr, P. Buchholz, R. Carosi, D. Coward, D. Cundy, N. Doble, L. Gatignon, A. Gonidec, B. Hallgren, G. Kessler, et al. The na48 liquid krypton prototype calorimeter. *Nuclear Instruments and Methods in Physics Research Section A: Accelerators, Spectrometers, Detectors and Associated Equipment*, 323(1):393–397, 1992.
- [40] A. Ceccucci, R. Fantechi, P. Farthouat, G. Lamanna, J. Rouet, V. Ryjov, and S. Venditti. The NA62 liquid krypton calorimeter’s new readout system. *Journal of Instrumentation*, 9(01):C01047, 2014.
- [41] K. Nakamura, P. D. Group, et al. Review of particle physics. *Journal of Physics G: Nuclear and Particle Physics*, 37(7A):075021, 2010.
- [42] G. Ruggiero. NA62 Pinunu working group meeting, 01/19/2016.

- [43] E. Gersabeck, G. Lamanna, A. Sergi, and S. Stamm. Trackless ring fitting algorithm for the rich detector. 2011.
- [44] C. Lazzeroni, K. Eppard, P. Dalpiaz, B. Hallgren, A. Norton, K. Kleinknecht, A. Maier, S. Balev, V. Palladino, G. Collazuol, et al. Study of the  $K^\pm \rightarrow \pi^\pm \gamma \gamma$  decay by the NA62 experiment. *Phys. Lett. B*, 732(arXiv: 1402.4334):65–74, 2014.
- [45] G. Ruggiero. NA62 Pinunu Analysis meeting, 01/26/2016.
- [46] T. Spadaro. NA62 Pinunu Analysis meeting, 01/26/2016.
- [47] L. Peruzzo. NA62 Physics Analysis Meeting, 06/01/2016.
- [48] W. S. Wong, G. Anton, R. Ballabriga, M. Böhnel, M. Campbell, E. Heijne, X. Llopart, T. Michel, I. Münster, R. Plackett, et al. A pixel detector asic for dosimetry using time-over-threshold energy measurements. *Radiation Measurements*, 46(12):1619–1623, 2011.
- [49] M. Barone. *Astroparticle, Particle and Space Physics, Detectors and Medical Physics Applications: Proceedings of the 9th Conference: Villa Olmo, Como, Italy, 17-21 October 2005*. World Scientific, 2006.

# Appendix A

## Gain measurement of the STRAW spectrometer

In order to value and optimize NA62 straw trackers' performance, we measured the dependence of the gas gain versus applied voltage at 970 *mbar* absolute pressure for three different gas mixtures, *Ar* – *CO*<sub>2</sub> (70-30 & 85-15 & 93-7). Battery and a new method of gas gain measurement were used to get more accurate current. Our results indicate the gain for *Ar* – *CO*<sub>2</sub> (70-30) gas mixture at 1752 V is  $(5.479 \pm 0.213) \times 10^4$ .

### Setup

The straw prototype at CERN was used to conduct the experiment. 16 tubes were connected with flex-rigid circuits board to one Front-End board. We used one board with high voltage and gas input connected shown by Figure A.1. An auto-ranging Keithley-6487 picoammeter with sensitivity 0.01 pA has been connected between the straw cathode and the ground to measure the produced currents. Although the sensitivity of picoammeter is quite high, its reading is constantly fluctuating,  $\pm 0.2$  nA, once connected to the high voltage supply. This may be caused by the noisy grounding. To solve this problem, we use a 130V battery as power supply, which avoids parasitic ground loops and then allows us to measure very small current, for detecting primary current. Besides, we took a new method proposed in which radiation source rates can be changed without affecting measurement so that we can use high activity source, an 2.7GBq <sup>55</sup>*Fe* source, to get the larger primary current. Due to space charge effect and safety issue, 0.32 mA current was set as upper limit.

### Get I v.s. Voltage curves

After putting <sup>55</sup>*Fe* source in the nearest distance, we used voltage division for the battery to get different voltage from 45 to 130V and measured the

Get  $I$  v.s. Voltage curves



Figure A.1: Straw prototype with Gas and HV Input Connected

current in some points. As shown by Figure A.2 a, we get a plateau (gain  $\approx 1$ ) for the current within this range, which demonstrates  $I_{primary}$  equals  $431.8 \pm 4.05$ . Without moving the source, we replaced battery with high voltage supply, changed the voltage and got Curve 1. Then the distance and angle of  $^{55}Fe$  source was adjusted to decrease source rate, Curve 2 was acquired after this. So was Curve 3. Finally, we got the current v.s. voltage line shown in Figure A.2 a.

Using the equation  $gain = \frac{I_{measured}}{I_{primary}}$ , gain for Curve 1 is easy to get. Then we can calculate the average constant  $k_1 = \frac{gain}{I_{measured}}$  for Curve 2 using the known gain of several points deduced from Curve 1. Gain for other points in Curve 2 can be obtained using known  $k_1$ . Repeating this, we can get gain v.s. voltage in Figure A.2 b.

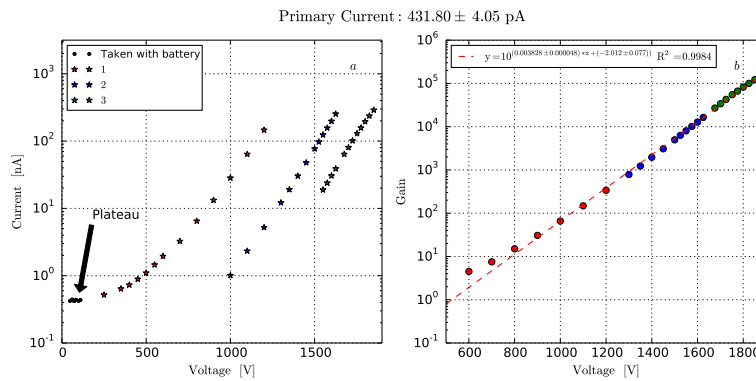


Figure A.2: Gain v.s. Voltage for  $Ar - CO_2(70-30)$  at 970 mbar

## Gas gain result

We followed the above process and got gain v.s. voltage curves for  $Ar - CO_2$ (70-30, 85-15, 93-7) corresponding with Figure A.2, Figure A.3 and Figure A.4, respectively. Pressure was set at 970 *mbar*.

Due to the fact that current reading fluctuates with high voltage power supply as mentioned above, we drop the points whose current below 2 nA. Besides, Figure A.3 shows when gain is above  $2 \times 10^5$  straw tracker enters into non-proportional counting region, a transition region to the Geiger region. Hence, to get credible linear fit result we use the data whose gain is within the region  $[10, 2 \times 10^5]$ . Curves were linear fitted using bivariate correlated errors and intrinsic scatter (BCES) model. The error in y coordinate equals 1% in current reading plus initial error in primary current.

We can use fit parameters to estimate the gain at exact voltage like 1750, but it brings large uncertainty  $\frac{\delta(10^a)}{10^a} = \ln(10) * \delta a$ . Consequently, we decide to directly use the data point. For  $Ar - CO_2$  (70-30) gas, at 1752 V, the gain should be  $(5.479 \pm 0.213) \times 10^4$  assuming total error equals maximum 2% in reading plus 0.945% error in constant  $K$  (0.655% in  $K_1$  and 0.29% in  $K_2$ ) plus error in primary current, 0.938%.

It is obvious that with the proportion of  $Ar$  increased the gain dramatically increases. The corresponding voltage for gain achieving  $10^4$  is 1575V, 1400V and 1275V for 70-30, 85-15 and 93-18. If we want to achieve  $10^5$  in gain for the best resolution, the working voltage should be set at 1825V for the present working gas mixture, i.e., 70%  $Ar$  and 30%  $CO_2$ , at 970 *mbar*. Using gas mixtures with denser  $Ar$  can decrease the working voltage. 1610V or 1460V is required if we used  $Ar - CO_2$ (85-15) or  $Ar - CO_2$ (93-7) as filled gas.

## Gas gain result

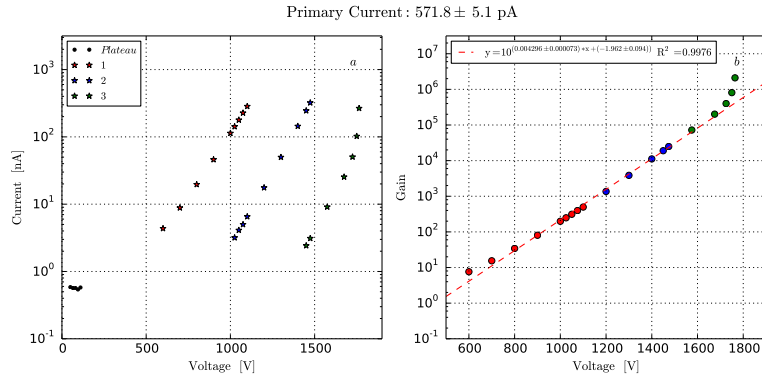


Figure A.3: Gain v.s. Voltage for  $Ar - CO_2(85-15)$  at 970 mbar

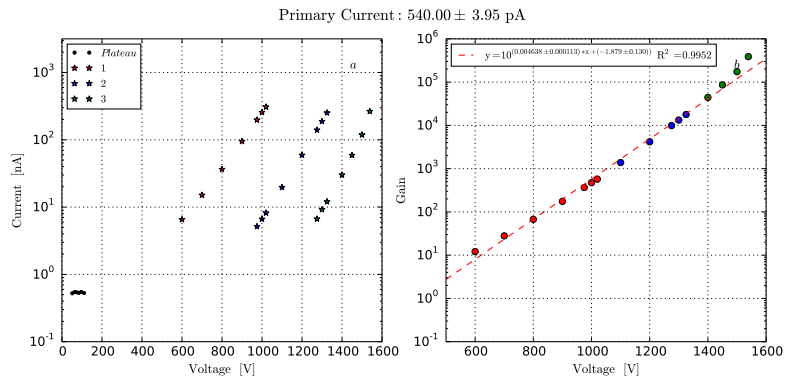


Figure A.4: Gain v.s. Voltage for  $Ar - CO_2(93-7)$  at 970 mbar

## Appendix B

# Study of the false $K_{\pi 2}$ rejection caused by additional $\pi^+$ LKr clusters

We generated 300K  $K_{\pi 2}$  MC events where  $\pi^0$  was forced to decay into  $\nu\bar{\nu}$ . In this MC simulation, LKr clusters were only generated by  $\pi^+$  track so that we can use these events to study the false rejection effect caused by additional  $\pi^+$  LKr clusters.

First, we applied the one track selection cuts and  $K_{\pi 2}$  selection cuts (section 4.4.2) on MC event. In each survived MC event, we selected only one LKr cluster which is furthest from the  $\pi^+$  projected position in the LKr from all LKr clusters except the one associated with the  $\pi^+$  track. It should be noted that the distance was set to 0 if no additional LKr cluster was found. The distance distribution of these selected clusters is shown in Figure B.1. Nearly 75%  $K_{\pi 2}(\pi^0 \rightarrow \nu\bar{\nu})$  events in this study only have one LKr cluster, which is associated with the  $\pi^+$  track.

As long as the distance of the selected LKr cluster in a MC event was larger than the radius of the masked region we set, we treated that LKr cluster as a fake photon cluster and reject the event. The reject efficiency distribution for different radii is shown in Figure B.2. The efficiency is around 94.36% if we set the radius of the masked region to 150 mm.

Appendix B. Study of the false  $K_{\pi 2}$  rejection caused by additional  $\pi^+$  LKr clusters

---

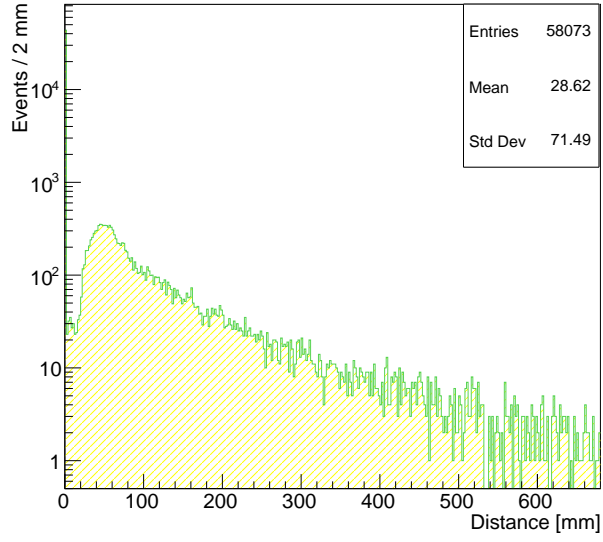


Figure B.1: This figure shows the distance of the selected LKr cluster to the projected position of  $\pi^+$  in the LKr.

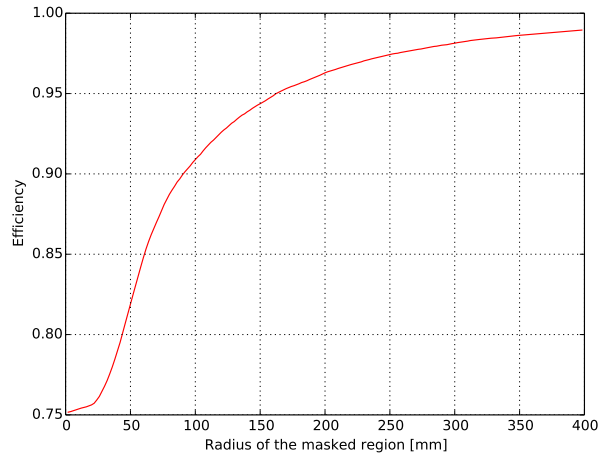


Figure B.2: This figure shows the rejection efficiency for different radii of the masked region.